The Veto System of the LZ Dark Matter Experiment

by

Luke Korley

A dissertation submitted in partial fulfillment
of the requirements for the degree of
Doctor of Philosophy
(Physics)
in The University of Michigan
2023

Doctoral Committee:

Assistant Professor Bjoern Penning, Chair
Professor Dragan Huterer
Professor Igor Jovanovic
Professor Wolfgang Lorenzon
Associate Professor Joshua Spitz
Assistant Professor Jui-Jen Wang

Luke Korley

lkorley@umich.edu

ORCID: 0000-0002-1168-9195

DEDICATION

This thesis is dedicated to my mother and father who have always been supported me in my studies. They have been a source of encouragement from the very beginning, believing in me and cheering me on through the most difficult times. It is hard to put into words how thankful I am for your support, and how glad I am that you were there to show me there was light at the end of tunnel in those moments when I could not see it for myself.

ACKNOWLEDGEMENTS

There are a multitude of people without whom I would not have been able to conduct the research presented in this dissertation. Whilst this acknowledgement is too brief to name them all, I wish to express my sincerest gratitude to them.

Firstly I wish to thank my advisor Professor Bjoern Penning, who took a chance on me when we first met at Bristol back in 2017, and has provided guidance and support since. The path has not been the easiest and I appreciate you being in my corner through it all with patience, understanding, and perspective, even in my less teachable moments.

To Professor Jui-Jen Wang, I extend my gratitude for your heroic efforts providing camaraderie and advice when we first started at Brandeis. It was a pleasure to work with you and your experience both in the lab and outside, distilled through our many outdoor work breaks, has been invaluable to me. I will not forget how you made time to discuss ideas and provided a space for me to clarify my thinking, even when you were incredibly busy.

To my colleagues and friends at Brandeis, it was a joy to work and socialise with you. Thank you Jim, Kevan, Richard, and Andrey for providing your engineering expertise and not hesitating to pose the challenging questions which helped sharpen my sometimes woolly ideas.

To Zach, Sagnik, Ian, Alex, Andrew, Alyssa, Seth and the many others who were regulars at our friday socials, I am grateful for the comfortable and welcoming atmosphere you provided which made me feel a little less alone so far from home. I enjoyed your company and insight discussing topics as varied as air travel in the 70s and anime. In particular, I wish to thank Ian for being such a pleasant housemate and welcoming me into a varied group of friends with whom I enjoyed rigorous debate and exciting social activity.

During my various trips on-site it was a pleasure to encounter our wonderful LZ collaborators who made the long days in the SAL and underground that much easier to handle. Who would've thought one could indulge in the classic English past-time of moaning and whinging with other brits in Lead, South Dakota! Thank you Umit, David, and Sally who took me under her wing for the first LZ analysis I took part in. I cannot look back on my time on-site without thanking the illustrious Derek Lucero,

who beyond his valued skills as an engineer, warmly welcomed me into his home for merry-making and poker. I will not forget your kindness.

To my friends and colleagues at Michigan, thank you for making the transition that much easier to bear. Micheal, Harvey, and Johnny, the debaucherous fun interlude of the Ypsilanti den provided a unique and welcomed separation from campus life for which I am thankful. I will remember the many conversations on life, the universe and everything had with Chami, Sam, Maris, Alyssa, Harvey, Micheal, Nora, Geertje, and Chris for years to come. It has been a joy to share a workspace, move across the country, and adventure unscrupulously in fictitious lands with you all. It will be a pleasure to see you all progress in your careers, whichever you choose.

I would also like to thank Dr Daniel Murphy and Donald Griffis who have provided me with much needed perspective during my time at Michigan.

To Ozi and Gaston, thank you for being there for me when I could not do so for myself. Your compassion and care has not gone unnoticed during the difficult writing and completion period. You have my utmost gratitude and appreciation. I hope I can provide even a fraction of the support you have given me when you reach this point.

To my friends and family back home, you have been and remain a source of immeasurable support. Thank you all for believing in me, providing an escape in difficult times, and keeping me grounded and sane. I look forward to spending more time with you all.

TABLE OF CONTENTS

LIST OF FIGURES

Figure

LIST OF TABLES

Table

LIST OF ABBREVIATIONS

CMB Cosmic Microwave Background

SHM Standard Halo Model

WIMP Weakly Interacting Massive Particle

SI Spin Independent

SD Spin Dependent

LZ LUX-ZEPLIN

TPC Time Projection Chamber

OD Outer Detector

SURF Sanford Underground Research Facility

PMT Photo-multiplier Tube

GdLS Gadolinium Doped Liquid Scintillator

OCV Outer Cryostat Vessel

ICV Inner Cryostat Vessel

CSD Calibration Source Deployment

BACCARAT Basically A Component-Centric Analogue Response to AnyThing

RQ Reduced Quantity

SPE Single Photo-electron

OCS Optical Calibration System

ER Electronic Recoil

NR Nuclear Recoil

ADCC Analog-to-Digital Converter Counts

BR Branching Ratio

phd Photons Detected

ABSTRACT

A large body of astrophysical and cosmological evidence suggests the majority of the mass density of the universe is composed of non-luminous, weakly/non interacting kind of matter, dubbed dark matter. Weakly Interacting Massive Particles (WIMPs) are a leading candidate for the make-up of dark matter, motivated by both theoretical and cosmological arguments. A dual-phase Xenon Time Projection Chamber (TPC) is employed by the LUX-ZEPLIN experiment to detect WIMP-nucleon interactions. This ultra-clean experiment benefits greatly in sensitivity from the inclusion of a gadolinium-doped liquid scintillator (GdLS) Outer Detector (OD) to veto troublesome neutron backgrounds thermal neutron captures on gadolinium nuclei.

To achieve this purpose, an array of PMTs observes scintillation light from the interaction of gamma-rays produced by these captures in the GdLS. This work presents the successful calibration of these PMTs, and a series of tests exploring the anomalous increase in PMT dark rate when exposed to water. An independent OD trigger is defined in order to boost statistics of high energy OD events facilitating future studies intending to probe the ambient neutron flux and muon events. This trigger was found to be maximally efficient for pulses of size equivalent to neutron capture signals.

The dominant source of false vetos in the OD comes from gamma-rays produced by ^{238}U, ^{232}Th, and ^{40}K contaminants in the walls of the Davis cavern in which LZ is housed. The spectrum of these gammas is measured, finding that a layer of shotcrete effectively screens the underlying gamma spectrum. Thus this shotcrete layer is responsible for the measured radioactive contamination levels of 220$\pm$60 Bq/kg of ^{40}K, 29$\pm$15 Bq/kg of ^{238}U, and 13$\pm$3 Bq/kg of ^{232}Th. This measurement informs the background model and understanding of the false veto rate.

Additionally, an attempt is made to identify and measure fast neutrons via proton recoils in the OD by exploiting timing differences between proton and gamma interactions. Although discrimination was not achieved due to smearing effects from reflections, it was found that proton recoil pulses are encapsulated by the veto threshold in LZ and thus removed from the WIMP search dataset of LZ. Finally, the world-leading results of the first WIMP search run of LZ are reported.

CHAPTER I

Introduction

Over the past century, a large body of evidence has built up suggesting the existence of non-luminous, non-baryonic substance, termed dark matter, constituting 25% of the energy density of the universe. Despite the significant evidence supporting its existence and abundance, the structure and make up of dark matter remains a mystery. Whilst the standard model of particle physics has been tremendously effective at describing and predicting the results of a vast array of experiments, it has failed to include dark matter. To date, the primary evidence for dark matter has come from astrophysical and cosmological studies, these have been able to probe the effects of gravity, which remain unexplained by the standard model of particle physics, but are well modelled by if a non-baryonic component (dark matter) which responds to gravity is adopted. Thus determination of the nature of dark matter is of great importance and a significant step into the ever receding frontier of "new physics". In what follows, one provides a brief overview of the evidence for dark matter, the leading candidates for its constituents, and the most prevalent attempts to detect it.

1.1 Evidence for Dark Matter

The origin of the term dark matter is attributed to Fritz Zwicky who used it to describe the significant amount of mass not accounted for by the light output of

the Coma Cluster [1]. Zwicky used the virial theorem, relating potential and kinetic energy of galaxies in the Coma Cluster, to compare the mass implied by kinematics to the luminous mass of the cluster. It was found that the observed velocities of 1 Mm/s were only possible if the cluster contained 400 times the mass estimate of the contained luminous matter. The conclusion of his calculation was that dark matter existed in "much greater density than luminous matter." In subsequent years the

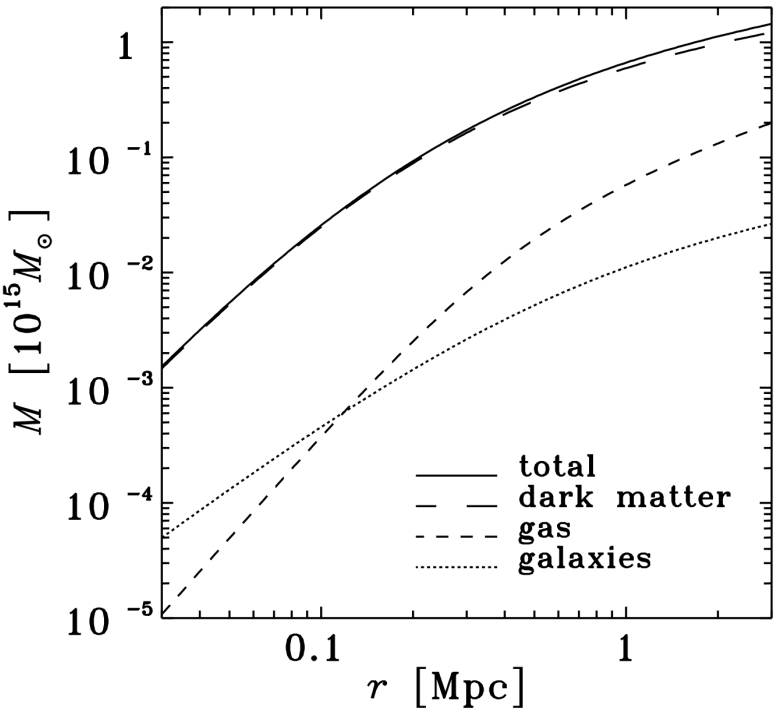

Figure 1.1: Density profile of matter components in the comma cluster as a function of radius relative to virial radius [2].

understanding of the make up of clusters has matured. It is now understood that a great deal of cluster mass is made up of baryonic dust (radiating infrared light) and gas (radiating X-rays). However, more recent studies of galaxy clusters which include these components in the calculation also point to unseen matter contributing the bulk of mass, the dark matter. Whilst Zwicky grossly underestimated the impact of these components[1], the more recent calculations point to a still immense 85% contribution

[1]This author forgives Zwicky for not observing things beyond the reach of the technology available to him and his contemporaries.

from dark matter [2].

1.1.1 Rotation Curves of Galaxies

Further evidence for dark matter came, decades later, from studies of galactic rotation curves in which the velocity of stars stays relatively constant with distance from the galactic centre [3]. This is a departure from the predictions of classical dynamics where the velocity distribution $v(r)$ as a function of distance from the galactic center r is given by:

$$\begin{aligned} v(r) &= \sqrt{\frac{GM(r)}{r}}, \\ M(r) &= 4\pi \int \rho(r) r^2 dr, \end{aligned} \tag{1.1}$$

where $M(r)$ is the mass contained within r, and $\rho(r)$ is the mass density profile. The

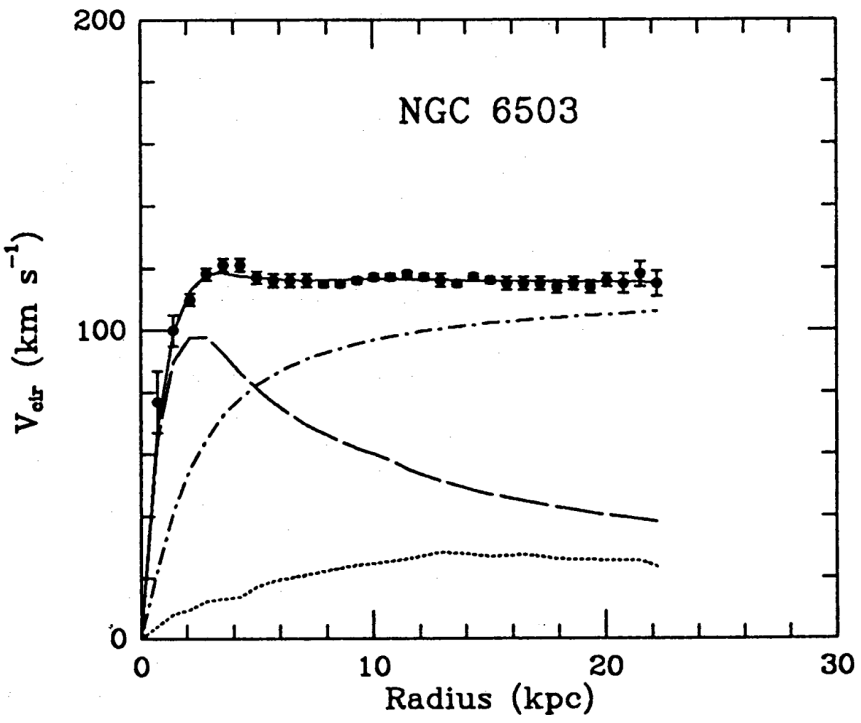

Figure 1.2: Galactic rotation curve for NGC-6503 with the luminous disk, gas and halo contributions fit to the observed data (black dots) producing the combined fit shown by the solid curve [4].

velocity distribution is expected to fall with $\frac{1}{\sqrt{r}}$ far from the luminous mass center of the galaxy since the contained mass is expected to be focused around the luminous mass.

However, the rotation curves are observed to be flat at large radial diastances from the centre as illustrated in Fig. 1.2. This observation is consistent with a large fraction of the galaxy's mass being in a diffuse halo extending beyond the edges of luminous matter. This phenomenon has been observed in many galaxies, resulting in the conclusion that the bulk of the galactic mass is not contained within the luminous disk, but appears to be in an extended halo dominated by dark matter. Ongoing investigations now focus on Low Surface Brightness (LSB) galaxies in which dark matter dominates throughout [5, 6].

1.1.2 Gravitational Lensing and Galaxy Clusters

A key result of general relativity is the curvature of light paths caused by the presence of mass. Photons take paths along null geodesics, that is paths along which the space-time interval is zero. With the presence of mass warping space-time, these paths are also warped/curved. This is known as gravitational lensing and manifests itself as either as strong lensing, weak lensing, or microlensing [7]. Strong lensing typically requires mass above some critical density; producing multiple images in the case of a point source of light, and arcs or more rarely Einstein rings in the case of an extended light source. The first complete Einstein ring discovered is shown in Fig. 1.3. Weak lensing is far more common but multiple images are not produced, rather it manifests as a subtle distortion in the image. As such, this effect is detected statistically. Microlensing is caused by significantly smaller objects (planet - solar mass) distorting the image of bright sources. Since the lensing mass is so small, the displacement of light is not discernible, however the lensing effect does cause a change in apparent brightness of the source. The magnitude of these distortions is directly

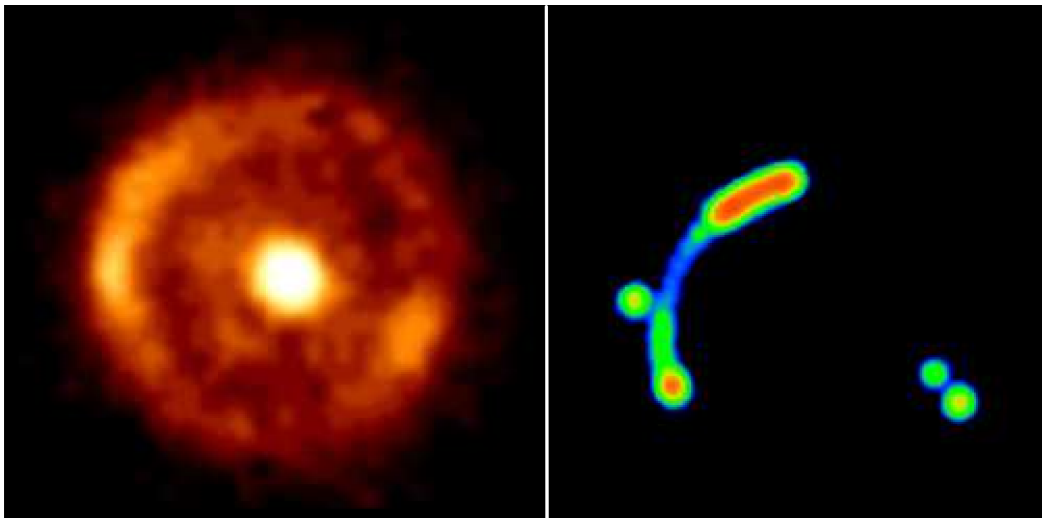

Figure 1.3: **Left:** The Hubble Space Telescope infra-red picture of the distant galaxy B1938+666 which has been imaged into an Einstein ring by an intervening galaxy. The intervening galaxy shows up as the bright spot in the centre of the ring. **Right:** The MERLIN radio picture of the radio source B1938+666 embedded in the distant galaxy. The incomplete ring (or arc) shows that the radio source is not perfectly aligned with the lens galaxy and the Earth. The lens galaxy does not contain a radio source and hence does not show up in this picture. Figure adapted from [8].

correlated with the amount of mass present, thus the amount of mass causing the lensing effect can be measured. Comparing the mass determined by lensing measurements to the luminous mass of galaxy clusters, a discrepancy is observed implying the existence of large quantities of non-luminous mass [9].

Further evidence of unaccounted for mass at the scale of galaxy clusters is demonstrated with the Bullet Cluster (1E0657-558). This cluster is the result of a merger between two smaller clusters, in which baryonic matter is observed via electromagnetic radiation and the total mass is detected via weak lensing. These observations show distinct and separate mass centres from the two approaches, as can be seen in Fig. 1.4. The x-ray luminous (baryonic) matter from the merging clusters interacted strongly causing it to slow down and form a globular centre. However, the bulk of the mass in the clusters appear to have passed through without significant interaction leaving the two lensing centres on the outer edges. It is inferred from this that the large fraction of non-luminous mass must be very weakly interacting, both with itself,

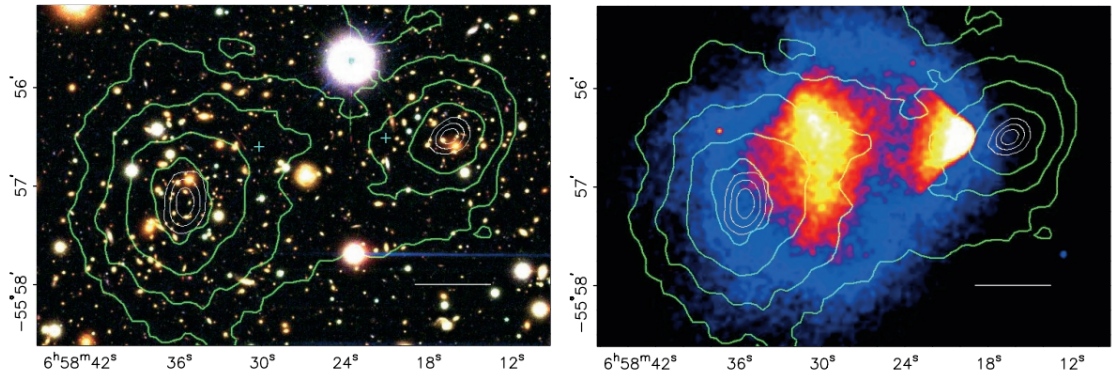

Figure 1.4: The Bullet Cluster (1E0657-558) resulting from merger of two galaxy clusters. **Left:** Optical image from Magellan observatory. **Right:** X-ray image from Chandra observatory. White bars in both images show 200 kpc distance for scale. Green contours show mass distribution derived from weak lensing, whilst white contours denote uncertainty in the position of the lensing peaks. Adapted from [10].

and with baryonic matter.

1.1.3 Cosmic Microwave Background (CMB) Radiation

Cosmic microwave background (CMB) radiation is the oldest detectable black-body spectrum in the universe, first observed in 1965 [11]. This radiation is a relic from the hot early universe. In the period preceding the CMB (300,000 years after the Big Bang), the universe was hot and dense, filled with an opaque hydrogen plasma which scattered the thermal radiation of the early universe. As the universe expanded the plasma and the radiation cooled; eventually the temperature was low enough for protons and electrons to combine and form neutral hydrogen atoms. This is known as the recombination epoch. At this point, approximately 380,000 years after the Big Bang, the temperature of the universe was approximately 3,000 K [12]. The energy of thermal radiation at this temperature is roughly 0.26 eV, to which hydrogen is transparent given its much higher ionization energy of 13.6 eV. Thus, for the first time photons could travel unimpeded through space. This event is referred to as de-coupling. As the universe continued to expand and cool, these photons have been red shifted to the microwave frequencies observed in the CMB. One striking feature of

the CMB is its uniformity and isotropy. Successive measurements have revealed very little variation, though the tiny fluctuations observed are one of the greatest discoveries from observations of the CMB [13]. The most precise measurement of the CMB to date was produced by the Planck satellite [14]. This measurement, demonstrates how minuscule the non-uniformities are, with a maximum difference of 600 μK in the 2.725 K CMB [15]. The competing forces of gravity and radiation pressure in the

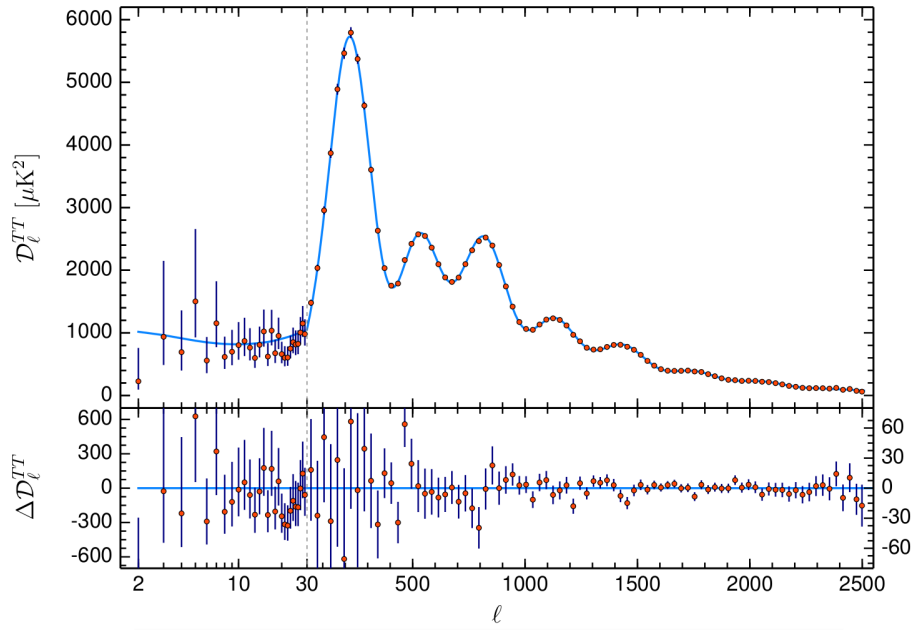

Figure 1.5: Angular power spectrum of CMB temperature fluctuations fit to the ΛCDM model (top), and the small residuals of this fit (bottom) [15].

plasma in combination with the expansion of the universe form pressure waves in the plasma which leave their imprint in the distribution of anisotropy of the CMB, these are baryon acoustic oscillations (BAO). A multipole expansion of the CMB temperature fluctuations yields the angular power spectrum shown in Fig. 1.5. The peaks in this spectrum correlate with various cosmological parameters and allow measurement of said parameters. The location of the first peak points to the flatness of the universe and indicates its total energy density. The second and third peaks indicate the baryon density, with the difference of the baryon density and the total energy density yielding information on the dark matter density [9]. The results of the CMB mea-

surements of Planck are well described by the Lambda Cold Dark Matter (ΛCDM) model of cosmology, pointing to the total energy density of the universe composed of; 69.11% $\pm$ 0.62% dark energy, 4.88% $\pm$ 0.03% baryonic matter, and 26.01% $\pm$ 0.22% dark matter [16].

1.2 Candidates for Dark Matter

Having demonstrated evidence for unobserved mass in the universe from the galactic scale to the cosmological scale, one must consider what could constitute this mass. From observations so far, some properties of this mass can be detailed:

1. Stable on timescales of $\mathcal{O}$(14 billion years) (timescale of the universe)
2. Non-baryonic
3. Very weakly/non interacting via electromagnetism and the strong force
4. Non-relativistic (cold) to allow for clustering
5. Very weak/no self interaction (except gravitational)

A variety of candidate particles have been proposed ranging in mass from 10^{-22} eV to many solar masses. In what follows a small selection of these candidates is briefly discussed.

1.2.1 Neutrinos

The standard model neutrino was one of the first proposed dark matter candidates. Being a long-lived, stable, and weakly interacting particle, neutrinos seem to fit the requirements. Unfortunately though, they have been discounted based on N-body simulations which show that relativistic neutrinos found in the standard model do not allow for the structure formation observed in the universe [17]. However,

sterile neutrinos have been proposed in the stead of existing standard model neutrinos [18]. This new species is postulated to interact with the standard model only via a small mixing angle with the standard model neutrino. Whilst experiments have been consistent with the standard model thus far [19, 20], research into this candidate is ongoing as the neutrino sector is probed more deeply [21].

1.2.2 Axions

Although allowed by the mathematical formulation of quantum chromodynamics (QCD), CP violation has never been observed in strong interactions. This is known as the strong CP problem [22]. Axions are Goldstone bosons produced by spontaneous symmetry breaking of a gauge invariant field at some energy scale, f_a, and were postulated as a solution to this problem [23]. Current experimental constraints place the possible axion dark matter mass between 10^{-6} and 10^{-2} eV [24]. Axion searches seeking to observe axions via their coupling to photons are ongoing. Notable experiments are ADMX [25] and CASPEr [26]. ADMX seeks to observe conversion of axions to microwaves, whilst CASPEr searches for time variation in the nuclear dipole moment and nuclear spin precession induced by axions.

1.2.3 WIMPs

Weakly Interacting Massive Particles (WIMPs) are the final dark matter candidate to be discussed in this work. They are proposed as heavy, non-relativistic particles, with interaction strengths on the scale of the weak force. WIMP candidates arise naturally in a variety of theories and extensions to the standard model such as supersymmetry, the little Higgs model, and universal extra dimensions [27, 28, 29]. These theories were initially proposed to solve issues in the standard model such as the hierarchy problem and to unify the three gauge symmetries of the standard model. Supersymmetry in particular is a compelling and fascinating theory, postulating a

bosonic (fermionic) partner to all standard model fermions (bosons), which produces a range of WIMP candidates [30].

In addition to these theoretical motivations for WIMPs, a cosmological argument exists which reproduces the current dark matter density from WIMPs, known as the 'WIMP miracle'. In the hot environment of the early universe, WIMPs were in thermal equilibrium. At this time the interaction rates for WIMP annihilation producing standard model particles and the reverse are similar, so the relative densities of these should stay constant. As the universe cools, there comes a point beyond which production of WIMPs from interactions with the standard model is suppressed. As such the density of WIMPs falls exponentially with temperature. The WIMP annihilation process, which depletes the WIMP density, stops being efficient when the temperature is such that the interaction rate is comparable to expansion rate of the universe. From this point (known as "freeze-out") on-wards the WIMP density stabilizes as the universe cools and expands, leaving the current ("relic") density [31].

1.3 Direct detection of WIMPs

Three routes in which particle dark matter could be detected are shown in Fig. 1.6. In what follows specific focus shall be placed on the direct detection approach. This approach uses large masses of target material for WIMPs to scatter elastically on [33]. The rate, R, of this scattering is given by the product of the interaction cross-section, σ, the number density of WIMPs with average speed $<v>$ relative to the target nuclei, $n_\chi<v>$, and the number of target nuclei, N_T in the detector:

$$R = \sigma N_T n_\chi <v>. \tag{1.2}$$

Incorporating the range of recoil energies a specific detector is sensitive to, it is useful to consider the differential scattering rate with respect to recoil energy, E_R, in terms

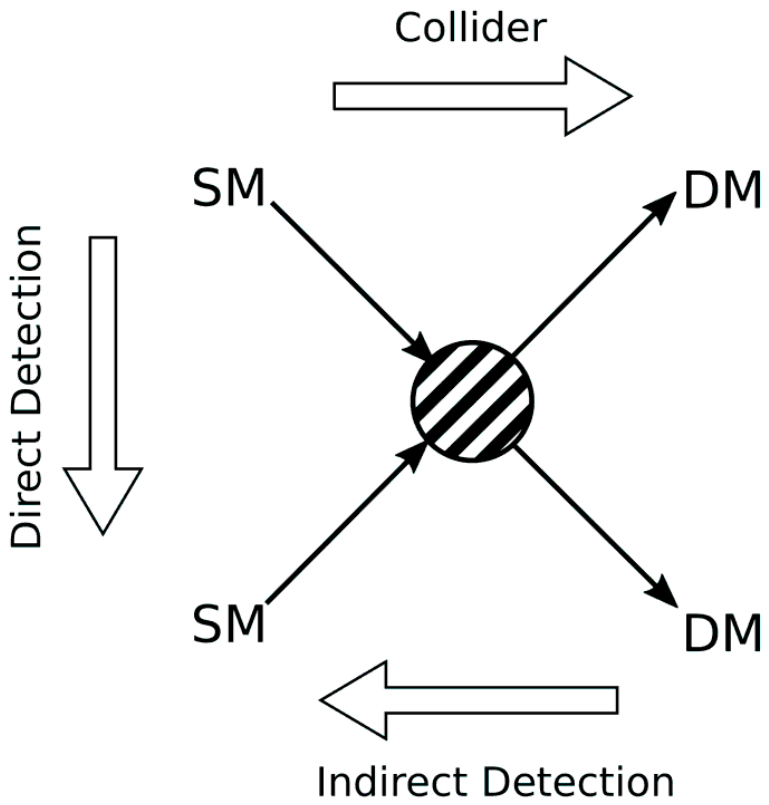

Figure 1.6: Simplified Feynman diagram of WIMP interaction with the standard model. Direct detection: Observe interaction between WIMP and standard model particle. Indirect detection: Annihilation products with no standard model source. Collider Production: Missing energy or momentum measured from standard model annihilation producing WIMPs. Figure adapted from Ref. [32].

of momentum transfer, q, between the target nucleus and the WIMP [33]:

$$\begin{aligned} \frac{dR}{dE_R} &= \frac{2\rho_0}{m_\chi}\int_{v_{min}}^{\infty} v f(\vec{v})\frac{d\sigma}{dq^2}dv, \\ q &= \sqrt{2m_T E_R}. \end{aligned} \tag{1.3}$$

Here m_χ is the WIMP mass, m_T is the mass of the target nuclei, ρ_0 is the local WIMP density, $f(\vec{v})$ is the WIMP velocity distribution, and v_{min} is the minimum WIMP speed required to produce a recoil of E_R.

In order to obtain the expected rate for any given detector, one must determine the the differential cross-section, local WIMP density, and the WIMP velocity dis-

tribution. A more detailed discussion of these factors is provided in the following sections.

1.3.1 Local Astrophysical Parameters

The local dark matter density, ρ_0 is crucial to determining the expected scattering rate and is directly proportional to it. The dark matter density of galaxies is typically measured with rotation curves. This is difficult in the case of the earth where the observer is in the galaxy being observed. Two general approaches are used; local and global. Local measurements use tracer stars near the sun, whilst global measures use ensembles of data sets to constrain a parameterised model of the milky way [34]. The local dark matter density extracted from these measures is $\rho_0 \approx 0.3$ GeV/cm^3. This is the value which has typically been used, though recent measurements from Gaia suggest a value of 0.5 GeV/cm^3. Therefore the adopted value may change in the years to come [35].

A variety of models are typically used for the velocity distribution. For this work, only the Standard Halo Model (SHM) [36] is considered as this model has been adopted and agreed upon by dark matter experiments [37]. In this model, the WIMP velocity distribution is assumed to be an isotropic Maxwell-Boltzmann distribution. The dispersion of this distribution is defined by the magnitude of the orbital velocity at the location of the sun, $\vec{v}_0$, the peculiar velocity of the sun, $\vec{v}_*$, and the earths velocity relative to the sun, $\vec{v}_+$. The requirement of dark matter being gravitationally bound in the galaxy imposes an upper limit of the galactic escape speed, v_{esc}. The resulting velocity distribution is:

$$f(\vec{v}) \;=\; \frac{1}{\sqrt{\pi}v_0} e^{-2\frac{|\vec{v}+\vec{v}_0+\vec{v}_*+\vec{v}_+|^2}{v_0^2}} \;\Theta(v_{esc} \;-\; |\vec{v}+\vec{v}_0+\vec{v}_*+\vec{v}_+|), \tag{1.4}$$

where $\Theta(x)$ is the Heaviside step function which imposes the upper speed limit. Com-

monly accepted values for these parameters, as detailed in Ref. [37] are summarised in Table 1.1.

Parameter	Description	Value
ρ_0	Local dark matter density	0.3 GeV/cm^3 [38]
v_{esc}	Galactic escape speed	544 km/s [39]
$\lvert\vec{v}_+\rvert$	Average galactocentric Earth speed	29.8 km/s [40]
$\vec{v}_*$	Solar peculiar velocity	(11.1, 12.2, 7.3) km/s [41]
$\vec{v}_0$	Local standard of rest velocity	(0, 238, 0) km/s [42]

Table 1.1: Values of Standard Halo Model parameters suggested by [37].

1.3.2 Differential cross-section and Form Factors

The differential cross-section for elastic scattering has two components which are non-vanishing in the zero-momentum limit; a spin-independent (SI) and spin-dependent (SD) component [43]. These two components are generally considered independently for experimental simplicity, with the SI component arising from scalar coupling of the WIMP to quarks and gluons, whilst the SD component is the result of axial-vector coupling [33]. Hence the differential cross-section is:

$$\begin{aligned} \frac{d\sigma}{dq^2} &= \left(\frac{d\sigma}{dq^2}\right)_{SI} + \left(\frac{d\sigma}{dq^2}\right)_{SD}, \\ \frac{d\sigma}{dq^2} &= \frac{1}{4\mu^2 v^2}\left(\sigma_0^{SI} F_{SI}^2(q) + \sigma_0^{SD} F_{SD}^2(q)\right). \end{aligned} \tag{1.5}$$

Here $\sigma_0^{SI,SD}$ are the SI and SD cross-sections corresponding to zero-momentum transfer, μ is the WIMP-nucleus reduced mass, and $F_{SI,SD}(q)$ are the SI and SD nuclear form factors.

In the SI case, isospin is assumed to be conserved such that WIMP coupling with protons and neutrons is very similar, resulting in:

$$\sigma_0^{SI} = \left(\frac{\mu}{\mu_n} A\right)^2 \sigma_n, \tag{1.6}$$

where μ_n is the WIMP-nucleon reduced mass, A is the atomic mass of the target nuclei, and σ_n is the WIMP-nucleon cross-section [33].

The nuclear form factor, $F(q)$, encapsulates the momentum dependence of the cross-section and is a Fourier transform of the density distribution within the nucleus. The SI form factor used is the Helm form factor, in which the nucleus is modeled as a solid sphere of radius r_N with smooth nucleon density given by a gaussian of width s [38].

$$F_{SI}^2(q) = \frac{3j_1(qr_N)}{qr_N} e^{-(qs)^2/2}. \tag{1.7}$$

For SD interactions, the unequal coupling between WIMPs and protons/neutrons means the choice of form factor has a large impact on WIMP sensitivity. In addition this unequal coupling also impacts the form of σ_0^{SD}. These are discussed in detail in Ref. [44, 45, 46].

Hence the resulting SI WIMP-nucleon differential cross-section and scattering rate are given by:

$$\left(\frac{d\sigma}{dq^2}\right)_{SI} = \frac{A^2\sigma_n}{4\mu_n^2 v^2} F_{SI}^2(q), \tag{1.8}$$

$$\left(\frac{dR}{dE_R}\right)_{SI} = F_{SI}^2(q) \frac{\rho_0 A^2 \sigma_n}{2\mu_n^2 v^2 m_\chi} \int_{v_{min}}^{\infty} \frac{f(v)}{v} dv. \tag{1.9}$$

An analogous derivation of the SD differential cross-section and scattering rate is given in Ref. [44, 45].

Given the observational and theoretical motivations detailed in this chapter, a variety of experiments have been devised to achieve direct detection of dark matter. Due to the low interaction rate of dark matter expected based on astrophysical observations, major requirements for these experiments include low background rates, aided by the use of ultra clean detector components to reduce the presence of radioactive contaminants, and a large target mass. One such endeavour is the xenon based LUX-ZEPLIN (LZ) experiment, on which this work focuses. The following chapters report

efforts by the author studying photo-multiplier tubes (PMTs), which observe interactions in the target material of LZ, an overview of the LZ detector, measurements informing the background model for LZ, an exploration of fast neutron identification via proton recoils, and the first science result of LZ.

CHAPTER II

The Lux-Zeplin Experiment: Overview and Detector Assembly

LUX-ZEPLIN (LZ) is a second generation direct detection experiment, situated 4850 feet (1.48 km) underground in the Davis Cavern at the Sanford Underground Research Facility (SURF). The LZ detector consists of a dual phase Xenon (Xe) time projection chamber (TPC) as the primary WIMP detector, and an active veto to reject neutrons and gammas. The active veto is comprised of two sub-detectors; an instrumented LXe "skin" region between the TPC and the inner cryostat vessel, and a gadolinium-loaded liquid scintillator (GdLS) contained in acrylic tanks. The GdLS tanks enclose the titanium cryostat, forming a near hermetic detector. Signals from all sub-detectors are observed by photo-multiplier tube (PMT) arrays.

A schematic of the detector is shown in Fig. 2.1 [47]. LZ was assembled within a water tank of height 591 cm and radius 381 cm to further shield from the radioactivity of the cavern rock. The water tank, which housed LZ's predecessor LUX, is further shielded by six octagonal steel plates, each 2 inches thick, in the shape of an inverted pyramid, that is inlaid in the floor beneath the tank.

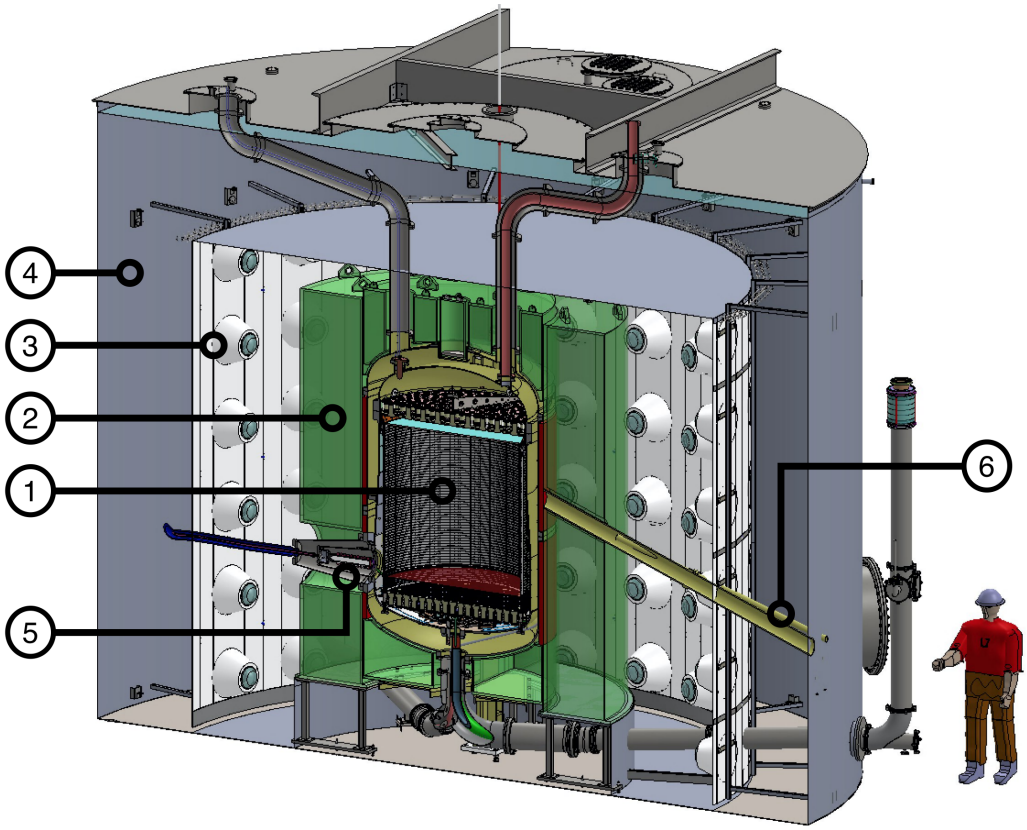

Figure 2.1: Major subsystems of the LZ detector. Rendering of the LZ experiment, showing the major detector subsystems. At the center is the liquid xenon TPC (1), monitored by two arrays of PMTs and serviced by various cable and fluid conduits (upper and lower). The TPC is contained in a double-walled vacuum insulated titanium cryostat and surrounded on all sides by a GdLS Outer Detector (2). The cathode high voltage connection is made horizontally at the lower left (5). The GdLS is observed by a suite of 8" PMTs (3) standing in the water (4) which provides shielding for the detector. The pitched conduit on the right (6) allows for neutron calibration sources to illuminate the detector. Figure from Ref. [48].

2.1 Xenon Time Projection Chamber

The LZ TPC contains 7 tonnes of liquid Xe (LXe) as well as a layer of gaseous Xe (GXe) at the top of the TPC. The walls of the TPC are lined with PTFE to improve light collection, with the whole assembly housed in two nested low radioactivity Titanium (Ti) cryostat vessels [49]. The inner cryostat vessel (ICV) contains both the TPC and the skin, with an insulating vacuum layer between the ICV and the outer cryostat vessel (OCV). Scattering events in the LXe create both a prompt scintillation

signal (S1) and free electrons, via ionization of the Xe, which, under application of an electric field, drift up to the LXe surface and are extracted into the GXe. These electrons produce a proportional scintillation signal (S2) as they accelerate in the GXe. These signals are shown in Fig. 2.2. Two arrays of PMTs (above and below the central TPC region) detect the S1 and S2 light. The time delay between the S1 and S2 signal gives a measure of the z position of the interaction, whilst the pattern of S2 light incident on the top PMT array is used to determine the x, y position of the interaction [47]. The S1 and S2 signal sizes are given by the area of the observed pulses which is proportional to the number of photo-electrons observed in the PMTs. They are typically reported in units of 'phd' which is the pulse area normalized to the area of single photo-electrons obtained using LED calibrations.

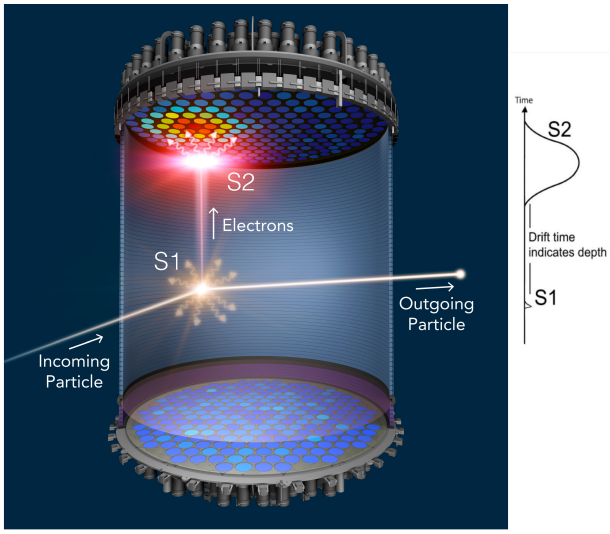

(a) Figure from Ref. [47].

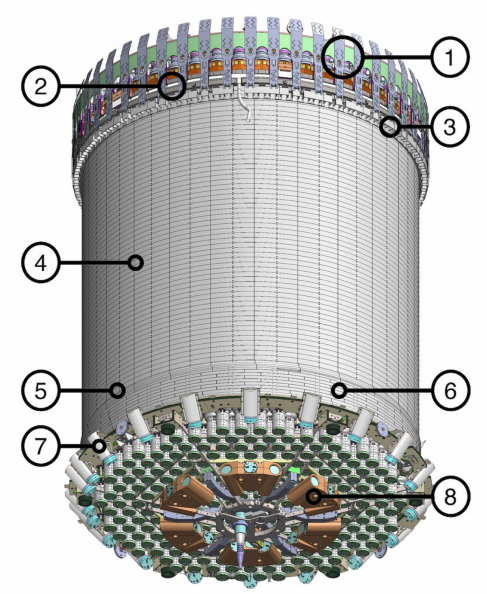

(b) Figure from Ref. [48].

Figure 2.2: Dual phase Xe TPC operating principle. **2.2a:** Prompt scintillation (S1) and delayed ionization signal in GXe (S2) produced by interactions in the LXe. **2.2b:** TPC design and components: 1-Top PMT array; 2-Gate-anode and weir region (liquid level); 3-Side skin PMTs (1-inch); 4-Field cage; 5-Cathode ring; 6-Reverse field region; 7-Lower side skin PMTs (2-inch); 8-Dome skin PMTs (2-inch).

Xenon has few radioactive isotopes, high scintillation yield, and impressive self

shielding properties. By this it is meant that γs and neutrons which penetrate into the LXe cryostat are effectively screened, with mean interaction lengths of $\mathcal{O}(5$ cm) and $\mathcal{O}(10$ cm) respectively for MeV scale particles in the LXe volume. This is shown in Fig. 2.3.

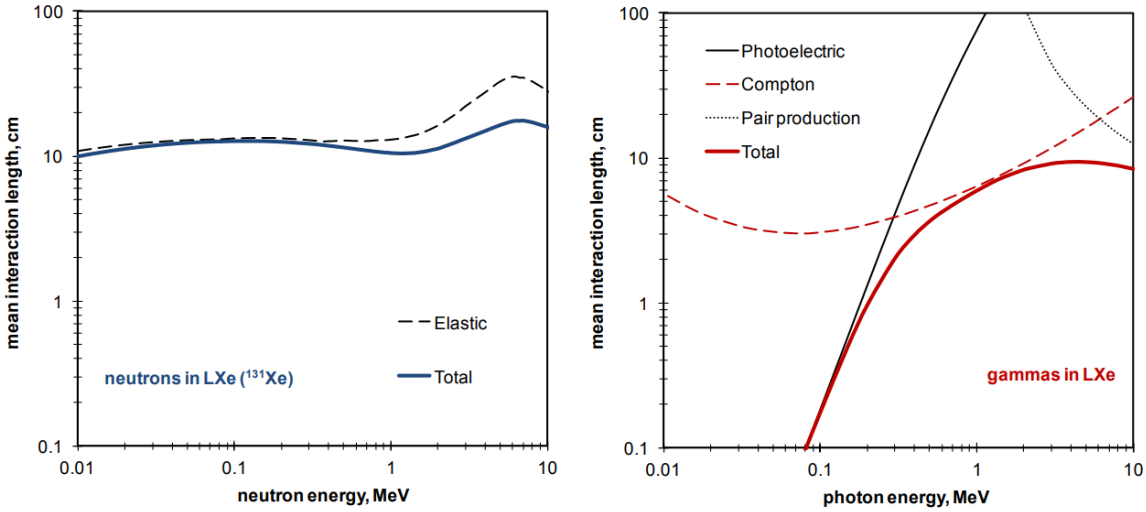

Figure 2.3: Mean interaction lengths for neutrons [50] and γrays in LXe.

2.1.1 Xenon Particle Interactions

What follows is a brief summary of the scintillation mechanism in Xe; a more detailed and thorough treatment is given in Ref. [51]. Particles traversing a Xe medium can interact with either the atomic nucleus, producing a nuclear recoil (NR), or the electron cloud surrounding it, producing an electronic recoil (ER). These both result in the recoiling particle scattering and transferring energy to nearby Xe nuclei and atomic electrons via excitation or ionisation, which go on to do the same, initiating a cascade of secondary interactions. The final result of this cascade is the production of scintillation light.

Excited Xe atoms bind with ground state Xe to form an electronically and vibrationally excited molecule, the excimer denoted as $(Xe_2^{*\nu})$. Energy in the vibrational modes of this excimer is lost through collisions with other Xe atoms, after which the

electronic excitation energy is released as a VUV photon. This chain of events from excitation to luminescence is shown below:

$$e^- + Xe \rightarrow Xe^* + e^-, \qquad \text{(initial excitation)}$$

$$Xe^* + Xe \rightarrow Xe_2^{*\nu}, \qquad \text{(producing excimer)}$$

$$Xe_2^{*\nu} + Xe \rightarrow Xe_2^* + Xe, \qquad \text{(relaxation)}$$

$$Xe_2^* \rightarrow Xe + Xe + \gamma. \qquad \text{(VUV emission)}$$

The process for ionised Xe atoms differs with increased complexity. In this situation, the ionised atom forms a diatomic xenon ion with nearby neutral Xe atoms. Some ionisation electrons produced in the cascade of secondary interactions recombine with the molecule, after which it splits forming a highly excited Xe atom. This atom relaxes to a less excited atom, forms an excimer with a neighbouring atom and de-excites in a similar manner to the excitation luminescence excimer. The full process of recombination luminescence is:

$$e^- + Xe \rightarrow Xe^+ + 2e^-, \qquad \text{(initial ionisation)}$$

$$Xe^+ + Xe \rightarrow Xe_2^+, \qquad \text{(producing diatomic ion)}$$

$$e^- + Xe_2^+ \rightarrow Xe^{**} + Xe, \qquad \text{(recombination)}$$

$$Xe^{**} + Xe \rightarrow Xe^* + Xe + heat, \qquad \text{(relaxation)}$$

$$Xe^* + Xe \rightarrow Xe_2^{*\nu}, \qquad \text{(producing excimer)}$$

$$Xe_2^{*\nu} + Xe \rightarrow Xe_2^* + Xe, \qquad \text{(relaxation)}$$

$$Xe_2^* \rightarrow Xe + Xe + \gamma. \qquad \text{(VUV emission)}$$

The energy deposited in the initial interaction can be written as a function of the

number of excited atoms (n_{ex}) and ionised atoms (n_i):

$$E = \frac{W}{L}(n_{ex} + n_i) \tag{2.1}$$

Where W is the average energy required to produce a single excited/ionised atom, which has a value of 13.7±0.2 eV in LXe [52]. The parameter L is the Linhard factor (quenching) which accounts for fraction of the initially deposited energy lost to heat, which typically has the value 1 for ERs [53].

The areas of S1 and S2 pulses are proportional to n_{ex} and n_i respectively. The constants of proportionality are g_1 and g_2, which are determined by the S1 light collection efficiency and electron extraction efficiency respectively. Thus the energy deposited, as a function of pulse area is given by:

$$E = \frac{W}{L}(\frac{S1}{g_1} + \frac{S2}{g_2}). \tag{2.2}$$

2.1.2 Discriminating ERs from NRs

Discriminating between ERs and NRs is key for discovery, since ERs are major source of background for the NR WIMP signal. The major difference between measurements of these two interactions is the ratio of S2 to S1 light. In plots of $\log_{10}$(S2) against S1, as shown in Fig. 2.4, ERs and NRs each form bands, with the NR band falling at lower $\log_{10}$(S2). The overall separation of the bands is due to NRs producing less ionization and more direct excitation (source of prompt scintillation signal) than ERs [51, 54]. The band-widths are largely dependent on electron-ion recombination rates at the interaction site [51]. As a result, initial ionization is either measured as S2 or S1, and fluctuations in recombination rates is one of the primary causes of the band broadening.

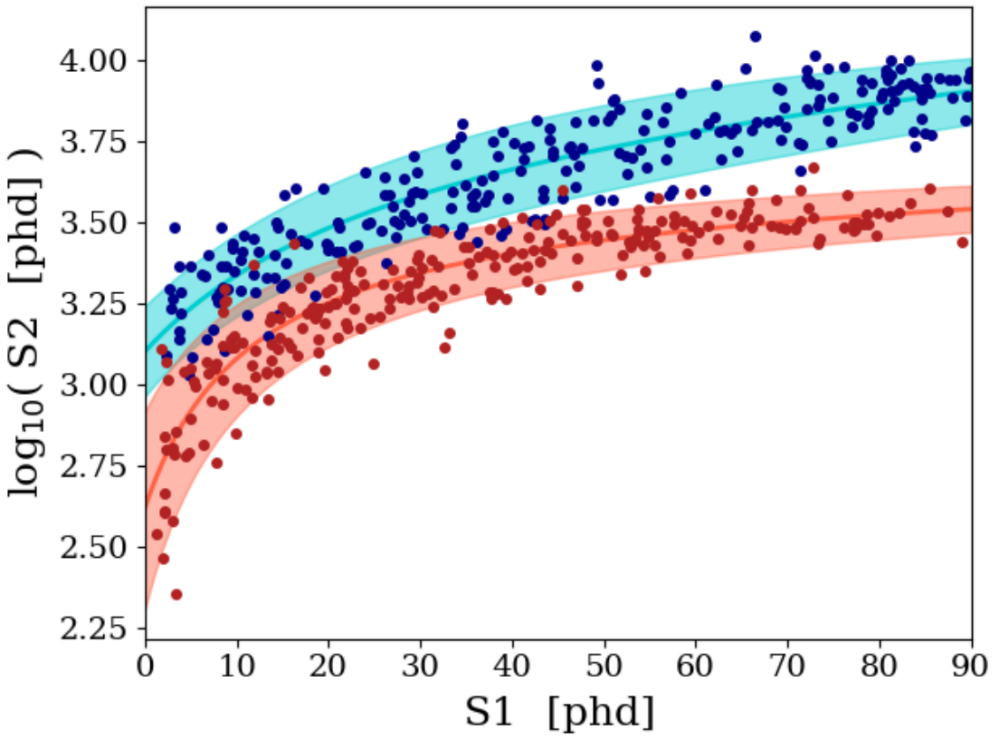

Figure 2.4: Discrimination between ERs (blue) and NRs (red) in $\log_{10}$(S2) vs S1 space. Solid lines are band means with shaded regions showing 90-10 % confidence level regions for each. Figure adapted from Ref. [54].

2.2 Xe Skin

The skin region surrounding the TPC contains 2 tonnes of LXe and provides a crucial coincidence veto for gamma interactions the TPC. This region not only provides insulation from the grounded titanium vessel, its 131 PMTs, located in the side and bottom dome of the skin region, are capable of observing scintillation from gammas passing through. The skin contains 93 1-inch Hamamatsu R5820 PMTs at the top of the side skin looking down and 38 2-inch Hamamatsu R8778 PMTs; 20 at the bottom of the side skin looking up, and 18 in the bottom dome region below the TPC (see Fig. 2.2b). The walls of this region are lined with PTFE to maximize light collection.

2.3 Outer Detector

Neutrons can scatter elastically on Xe nuclei, producing NRs just like WIMPs would be expected to. This makes them a particularly dangerous background. However, since neutron interactions with nuclei have a higher cross section than that of WIMP, one can tag this background by disregarding multiple scatters. These additional scatters can occur within the TPC or nearby, hence having further radiation detectors surrounding the TPC grants superior discriminating power for this background. This is the primary goal of the OD system.

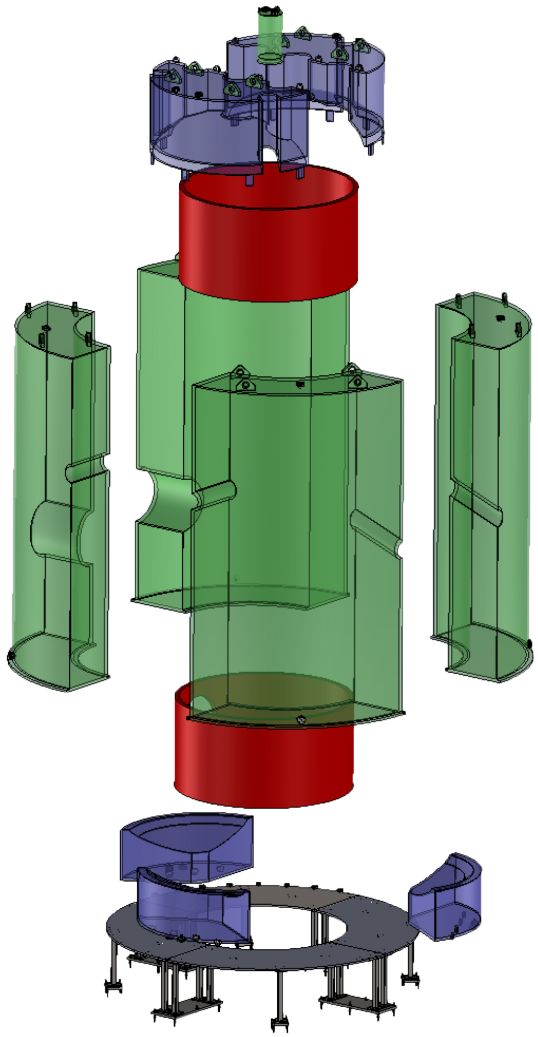

Figure 2.5: Exploded view of all OD acrylic tanks. **Red**: Water displacement spacers (foam). **Green**: Side acrylic tanks. **Indigo**: Top and Bottom acrylic tanks.

In the water tank a cylindrical wall of PMTs surrounds 9 acrylic tanks containing the GdLS. These tanks, shown in Fig. 2.5, surround the titanium cryostat vessel housing the skin and TPC.

2.3.1 Organic Scintillator Particle Interactions

When particles travel through a scintillating medium they interact, leaving a trail of ionized/excited molecules in their wake, losing energy as they do so [55]. Broadly speaking, the ionized/excited molecules left by particle tracks form triplet or singlet states then decay back to ground producing photons.

The characteristic decay times of the singlet states formed are shorter than those of the triplet states. This results in the light signal decaying with two characteristic times, a fast component and a slow one [55]. By measuring the decay time of a scintillator signal, one can thus determine the relative populations of the singlet and triplet states from a given interaction. Since ionization preferentially populates the triplet states, this property can be used to distinguish different kinds of interacting particles based on the time signature of the light signal. This is the basis of pulse shape discrimination in organic scintillators [56, 57].

If one ignores interactions between ionized molecules, the light yield (L) produced is proportional to the total energy (E) deposited in the scintillating medium. The total energy deposited is given by the path integral of the differential energy dissipated, $\frac{dE}{dx}$, which comes from the Bethe-Bloch formula [58, 59].

$$L \;=\; S \int \frac{dE}{dx}\, dx, \tag{2.3}$$

where x is the path length of the particle in the scintillator and S is the scintillation efficiency. This relation holds particularly well for cases such as fast electrons, which have low energy loss per path length $\frac{dE}{dx}$ and the excited/ionized molecules it leaves

in its wake are relatively well separated. However, at lower energies, one observes deviation from linearity due to increases in $\frac{dE}{dx}$. This is a result of a $1/v^2$ dependence in the Bethe-Bloch formula. This deviation is stronger for heavy charged particles such as protons, and α-particles, and ions with elevated $\frac{dE}{dx}$. Higher $\frac{dE}{dx}$ from charged particles means a higher density of ionized/excited molecules in the path. Thus the assumption of negligible interactions between them is no longer valid.

Birks, after conducting measurements on anthracene crystals, proposed a semi-empirical model which introduces terms to model light yields when $\frac{dE}{dx}$ is elevated [60]. The result of this modification is

$$L \;=\; S \int \frac{\frac{dE}{dx}}{1 \;+\; kB\frac{dE}{dx}}\; dx. \tag{2.4}$$

The constant k is the quenching parameter modelling the effect of ionization quenching. The term BdE/dx is the specific ionization density, with B as a constant. In usual parlance on this topic, the product of these two parameters kB, is referred to collectively as Birks' parameter.

Whilst Birks' law has been incredibly fruitful in describing more completely the non-linear aspects of scintillation light yield, a further adaptation was made by Chou [61]. In this adaptation the ionization quenching term is modelled by a second order polynomial, rather than a first order one:

$$L \;=\; S \int \frac{\frac{dE}{dx}}{1 \;+\; kB\frac{dE}{dx} \;+\; C\left(\frac{dE}{dx}\right)^2}\; dx. \tag{2.5}$$

This results in improved agreement between the model and measurement data. A higher order correction to Birks' original formulation is parameterized by the quadratic term C.

Component	Function	Mass Fraction (%)
$C_{17.14}H_{28.28}$ (LAB)	neutron/gamma	99.25
C_15H_11NO (PPO)	Primary Fluor/wavelength shifter	0.35
C_24H_22 (Bis-MSB)	Wavelength shifter	0.002
$C_9H_17O_2^-$ (TMHA)	Chelation	0.3
Gadolinium (Gd)	neutron capture	0.1

Table 2.1: Components of the GdLS mixture

2.3.2 Scintillator composition

The composition of the GdLS mixture is shown in Table 2.1. Linear-alkylbenzene (LAB) is a solvent which forms the base of the liquid scintillator mixture. In addition to this, the fluor 2,5-diphenyloxazole (PPO), and the wavelength shifter 1,4-bis(2-methylstyryl(benzene)) (Bis-MSB) are included. The LAB component is excited as particles pass through the LS depositing energy.

The excited LAB generally transmits this energy to the fluor through a series of chemical reactions which become available in the excited LAB state, as described in Section 2.3.1. The now excited fluor emits light at wavelengths up to 380 nm. The LS has a short absorption length for these wavelengths, thus this light never makes it to PMTs for detection. The Bis-MSB is included to mitigate this effect. It acts as a secondary wavelength shifter, absorbing the photons produced by PPO, and emitting at wavelengths with much longer absorption lengths as well as more overlap with the PMT sensitivity spectrum. Below 380 nm, the absorption length is approximately 1 m, whilst after wavelength shifting to 410 - 425 nm the absorption length extends to over 10 m. This mixture has a high light yield of 9,000 photons/MeV. The Birks' law (Eq. 2.5) parameters LZ adopts are shown in Table 2.2. The measurements these values came from use a strikingly similar mix to LZ.

As previously stated, this mixture is loaded with Gd at a mass fraction of 0.1% in order to improve both the efficiency and intensity of the neutron capture signal. In order to keep the Gd dissolved in solution, it is bound to the chelating agent

	S (photons/MeV)	kB	C
β/γ	9000	0.03	0
proton	9000	8.26E-3	0
α	9000	4.63E-3	1.77E-6

Table 2.2: Parameters of the modified Birks' law for GdLS. Values from Ref. [62] using a near identical LS composition to LZ.

3,5,5-trimethylhexanoic acid (TMHA) in a 3:1 ratio. This results in the complex $Gd(C_9H_17O_2^-)_3$.

2.3.3 Neutron capture in the OD

Gadolinium, namely ^{155}Gd(60 kb[63]) and ^{157}Gd(254 kb[63]), has the highest thermal neutron capture cross section (49 kb[1]) of any known stable element [64]. Hence it is the ideal doping agent to maximize visibility of neutrons scattered in the TPC. Due to this high cross section, only a small concentration of Gd is required (0.1% by mass). Approximately 87% of neutrons which reach thermal energies in the scintillator are captured on Gd releasing 8 MeV in a cascade of 4-5 γ rays [63]. See Fig. 2.6 for and example schematic of this emission process. With a light yield of 9,000 photons/MeV, even a 10% energy deposit from the neutron capture process leads to emission of O(1000) photons, which will reliably produce a significant signal in the water PMTs.

Hydrogen also produces a prominent neutron capture signal. Whilst the 0.3 b thermal neutron capture cross section of hydrogen is dwarfed by Gd, due to its abundance in the organic molecules in the GdLS, the acrylic, and the surrounding water, it constitutes a significant portion of the expected neutron captures observed. Upon capture of thermal neutrons, a single 2.2 MeV gamma is emitted by an excited deuterium decaying to its ground state [65]. Within the scintillator the bulk of remaining thermalised neutrons which do not capture on Gd capture on hydrogen[2]. The captures

[1] Abundance weighted average across all naturally occurring isotopes

[2] Other isotopes contribute to this count, but with negligible probability.

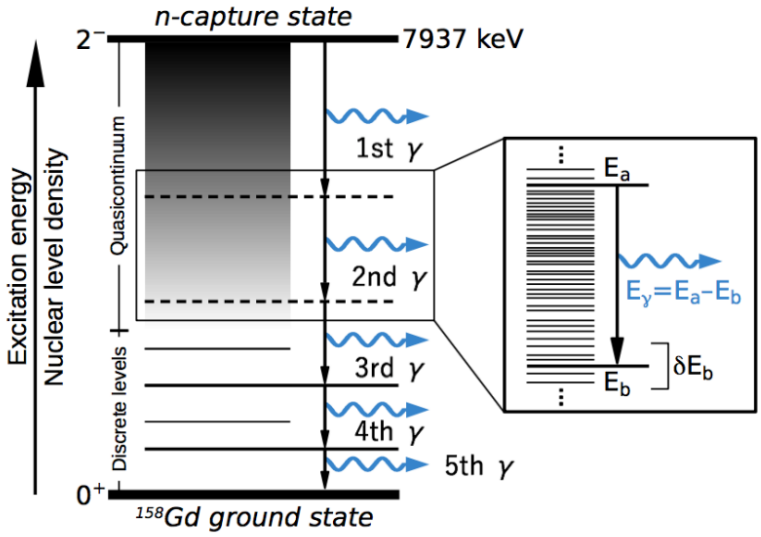

Figure 2.6: Decay schematic of ^{158}Gd after neutron capture on ^{157}Gd [63].

which occur on hydrogen outside of the acrylic tanks contribute much less since the resulting gamma must penetrate through the water shield before depositing energy in the GdLS, resulting in a much smaller signal for those which survive this journey. In addition, cavern background gammas mainly from the ^{238}U, ^{232}Th, and ^{235}U decay chains act as a background to this capture signal. The 2.6 MeV gamma from ^{208}Tl in the ^{232}Th decay chain is a particular example. This is not a major problem for the Gd capture signal since the cavern gamma spectrum has negligible rate at the high emission energies of Gd capture[3].

With hydrogen capture alone, neutrons thermalise and capture in the OD over approximately 220 μs. The addition of Gd, with its superior capture cross-section, reduces this time to approximately 28 μs. Hence neutron NR signals in the TPC can be identified by a corresponding neutron capture signal in the LS within approximately 500 μs of the TPC signal [47]. This window is set much larger than the expected thermalisation timescale to account for time spent by neutrons outside of the GdLS.

[3]Pile-up of lower energy gammas could mimic such a large signal, though this would be a second order effect.

2.3.4 OD PMTs, Tyvek Reflectors, & Optical Calibration System (OCS)

Surrounding the acrylic tank containing the GdLS are 120 Hamamatsu 8-inch R5912 photo-multiplier tubes (PMTs), used to detect scintillation light, arranged as shown in Fig. The R5912 PMTs have 10 linearly focused dynode stages, and a peak quantum efficiency of 25% (See Fig. 2.7). This model was chosen for its very good charge resolution, and the excellent correlation between the emission spectrum of GdLS and the R5912 efficiency and sensitivity spectrum, with the PMT quantum efficiency remaining above 20% for the full emission spectrum of the GdLS.. A comparison of the GdLS optical properties and the PMT sensitivity is shown in Fig. 2.7.

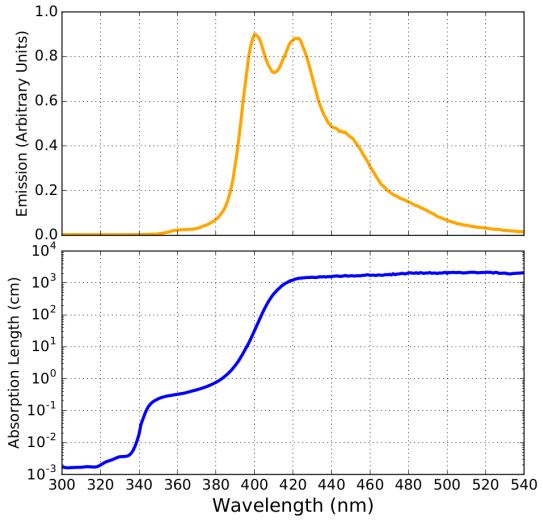

(a) GdLS emission spectrum (Top) and absorption length (Bottom) [66]

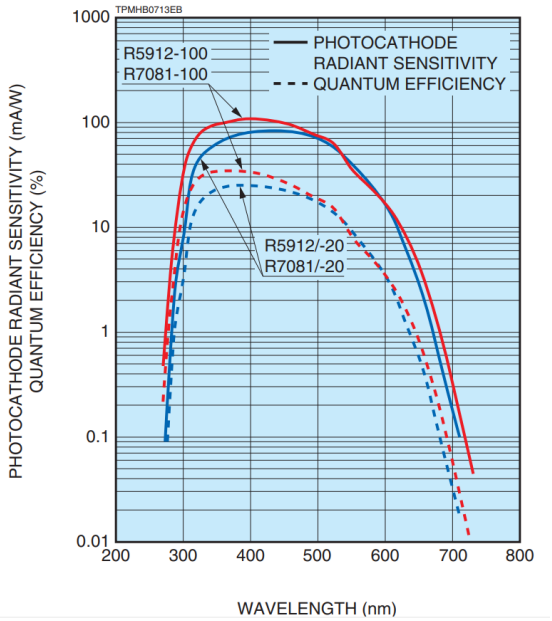

(b) R5912 PMT photo-cathode sensitivity [67].

Figure 2.7: Comparison of GdLS optical properties and PMT photo-cathode efficiencies.

In addition, 3 rows of 10 equidistant optical fibres, connected to LEDs emitting 435 nm light, are placed in the PMT wall facing into the detector [68]. These fibres are to be used for calibration of the PMTs. Light from each fibre reflects on a Tyvek

surface covering the cryostat. Tyvek also lines the wall of PMTs with cut-outs for the PMTs. The addition of Tyvek provides a factor approximately 2.5 increase in light collection efficiency (LCE) over no reflector, leading to an average LCE of 7.4% [69]. Tyvek was chosen over other reflectors for its excellent reflectivity (above 80% in water), inexpensiveness, low impurity, and low radioactivity [70]. Due to Tyvek's diffuse reflectivity, light from each fibre reflects onto several PMTs. Additionally, there are 5 fibres and LEDs to monitor acrylic and GdLS degradation respectively. Four of these emit 450 nm light, to probe the GdLS degradation. A fifth 435 nm LED probes transmittance of the acrylic.

2.4 Calibration sources

To make sense of the LZ detector response and performance, and eventually experimental results, calibration sources are crucial. To this end a variety of radioactive sources are employed, both internal and external, to determine energy scale, threshold and photon detection efficiency. A summary of these sources is given in Table 2.3.

Source	Type	Function	Deployment
Tritium (CH_4)	β	ER	Injected
^{220}Rn	various αs	ER & Xe Skin	Injected
^{131m}Xe	164 keV γ	TPC (x,y,z) & Xe skin	Injected
^{83m}Kr	32.1 keV β/9.4 keV γ	TPC (x,y,z)	Injected
DD	272 keV & 2.45 MeV neutron	NR response	External
^{88}YBe	152 keV neutron	NR response	External
AmLi	(α, n)	NR response	CSD
^{252}Cf	spontaneous fission	NR response	CSD
^{57}Co	122 keV γ	Xe skin threshold	CSD
^{54}Mn	821 keV γ	ER	CSD
^{228}Th	2.615 MeV γ	OD energy scale	CSD
^{22}Na	β^+ (2x 511 keV γs)	Inter-detector timing	CSD

Table 2.3: Calibration sources utilized in LZ for the first science run [47, 48].

Internal sources consist of radioisotopes injected into the xenon and allowed to circulate. Injection allows these sources to mix evenly throughout the volume al-

lowing the detector response to be assessed across the entire volume. In addition, the self-shielding property of Xe means an external low energy source would require a large amount of time to accumulate sufficient statistics for interactions near the center. Mixing such sources in the Xe significantly expedites this process. Some of these injected sources are short lived alpha and gamma sources (^{131m}Xe, ^{220}Rn, and $^{8}3m$Kr), thus decay away quickly following the calibration period. Longer lived injection sources such as tritiated methane (CH_4) must be removed. This achieved by circulation through a hot gas getter [48].

The majority of external sources are placed in up to three vertical calibration source deployment (CSD) conduits [48]. The CSDs are located in the vacuum space between the ICV and OCV. Sources placed in these tubes hence emit radiation directly into the TPC (without first passing through the outer detector), and directly into the GdLS volume (without traversing the water shield).

In addition to these, a deuterium-deuterium (DD) neutron generator is employed outside the water tank. It operates as a directional source, producing 2.45 MeV and 272 keV neutrons. These neutrons are directed through a calibration tube passing through the OD to the OCV. A detailed description of the DD generator and its development is provided in [71]. Two such tubes are employed in LZ, one angled and one horizontal. A ^{88}YBe photo-neutron source is also deployed in a plug in the OD top tanks, for low energy neutron calibrations. A portion of the tank is removed and replaced with this plug during this calibration. This plug is shown in green above the top tanks in the exploded view of Fig. 2.5.

2.5 Data Acquisition System (DAQ)

Data acquisition systems perform the crucial task of deciding which data to write for further analysis. The PMT signals are passed through a shaping amplifier to increases the signal to noise ratio in the data. Additionally, the amplifier boards split

the signal and provide two levels of amplification. These two levels provide excellent visibility of small signals, without risking excessive saturation on large signals. After amplification, the signal is digitized using a series of 32 channel SkuTek DDC-32 digitizer boards. These digitizers provide a sampling rate of 100 MHz (10 ns samples). In order to avoid an overwhelming data rate, a Pulse Only Digitization (POD) approach is employed on each PMT channel independently. This utilizes the circular buffers on the DDC-32's with a firmware filter which digitizes the incoming signal when a data tuned threshold is met [72]. This threshold is based on SPE data and is set to provide and SPE detection efficiency of $> 99.9\%$. A simplified schematic overview of

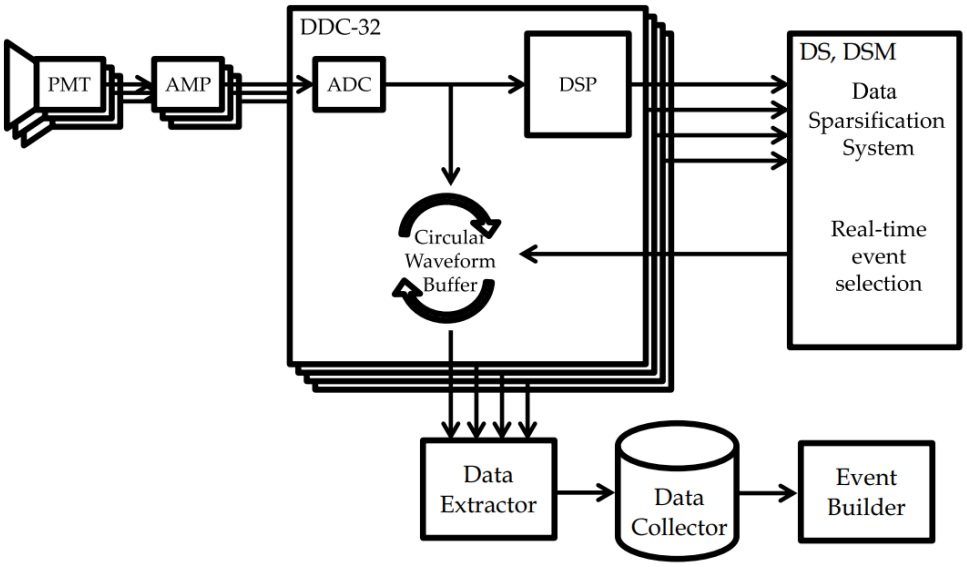

Figure 2.8: Schematic of the DAQ setup for LZ. [72]

the DAQ is provided in Fig. 2.8.

Further to this a series of tunable triggers are employed with the base architecture for this written to the board at the firmware level. These are:

- Random Trigger
- S1 Filter Trigger
- S2 Filter Trigger

(a) (b)

Figure 2.9: Electronics racks which house the DAQ system of LZ, during installation (**left**) and post installation (**right**).

- External Trigger

The random trigger simply captures events based on the output of an electronic noise generator. This is decoupled from the detector environment in order to obtain an unbiased sampling of events. The rate of this is fixed by adjusting the threshold the noise generated must cross in order to trigger the recording of an event.

The S1 filter trigger utilizes a double Hagenauer filter [72], with central region and side lobes of the same width. This trigger architecture is used primarily for independent triggers deployed in the veto detectors.

The S2 filter trigger is the primary trigger used for the WIMP search in the first science run. This trigger also uses a double Hagenauer filter, with differing central region and side-lobe widths, tuned to S2 pulses [72]. Events captured with this trigger contain the primary S1 pulse in the pre-trigger window. The veto decision is based on pulses in the veto detectors within the post-trigger window.

The external trigger is used during calibrations. It allows events to be captured based on an input signal from the LED systems for PMT calibrations, in addition to the DD generator.

2.6 Simulations

Simulations are a crucial part of experiment development and greatly aid the understanding and generation of both background and signal model probability distribution functions (PDFs) in addition to detector effects. An overview of the LZ simulation framework is shown in Fig. 2.10. LZ uses the BACCARAT[4][73] package

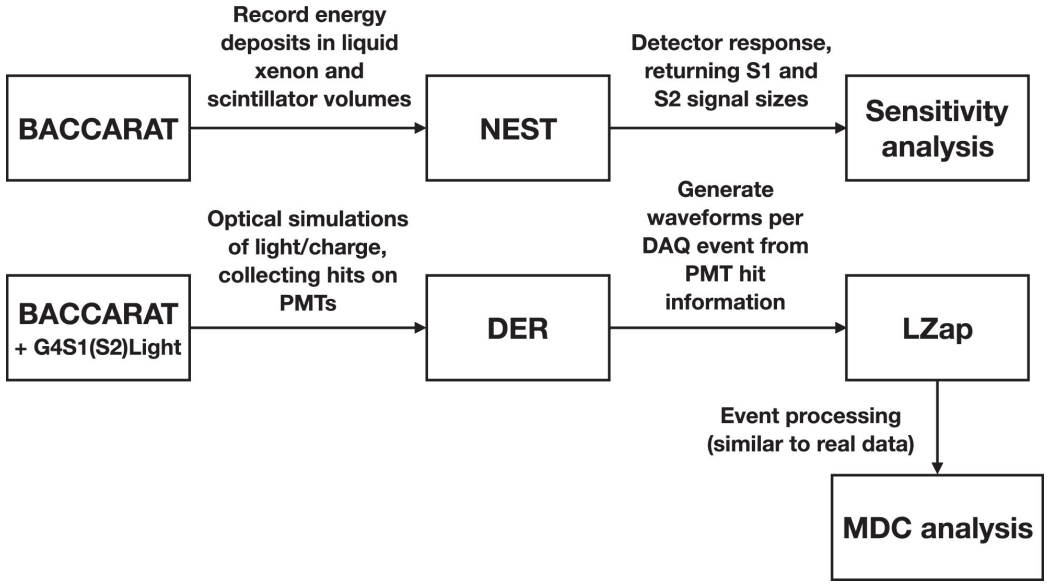

Figure 2.10: Simulations framework for LZ. G4S1(S2)Light referenced here are implementations of the NEST package. Figure from Ref. [73].

to simulate the particle interactions in the detector and the response of the detector. This package is built on the GEANT4 simulation package [74]. The LZ experiment is built as a detector geometry using the tools provided by GEANT4. In a simulation, particles are generated and propagated through the detector geometry, with interactions spawning new particles provided by GEANT. Energy deposits in the Xenon volumes are managed by the Noble Element Simulation Technique (NEST) model, which provide the expected conversion of these energy deposits to scintillation photons and ionization electrons [75]. NEST determines this using empirical models based on experimental measurements of noble elements, including Xenon. Energy

[4]**B**asically **A** **C**omponent-**C**entric **A**nalogue **R**esponse to **A**ny**T**hing.

deposits in other volumes are handled natively by GEANT4. One other deviation from standard GEANT4 handling of interactions is the neutron capture on Gd. Since GEANT4 has difficulty conserving Q-value and multiplicity of the gamma emissions from neutron capture, the DICEBOX toolkit is used for these processes [76, 77].

A custom software package, Detector Electronic Response (DER) is used to convert photons incident on PMTs to a simulated waveform signal. This package utilizes measurements of the PMT response (described in Chapter III) to generate these waveforms. Further to this DER implements the DAQ system described above in-silico. Thus the output of these simulations are a facsimile of the data one expects to be working with.

This DER output can then be processed using the same analysis package that is used on data. The LZ Analysis Package (LZAP) is a reconstruction software package using the gaudi framework [78] which processes the PMT signals recorded by the DAQ. Waveforms from the various PMTs in each sub detector are summed into detector pulses, using the gain and timing offset determined by calibration to normalize each PMTs signal. Detector pulses are created using a difference of gaussian filter to determine the start and end point of each summed pulse. A series of physics-ready reduced quantities (RQ) are calculated from these detector pulses. These RQs include parameter such as pulse height, pulse area, various prompt fractions (fraction of pulse area in the first t ns of the pulse), peak time, and more. Using these RQs a classification algorithm assigns pulses the labels: S1, S2, single electron (SE), single photo-electron (SPE), multiphotoelectron (MPE) and other. Once pulses are labeled in this fashion, a further algorithm classifies the event as either a single scatter, multiple scatter, pile-up or other. These labeled data along with selections on pulse level RQs are used to perform high level data analysis in order to achieve the physics goals of the LZ experiment.

2.7 Construction/Assembly of the LZ Detector

From 2017 to 2021, the author made a series of trips on-site trips (10 months cumulatively) to SURF to aid in the assembly and installation of LZ. A selection of these efforts are detailed pictorially in this section. These efforts begin with work on the Inner Cyostat Vessel (ICV), installing PTFE for the skin and aiding in the cleanliness monitoring prior to insertion of the TPC. Shown in Fig. 2.11 is the ICV being placed under nitrogen purge after a day of work in the class 1000 cleanroom. After each daily shift, the in progress detector was sealed in nylon with nitrogen flow

(a) Putting the TPC (in the ICV) under Nitrogen purge for the night in the lower part of the class 1000 cleanroom used for assembly of the TPC and Skin.

(b) The author in cleanroom garb, taking a moment to bask in the lack of glow from the ICV. Side Skin PMTs and PTFE reflectors are visible behind him.

Figure 2.11

in order to further minimize the introduction of radon gas to detector components. Once transported underground, the ICV with TPC inserted was instrumented with radiator blocks, RTDs (to monitor temperature), and Multi-layer insulation (MLI) to prevent thermal radiation into the cryogenic TPC (see Fig. 2.12).

Further to this, the author worked with the electronics group to install the electronic racks shown in Fig. 2.9. These racks house the vital organs of the LZ DAQ system described in the section above. This includes the uninterrupted power supply (UPS) providing backup power in the event of unexpected outage (installed at the

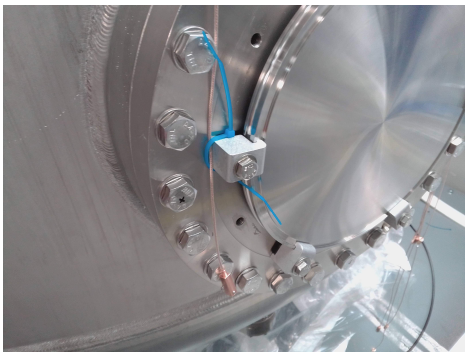

(a) Thermosyphon RTDs pictured near the HV port.

(b) MLI installed on the side of the ICV.

Figure 2.12: Insulation work on the ICV before insertion into the OCV.

same time as the pictured racks), the amplifier boards and DDC32 digitizers, along with data collectors.

In advance of the OD installation, the author spent significant time at their home institution fitting the PMTs with the Tyvek reflector cones, again to maximise light collection, and stainless steel assemblies known as 'spiders' which keep them attached to the stainless steel ladder frames. These spider frames are of the same design used in the OD test stand setup described in Chapter III. This work was also conducted in a class 1000 clean room and involved measurement of the resistivity of the PMT signal and HV cables as a quick assessment of the PMT base circuitry.

The PMTs are installed ladder by ladder top to bottom, using a winch system in teams of two to secure the PMTs in case of catastrophic loss of friction. The fruit of these efforts is the completed OD shown in Fig. 2.13[5]. Visible is the wall of OD PMTs with Tyvek cones attached to stainless steel frames lined with Tyvek curtains, the Tyvek lining on the OCV, as well as both the angled and horizontal DD conduit passing through the cut outs in OD acrylic tanks to the OCV awaiting its Tyvek cladding. After complete installation of the OD, all that remains is to calibrate

[5]It is left as an exercise for the reader to determine how this photo of the inside of the detector was obtained without stranding a member of the installation team for the duration of LZ's experimental run.

PMTs as installed and to fill the detector.

(a) Primary OD installation team taking a media break before completing and sealing the system.

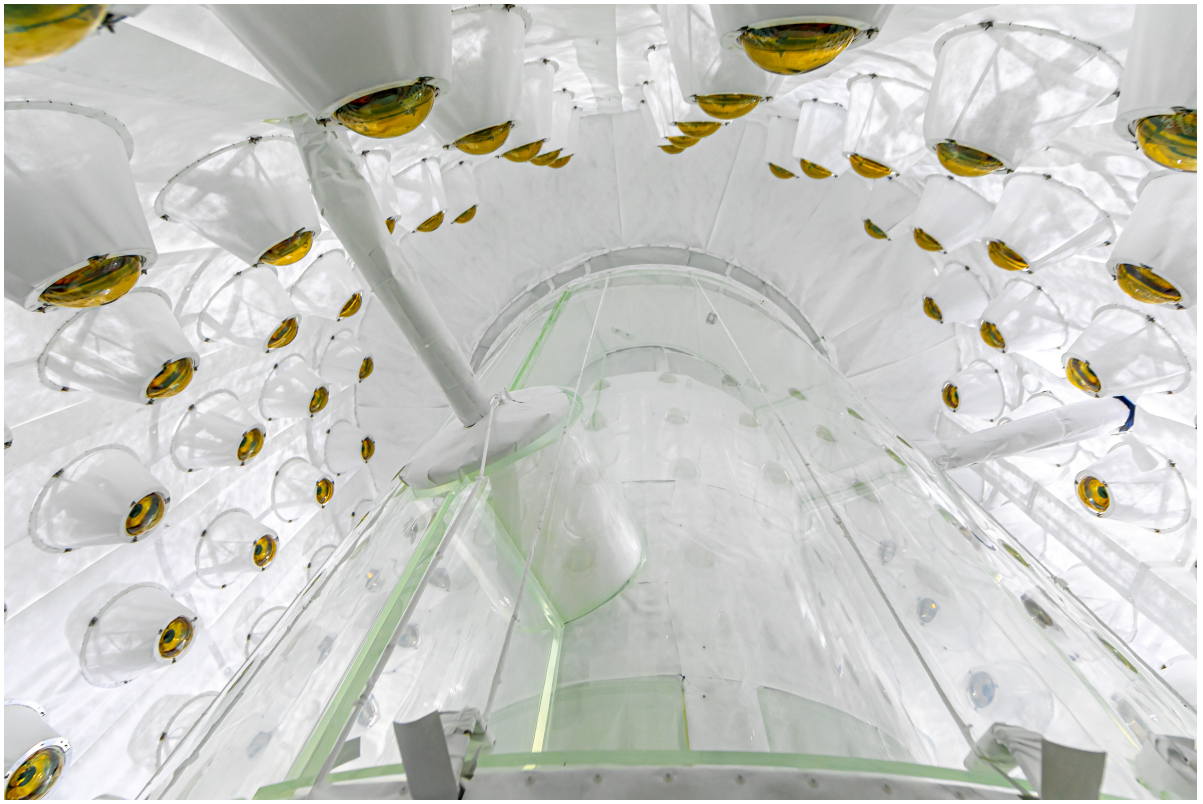

(b) Fully installed outer detector.

Figure 2.13: Completed outer Detector, before filling in its complete Tyvek clad glory (**2.13a**), along with the installation team prior to its completion (**2.13b**).

CHAPTER III

Photo-multiplier Tubes and the Outer Detector Test Stand

A water tank was set up to characterize and test the calibration procedures for the LUX-ZEPLIN OD PMTs. This consists of a stainless steel barrel of dimensions 115.6 cm × 40.0 cm × 0.5 cm (height × diameter × thickness), a Hamamatsu R5912 PMT (the same model used in the LUX-ZEPLIN outer detector), and an LED. A schematic and a photograph of this setup is shown in Fig. 3.1. Data from this setup is acquired using a SkuTek DDC10 digitizer board with a sample rate of 100 MHz (10 ns samples). In what follows a brief description of PMT operating principles is provided, in addition measurements of basic PMT properties are reported.

3.1 Photo-multiplier Tube Basics

The key operating physical phenomena which underpins the function of PMTs is the photoelectric effect. In short, a photon of appropriately high energy may excite an electron from the valence band of a material to the vacuum level. The energy required to do this is known as the work function of the material. The exciting photon must provide enough energy to excite the electron beyond the forbidden-band gap which electrons may not occupy, in addition to the interval between the conduction band

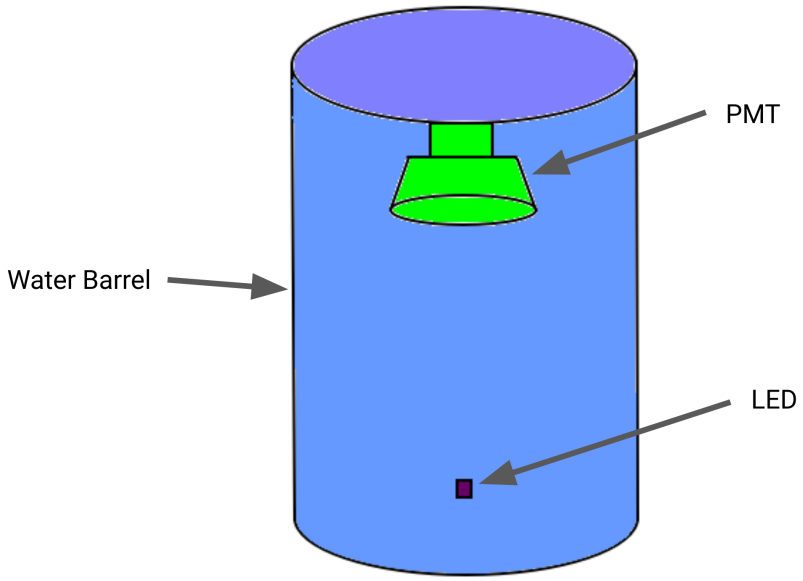

(a) Simple schematic of OD Test Stand showing PMT and calibration LED.

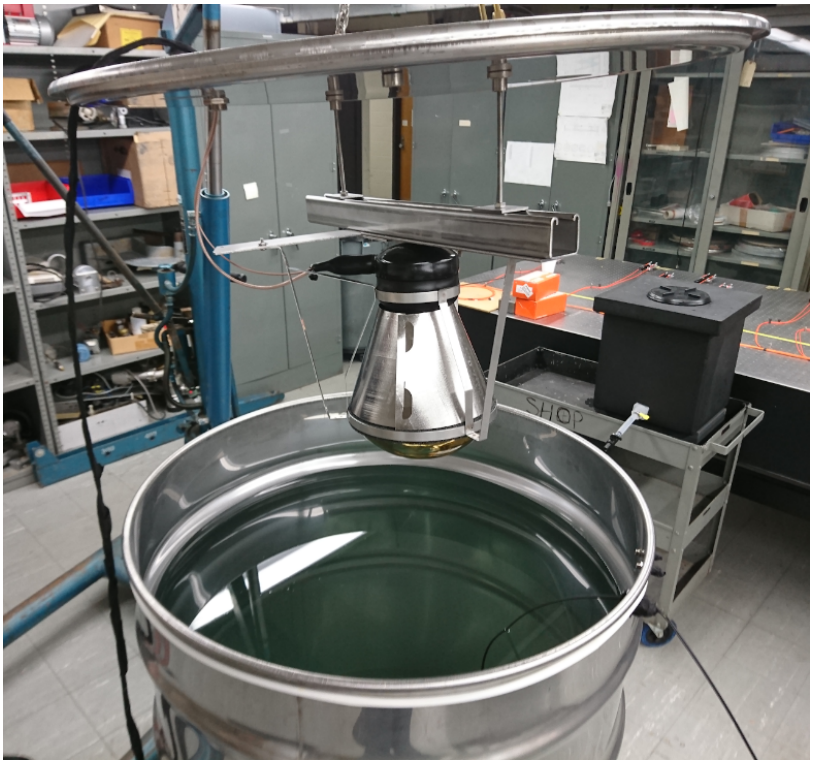

(b) OD Test Stand PMT lowered into barrel.

Figure 3.1: (3.1a): Schematic of OD test stand setup. (3.1b): Photo of OD Test Stand setup before PMT is lowered.

the the vacuum level barrier. A schematic of this process is shown in Fig. 3.2b. PMTs generally consist of a transparent bulb, usually some kind of fused silica, containing a vacuum with the internal surface coated with an alkali metal compound having a low work function, and a series of electron multipliers (dynodes) all connected to a readout circuit (see Fig. 3.2a).

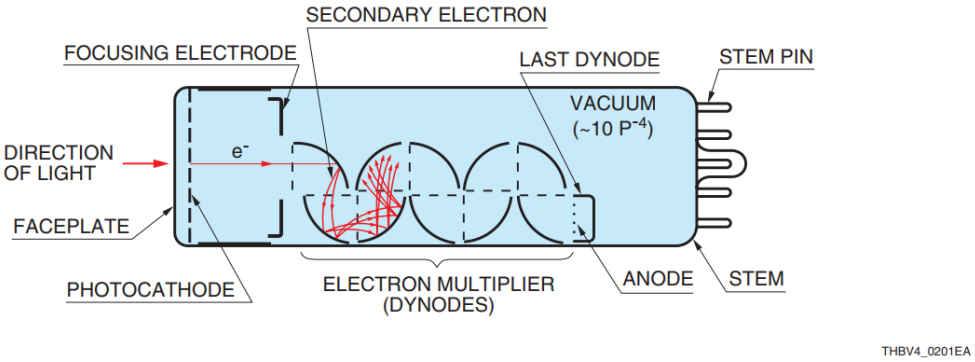

(a)

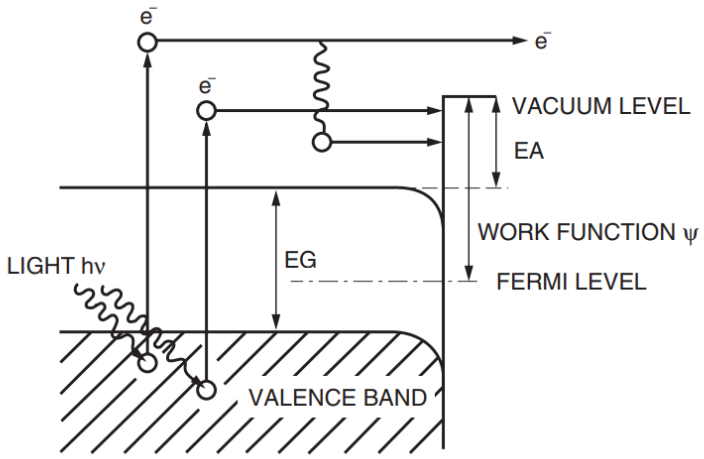

(b)

Figure 3.2: Basic structure of PMT (3.2a) and mechanism of light conversion to photo-electrons (3.2b) [79].

The liberated electron, henceforth called the photo-electron, is driven by a strong electric field from the photo-cathode, through a collimator, onto a series of electron multipliers (dynodes). The impact of the primary photo-electron on each dynode induces the emission of secondary electrons, which produce further electrons with each

impacting the next dynode and so on. Depending on the bias voltage applied between the photo-cathode and anode, these multipliers produce a current amplification of 10 - 10^8. Since the number of secondary electrons produced is highly dependent on the kinetic energy of the primary electron, the largest current amplification is achieved at the first dynode where the primary photo-electron has spent the most time accelerating under the influence of the bias voltage.

In the following sections a series of PMT characterization measurements are reported:

- SPE response at various bias voltages, producing a gain curve
- After-pulsing rate at 10^7 gain
- Dark Rate at 10^7 gain

3.2 SPE & Gain Curve

The electrical pulse output by a PMT has an area which is proportional to number of photo-electrons emitted from the PMT photo-cathode, with the charge amplification (gain) as the constant of proportionality. Thus the PMT's SPE response is critical to its performance as this allows the assessment of gain and working backwards, the quantity of incident photons. In an ideal world, the SPE response would be a single spike; in reality however there is broadening due to variations in quantum efficiency across the photo-cathode, non-uniformity in the electric field set up between the photo-cathode and anodes, impurities in the photo-cathode and dynode materials, and electronic noise. The shape of the SPE charge distribution, particularly the peak location and the width, provide an assessment of these effects and eventually, detector resolution.

SPE response is measured by injecting photons produced by an LED of wave-

length within the sensitivity range of the PMT in question[1]. At low intensities, the distribution of the number of photons emitted by the LED and incident on the PMT photo-cathodes tends towards a Poisson distribution. Setting the LED intensity such that only 10% of LED emissions result in a response from each PMT results in the vast majority of responses above the noise pedestal (95%) being single photons. Since the LED emission should have little time variation relative to the trigger signal, the LED pulses should occur within a small fixed window of time. One integrates over a fixed window of each acquired waveform defined using the peak and full width at half maximum (FWHM) of a distribution of pulse times produced by LED triggered data. These integrals yield the aforementioned charge distribution for the pulses captured, and since the intensity setting gives 10% probability of an LED pulse incident on the PMT, many of the integrals in this window occur on baseline and electrical noise fluctuations in the PMT base circuitry and acquisition equipment. This is the pedestal and gives an estimate of the ability to separate PMT signal from random electronic fluctuations in baseline noise. This gives a very clean measurement of the SPE response alone with minimal inclusion of higher photon multiplicities.

The SPE charge distribution displayed in Fig. 3.3b is generated using this procedure. The charge distribution is fit to the convolution, $F(q)$, of a Gaussian and a Poisson distribution (see Eq. 3.1). The Poisson component represents the distribution of the number of photons emitted by the LED, n, given an emission rate of λ photons per pulse. Both the mean and the variance of the Gaussian have a constant pedestal contribution (Q_0 & σ_0^2 respectively) and a term proportional to the SPE peak and resolution (Q_1 & σ_1^2 respectively). The constant of proportionality is n. This fit function is

$$F(q) \;=\; \sum_{n=0}^{\infty} Gauss\left(q; Q_0 + nQ_1, \sqrt{\sigma_0^2 + n\sigma_1^2}\right) \times \; Poiss(n;\lambda). \tag{3.1}$$

[1]In the most optimum scenario, one would make this measurement using many LEDs of varying wavelength.

The gain (charge amplification) is calculated as Q_1/e. Where e is the electron charge. Finally one fits the plots of gain vs Voltage to the function:

$$G(V) = 10^7 \cdot \left(\frac{V}{V_{1E7}}\right)^{\gamma}, \tag{3.2}$$

where $G(V)$ is the gain at voltage V, γ is a free parameter, and V_{1E7} is voltage corresponding to 1E7 gain. The resulting fit parameters are used to determine the

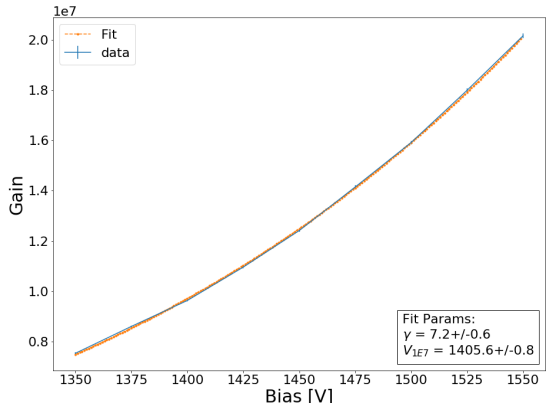

(a) Gain curve produced from SPE acquisitions at bias voltages from 1350-1550 V.

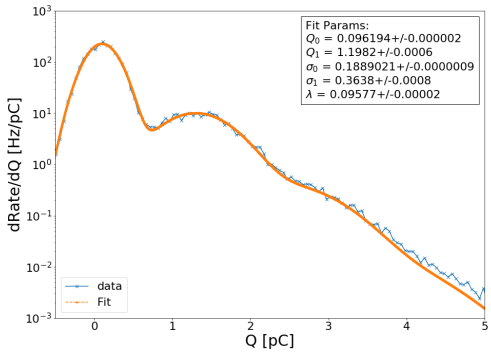

(b) Charge spectrum produced by single SPE acquisition run. Spectrum is fit to Eqn. 3.1.

Figure 3.3: Gain curve produced from SPE responses at various voltages. Curve is fit to Eqn. 3.2.

voltages required to gain match PMTs, in addition to determining the bias voltage required if one wishes to operate at a different gain. The curves generated with the empty barrel and the full barrel are consistent, as one would expect.

3.3 Afterpulsing

After-pulses are produced when photo-electrons ionize the residual gasses in the PMT. These residual ions drift back to the photo-cathode resulting in a secondary delayed pulse. Thus, the rate of these after-pulses acts as a monitor of PMT health. The most common gasses causing this are hydrogen, helium, oxygen, nitrogen, methane, with less frequent occurrences of argon and xenon. Hydrogen and helium are expected

to be the most abundant gasses and hence the cause of most after-pulses. One can determine the responsible gas for a given after-pulse based on the delay from the prompt pulse. This delay is precisely the drift time of ions to the photo-cathode, and thus is correlated with the bias voltage (V_0) across the PMT. Modelling the electrical potential between the first dynode and the photo-cathode as quadratic, one can determine the expected delay (t_I) for ion I from Eq. 3.3:

$$t_I = \sqrt{\frac{m_I}{2q_I V_0}} \times L \int_{s_0}^{L} \frac{1}{(L-s_0)^2 - (L-s)^2} ds = \frac{4}{\pi} \sqrt{\frac{2m_I}{q_I V_0}} \times L, \tag{3.3}$$

where L is the distance from the photo-cathode to the first dynode, m_I is the ion mass, q_I is the charge of the ion, and s_0 is the position of the origin (the first dynode). Due to the large size of the R5912 PMTs, these gases may not be ionized close to the first dynode (s_0), thus one expects a fair amount of spread in after-pulse delays around the calculated values of t. Estimations of afterpulsing times for a selection of common ions is given in Table 3.1. However, in this study, we are less concerned

Ion	Timing (μs)
H+	1.5
H_2+	2.1
He+	3
O+	7.5
CH_4+	7.5
Ne+	8
N_2+	9.5
Ar+	10.5
Xe+	18.5

Table 3.1: Estimated afterpulsing times from Eq. 3.3 for a selection of common ions given $V_0 = 1.2$ V.

with the specific ion which caused the after-pulse than the overall after-pulsing rate per photon incident on the photocathode. This overall rate is calculated using a large LED SPE dataset with an extended acquisition window, recording PMT pulses up to 20 μs after the SPE. The ratio of delayed pulses occurring over 500 ns after the SPE

to LED SPEs gives this afterpulsing rate.

The measured distribution in the ODTS is shown in Fig. 3.4. With the ratio of

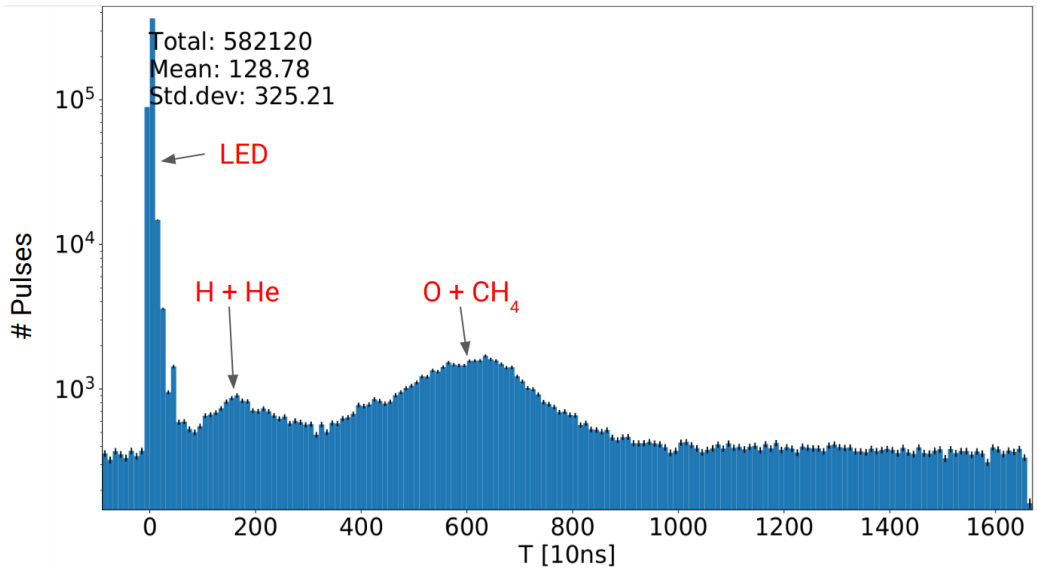

Figure 3.4: Pulse time relative to the prompt LED pulse (T = 0), with prominent afterpulse peaks visible at approximately 1.8 μs and approximately 6.2 μs after the LED pulse.

delayed pulses to LED SPEs yielding an afterpulsing rate of 2.8%.

3.4 Dark Rate

When a bias voltage is applied across a PMT, there exists an internal background independent of photons incident on the photo-cathode; hence it is termed dark rate. It is important to monitor and understand Dark Rate as it can contribute to spurious signals, changes in dark rate alert one to significant deviation/degradation in the environment or PMT response. This background may have multiple sources:

- Thermionic emission from photo-cathode and Dynodes
- Leakage current between electrodes
- Field emission

- Cosmic Rays incident on PMT glass

The PMTs used in this study are consistently operated in the $800V - 2000V$ range. This range is low enough that field emission is subdominant, and high enough that leakage current is also negligible. Since the cosmic ray flux at sea level is $O(1\ Hz\ m^{-2})$ it is clear that this component is meager in comparison to the $O(100\ Hz) - O(1000\ Hz)$ of dark rate observed in many large area PMTs.

The remaining source of thermionic emission is dominant in the operating regime of this study. This process involves thermal fluctuations exciting an electron to the vacuum band. As a result, this process is temperature dependent. In addition, there is also a dependence on bias voltage as this impacts the gap between the conduction band and the vacuum level.

These emissions result in mostly SPE-like pulses distributed uniformly in time, lowering the energy resolution of the system and lowering sensitivity of the OD.

Whilst multiple photo-electron pulses can be produced by this process, in the scenario where these are significant/dominant, the dark-rate need be excessively large, such that the PMT would be blind to all but the very largest of external pulses, introducing an untenable uncertainty in both resolution and sensitivity.

The PMT was set to the voltage required for 10^7 gain, as determined by the gain curve measurement and left in the sealed ODTS for approximately 14 hrs. The trigger threshold on the DAQ was set at 0.1×SPE height, approximately 0.6mV. The differential rate of triggering pulses, as a function of pulse area, is calculated by integrating the 8 sample regions around the trigger points to obtain pulse area, histogramming these areas, and normalizing the histogram with the livetime. Due to initial exposure to light, the PMT photocathode has an elevated dark rate. Once placed in the dark tank, one must allow this elevated rate to reduce over time. This is expected to occur with a few hours. One records PMT dark pulses during this entire period to observe this decay to the base rate.

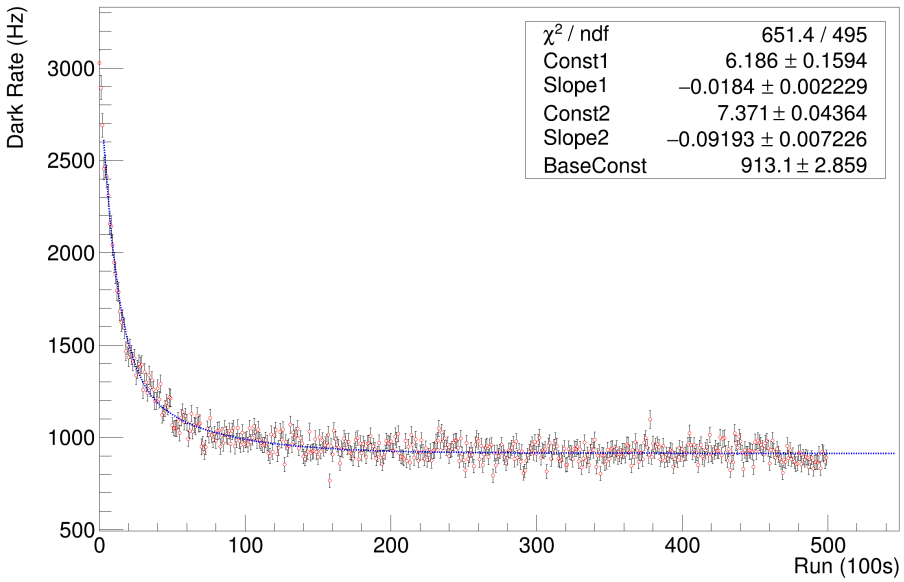

(a)

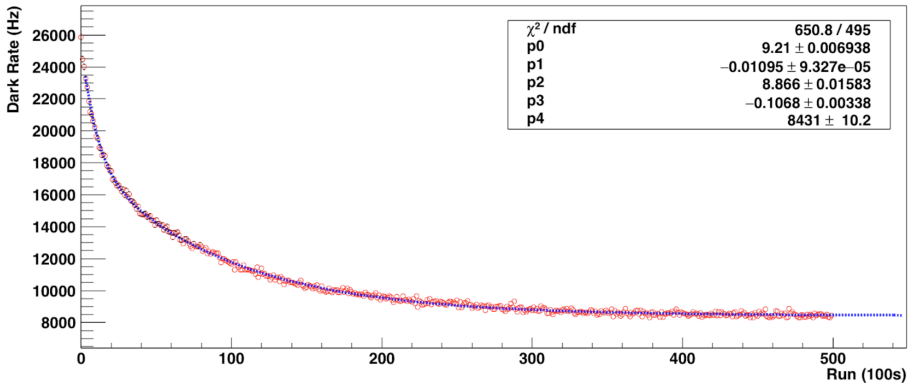

(b)

Figure 3.5: Dark rate over time in filled Test stand(**a**) vs Empty Test Stand(**b**). Here the base dark rate after the cooldown period is found to be 9 times higher in the filled test stand compared to the empty test stand.

Fig. 3.5a shows this cooldown curve for the PMT in the empty barrel. The base rate here is consist with expectations from the manufacturer and is sufficiently low that one expects no significant impact on their operation in the outer detector.

Upon completing the measurement in the empty barrel, one proceeds to conduct the same measurement with the full barrel. This is where one encounters a discrepancy. It can be seen in Fig. 3.5b that the base rate achieved is elevated compared to the empty barrel. In addition to this, it is clear that the system takes far longer to

achieve the base rate state than in dry. Repeated measurements confirm this effect and show consistently elevated rate by a factor of 9. It is also observed that when the empty tank measurement is conducted, the base rate returns to its previously measured value. From this it is inferred that the effect is not due to a permanent change in the PMTs behaviour. This effect when PMTs are submerged in water has been observed in several other experiments though no clear answer has been found [80]. Thus a series of tests to investigate this effect are conducted.

The first test involves partially filling the barrel to determine if the change is due to the full submersion of the PMT. The suspicion here is that the sealing on the PMT base is not entirely water tight and may be causing a temporary interruption in the circuitry of the PMT base. The results of this are shown in Fig. 3.6. Here it can be

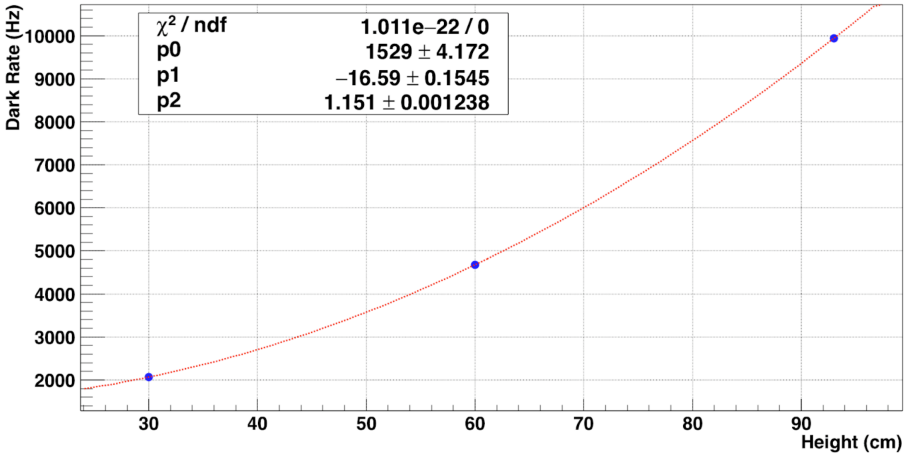

Figure 3.6: Dark rate against water level in OD Test stand.

seen that the elevated rate scales with the quantity of water in the barrel. What is not evident from this is whether the relevant quantity is the volume or the distance of the water surface to the PMT as both are changed in this measurement. A further measurement to determine this is conducted and detailed below.

3.4.0.1 Temperature Dependence

One factor which it is necessary to test is temperature dependence. Since thermionic emission is the dominant process producing dark rate in the range of operating voltages used for this study. Measuring the change in dark rate by varying the water temperature tests this factor rather thoroughly. The test stand is fit with an electrically insulated heating element in addition to 4 resistance thermometers (RTDs) at various locations on the tank. A schematic of this setup is shown in Fig. 3.7.

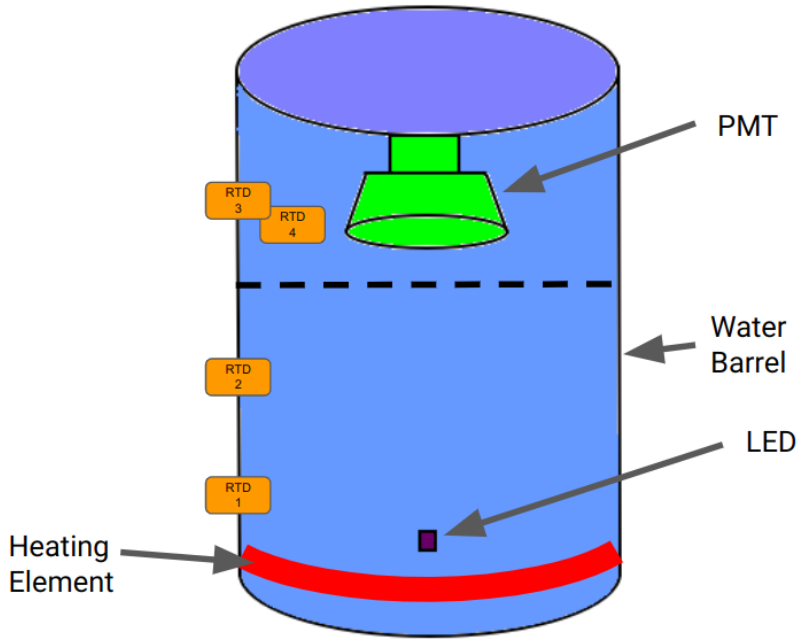

Figure 3.7: Schematic of test stand setup with heating element and location of monitoring RTDs.

Once set up with the tank in the full state, the PMT is allowed to reach its base dark rate over 14 hrs. The heating element then raises the water temperature at which point a measurement of dark rate is acquired. Measurements are taken over a range of temperatures from 21 C to 30 C. The results of these are shown in Fig. 3.8.

From this it is observed that the temperature effect does not account for the elevated rate. Whilst the dark rate is significantly correlated with the temperature it

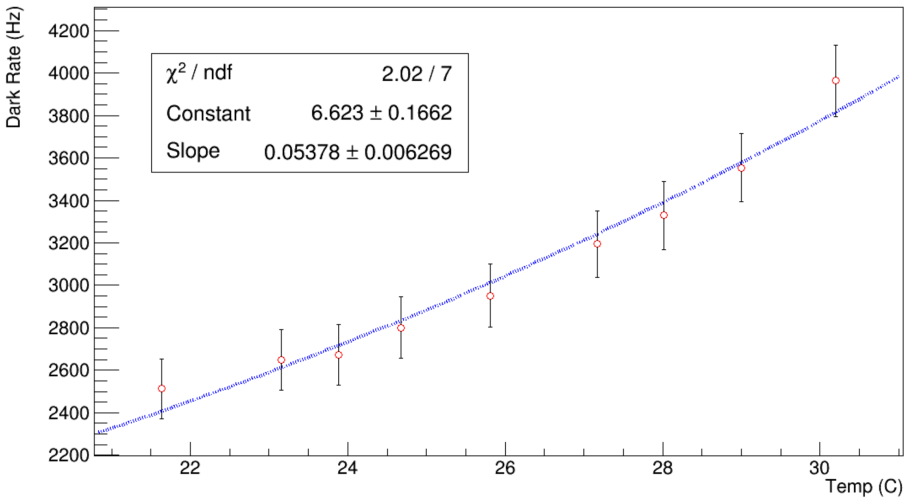

Figure 3.8: Dark rate as function of temperature when submerged in water.

falls far short of accounting for the observed increase. A change of 9 C (significantly higher than the fluctuations one would expect during normal operation) results in a factor of 2 increase in dark rate, which is well below the observed effect.

3.4.1 Shrouded PMT & Water Depth/Distance

To determine if the excess rate is truly dark rate in the sense described above, one shrouds the PMT to block light that may be emanating from the water. This setup is shown in Fig. 3.9. The striking results of this measurement are shown in Fig. 3.10. The shrouded PMT in the full barrel recovers almost entirely the empty tank dark rate. The clear conclusion here is that the increased rate is due to light production from the water. At this point it is necessary to investigate whether this increase is the result of a surface effect of the water. A small cuboid container of DI water, with surface area 20 cm×30 cm, is placed in the tank at varying distances to the PMT and the cool down curve is measured. In addition two water depths are utilized. A schematic of this setup is shown in Fig. 3.11. As can be seen in the results summarized in Table 3.2, the vastly smaller volume of water at a distance of 10.78 cm from the PMT recovers almost entirely the elevated dark rate of the full tank. Increasing the

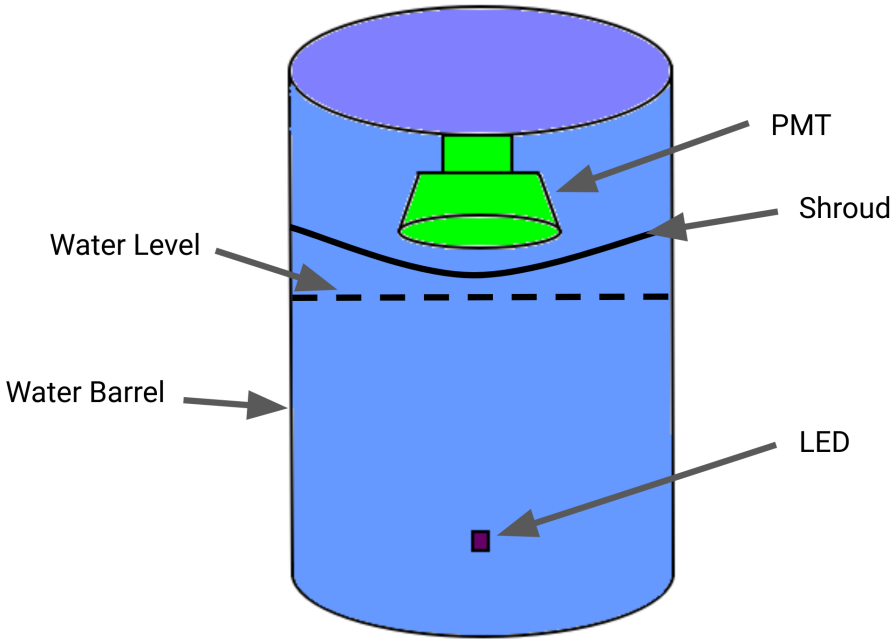

Figure 3.9: Schematic of ODTS with shrouded PMT.

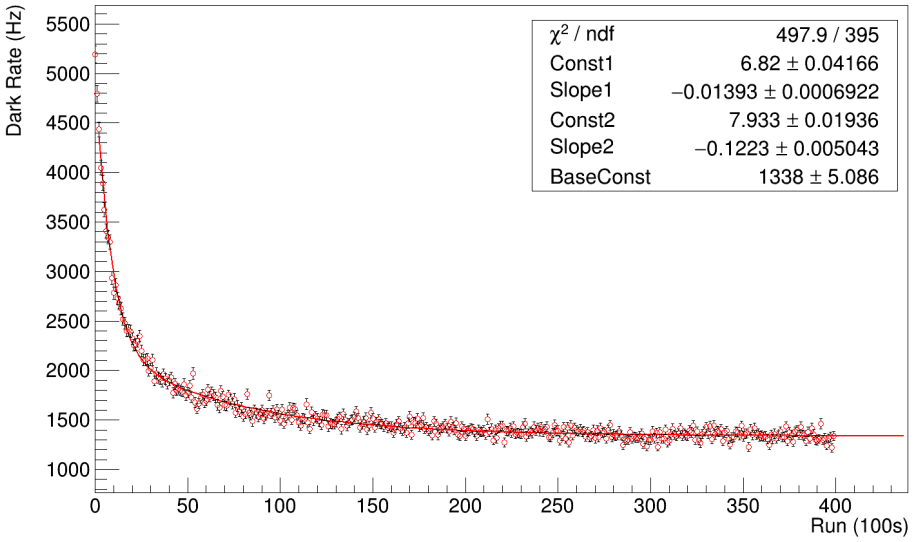

Figure 3.10: Dark rate with PMT Occluded.

distance from the PMT, the dark rate reduces significantly. From this it is inferred that the changes observed when varying the fullness of the tank were primarily due to the distance from the surface, since the effect of the full tank of water was replicated with a small volume of water close to the PMT.

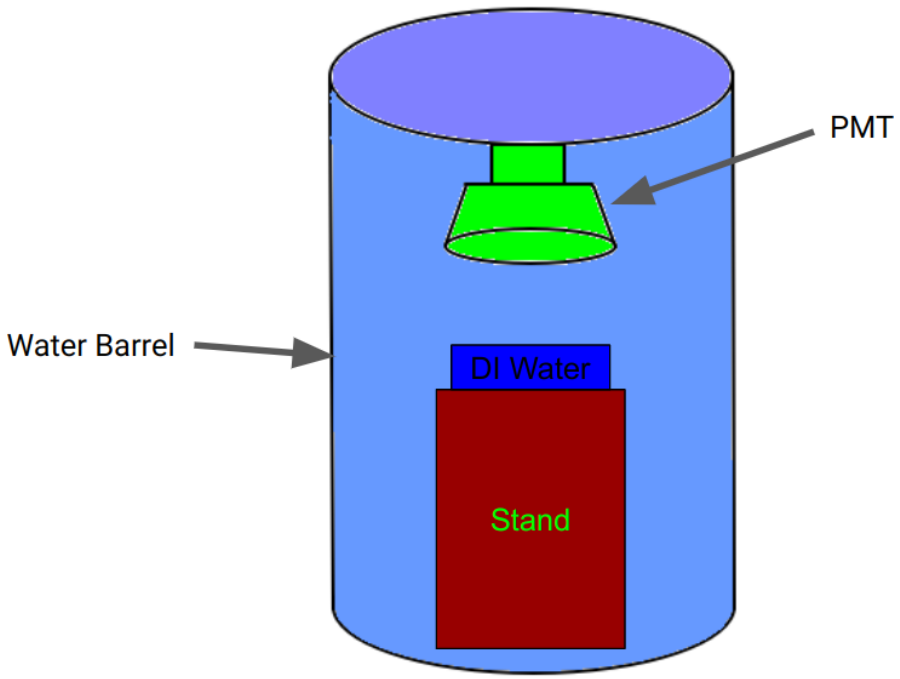

Figure 3.11: Schematic of ODTS setup with small container of DI water to investigate the effect of distance between water surface and the PMT.

Water Depth	Distance to PMT	Plateau Dark Rate (Hz)
0	Empty	913.1 ± 2.9
1 cm	10.78 cm	4638 ± 32
11.5 cm	10.78 cm	8431 ± 10
11.5 cm	27.78 cm	3880 ± 5
11.5 cm	42.78 cm	3114 ± 4

Table 3.2: Table of dark rate measurements in Empty tank compared to a small container of water several distances from the PMT.

Given the much smaller volume of water reproducing the full effect, it appears that the observed photons are produced within a surface layer of at most 11.5 cm thickness. Since the absorption length of water within the 250-700 nm range does not fall below $\mathcal{O}(1\ m)$ [81], if light were being produced in the water bulk but screened such that only this small depth was observed, an overwhelmingly high rate of photons below 200 nm and/or above 800 nm would be required to overcome the sub 0.1% PMT quantum efficiency shown in Fig. 2.7b and reproduce this effect. This is unlikely.

Considering sources of radiation which may account for this, one can discount all

sources which would scale with the volume of water present, this includes radioactive contamination in the steel container, in addition to contamination of the water bulk. One is left to consider radioactive contamination in the air from sources such as ambient radon. However, given the much lower rates observed in the much more sensitive target of NaI used in the measurements to be detailed in Chapter V this also seems very unlikely.

3.5 Concluding Remarks

Basic procedure for OD PMT characterization have been tested, proving viable for monitoring the OD health and stability. An anomalously high dark rate has been measured in PMTs in the presence of water. This effect has been observed in other PMT deployments though has remained unexplained [80]. Here a series of tests are conducted which show that this additional signal is the result of real photons (shrouded measurements). It is shown that only the first few centimeters of water closest to the PMT contribute to this effect. Involvement of temperature dependence in the PMT is discounted as primary causes. Radioactive contamination also appears an unlikely candidate, though a more detailed exploration of this avenue is required to make conclusive claims.

CHAPTER IV

Outer Detector Commissioning

After construction and installation a variety of measurements are conducted to commission the Outer Detector (OD). These include PMT commissioning activities in which the procedures developed in Chapter III are implemented for the LZ, in addition to a timing correction aligning the signals from each PMT such that only time variations due to geometry and the emission properties of the scintillator are observed. Beyond this, an independent trigger of the OD is developed to boost statistics of large area pulses and aid in neutron studies. These activities are detailed in the remainder of this chapter.

4.1 PMT Commissioning

Once installed, the various PMT properties described in Chapter III are remeasured, both for consistency and to establish a baseline for monitoring the the installed environment. In what follows, the results of these efforts are presented. All PMTs in the LZ detector are given an ID number with the OD PMTs having ID numbers in the range 800-920.

4.1.1 Single Photo-Electron (SPE) Response

One integrates over a fixed 120 ns window (defined per PMT using the peak of the pulse time distribution shown in Fig. 4.1). The resulting SPE values are shown

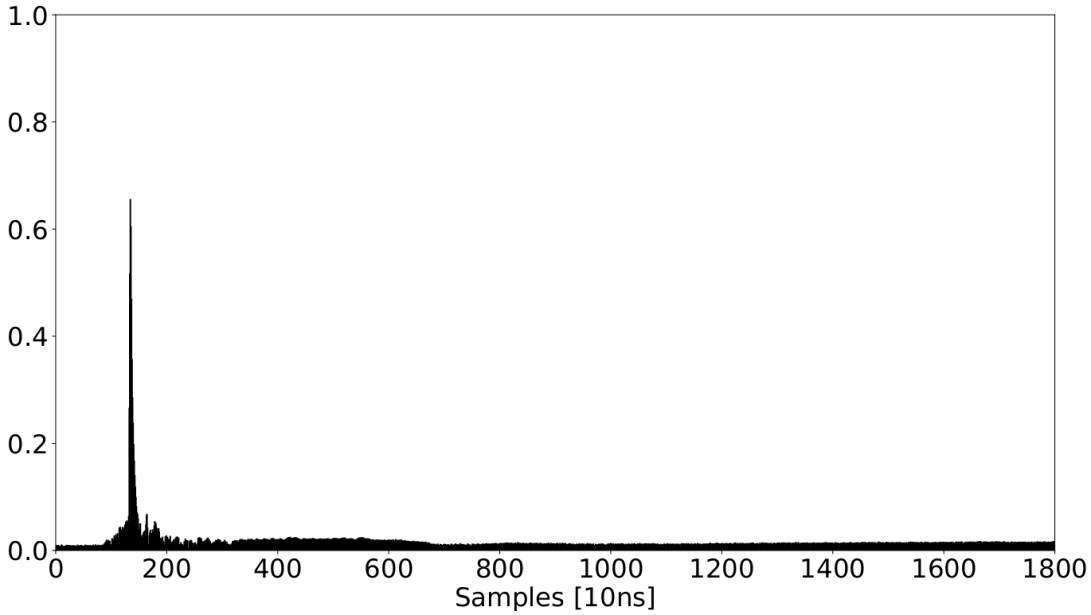

Figure 4.1: Distribution of pulse times used to determine the SPE integration window for one of the 120 installed PMTs.

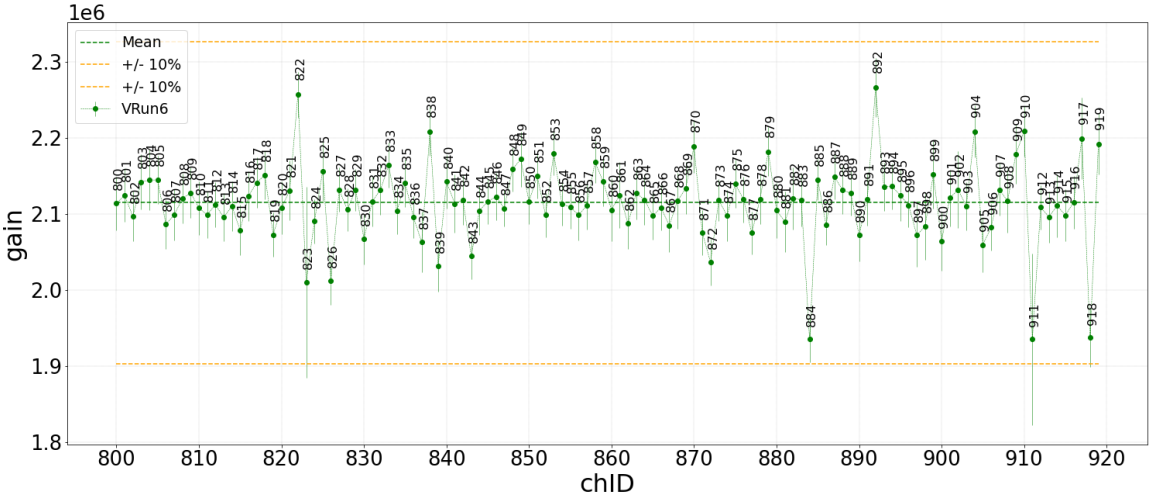

Figure 4.2: SPE values for the 120 installed PMTs.

in Fig. 4.2, where it is evident that all PMTs are matched within 10 % of each other.

By matching the PMT gains like this, thresholds can be set more uniformly, thus reducing complexity of further studies.

4.1.2 Dark Rate

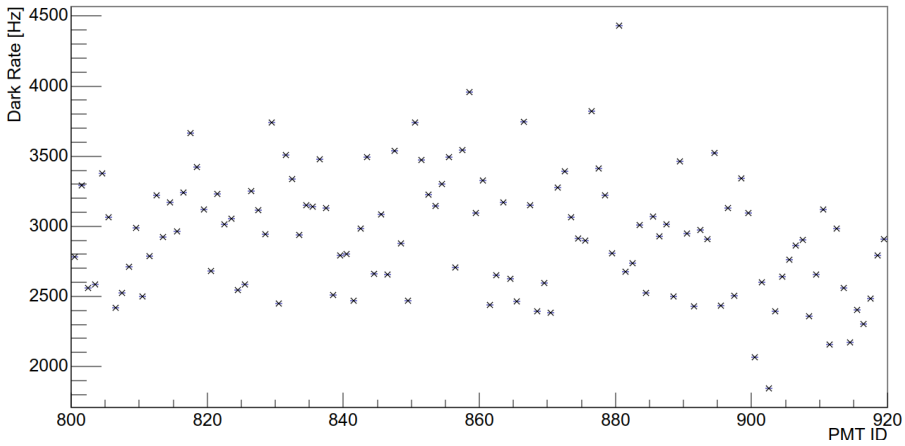

Figure 4.3: Dark Rates of the installed PMTs. Overall dark-rate given by integral above Valley.

Measurement of the dark rate is rather simple, only requiring recording of PMT signal output (in a darkened state with no external light) with a random trigger. The resulting distribution of recorded pulse areas (rate normalized), closely mirrors the SPE distribution. The dark rate is calculated as the integral of the pulse area spectrum above the area corresponding to the valley separating the SPE peak and the noise pedestal.

In order to limit impacts on live-time and energy resolution, the dark rate of each PMT should to be less than 10 kHz. All installed PMTs meet this requirement.

4.1.3 After-Pulsing

In order to measure after-pulse, one again uses the OCS system to inject SPEs, recording pulses 20 μs after the injection. The after-pulse rate is defined as the number of after-pulses per SPE incident on the PMT, as detailed in Chapter III. Since unconcerning after-pulse rates should be low, one needs a large number of

injected pulses to obtain suitable statistics. In order to minimize the live-time impact of after-pulses to LZ and as a flag for degrading or damaged PMTs, the overall after-pulse rate per PMT is required to be under 10%. Subtracting the flat contribution from dark pulse rate from the resulting pulse time distribution, the after-pulse rate is calculated as the ratio of the integral of the prompt peak to the integral above 500 ns. The resulting after-pulse rates are shown in Fig. 4.4, with all installed PMTs

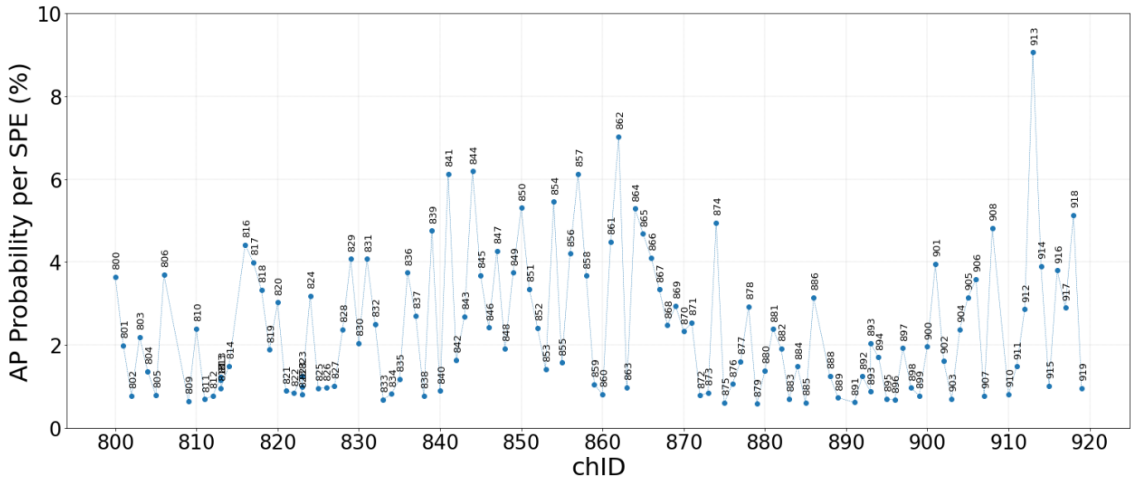

Figure 4.4: After-pulse rate calculated for each PMT.

meeting the 10% requirement.

4.2 OD Intradetector Timing (PMT Transit Time Calibration)

It is necessary to calibrate the timing of PMT measurements to ensure that the time distribution of signals at the PMT photo-cathode are preserved as they travel through the cables to the amplifiers and eventually the DAQ. This ensures that signals across many PMTs can be combined without introducing unnecessary distortions. This calibration is achieved using SPE data from all LEDs on the middle row of the OD OCS system. For each LED one only includes data from the adjacent 4 closest columns of PMTs since outside of these the signal is reduced, and illumination

from the most direct path is far less likely thus reflections reduce the measurement precision. The variation in time from light emission to electrical signal in DAQ has multiple components:

1. Geometric: Time of Flight (TOF) in GdLS, Acrylic Tanks, and Water.
2. Transit time of photo-electrons in the PMT varies with square root of bias voltage
3. Transit through PMT signal cables of variable length due to cable extensions
4. Shaping filters on the amplifier boards

The TOF component one would like to preserve in the output signal, so whilst it will not be corrected for, it must be considered due to how difficult it is to disentangle from the transit time in the PMT. The component from the PMT transit time is disentangled from the geometric effects in the detector by estimating and subtracting the TOF from each combination of LED and PMT. This process is a geometric exercise in which the optical path from a fibre to a point on the OCV Tyvek reflector and back to a PMT is calculated by hand, using the known dimensions of the detector as built, and combined with the refractive indexes of the intervening water and GdLS to obtain the required TOF. This approach is simple, but given, the prompt PMT signal is used and only nearby PMT ladders to each fibre are used, an (unlikely) error in the calculated path length of $\mathcal{O}(1\text{ m})$ is required to induce a TOF error of 1 ns. Thus a sufficiently precise answer is obtained. The component from the amplifier boards and shaping filters is calibrated by injecting a signal at the input and recording the variation in signal time of flight across input channels.

Due to a very minor impedance mismatch at the amplifier boards, one can use the reflection to determine the component of the correction coming from the cables. To begin, templates of the SPE are built using LED data, from this we can extract

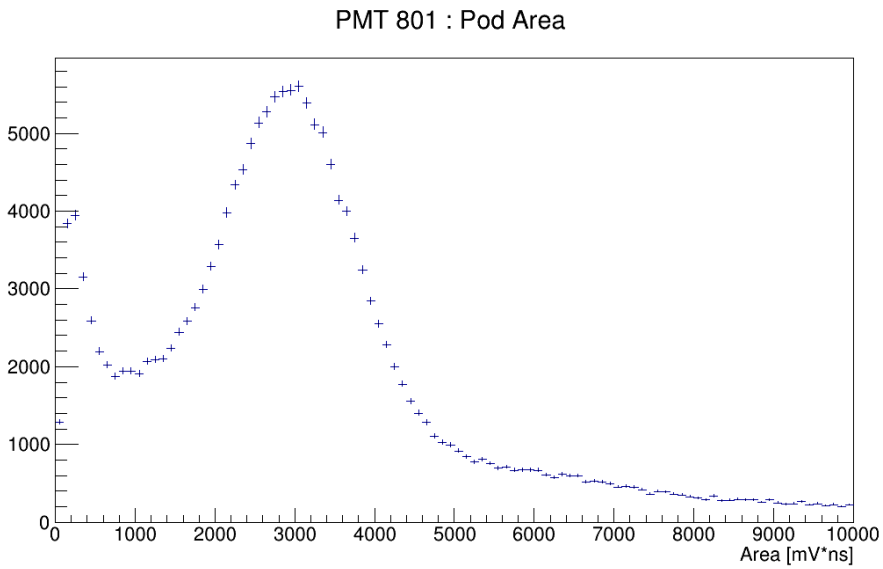

Figure 4.5: Histogram of pulse (POD) areas for PMT 800. Pulses contributing to the SPE template are selected from within the FWHM of the peak at approximately 3000 mV·ns.

directly the time between the main pulse and the reflection pulse. The templates are generated by averaging over SPE waveforms selected based on area within the FWHM of the SPE peak in a histogram of pulse areas. An example of these is histogram is shown in Fig. 4.5. When conducting the averaging of the wave-forms, an offset is applied such that the peak of each pulse lies on the Time = 0 line. An example of the resulting template is shown in Fig. 4.6a. A template is generated for each PMT.

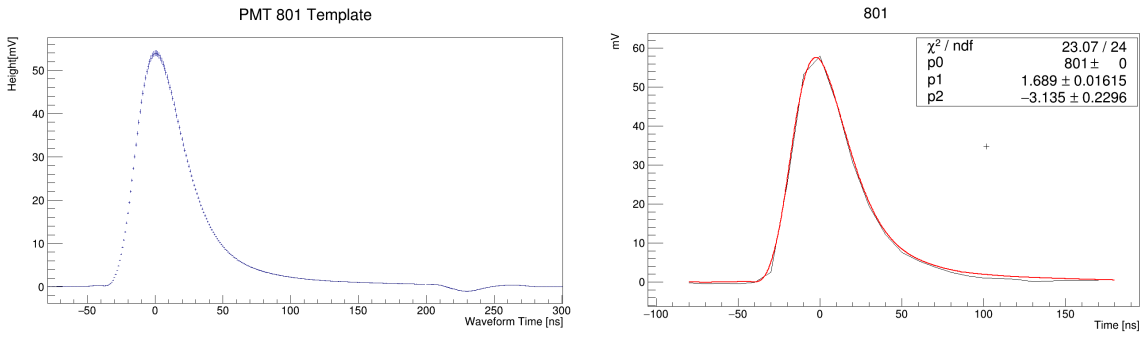

(a) (b)

Figure 4.6: Examples of the resulting SPE template shape for PMT 801 (4.6a) and a fit of this to a pulse observed in the same PMT (4.6b).

The reflection times shown in Fig. 4.7 are extracted from the templates as half the time difference between the main pulse peak and the peak of the small negative dip (approximately 230 ns in Fig.4.6a). Halving this difference accounts for the travel time from the amplifier board to the PMT base, and back to the amplifier and DAQ. In principle a small component of the reflected pulse is also reflected back to the PMT, though the attenuation is so great that in practice further reflections are lost under electronic noise. Once the templates are acquired, they are used to fit to a further set of LED SPE data acquisitions from which the photon time is determined to be 10% of the rising edge of the pulse relative to the LED trigger. These are plotted in Fig. 4.8. The rising edge of this distribution, after subtracting the TOF of photons through the fibres to the PMT, gives a series of time delays for LED-PMT pairs. Taking an average of this value for each PMT which was exposed to the LED light, one now has a series of corrections for each PMT.

The choice of whether to use absolute or relative corrections is arbitrary since a further correction will be applied to align the sub-detectors to each other using the coincident back to back gamma signal from an ^{22}Na source. In this case relative corrections were selected, which simply means calculating the deviation from the mean of these values across all PMTs. The resulting corrections are shown in Fig. 4.9.

4.3 OD Energy Scale

The OD energy calibration was performed using ^{57}Co, ^{54}Mn, ^{228}Th, and ^{22}Na gamma sources in the CSD. In addition to these, the 2.2 MeV hydrogen neutron capture gamma and 8 MeV Gd neutron capture signal from the ^{252}Cf source was incorporated. Picking out the peaks from these sources the response of the OD can be parameterised. The resulting energy scale is displayed in Fig. 4.10, with the linear component of the scale yielding 230 phd/MeV. Even at low energy (below 300 keV) where significant losses would be expected due to the non-linear energy response of

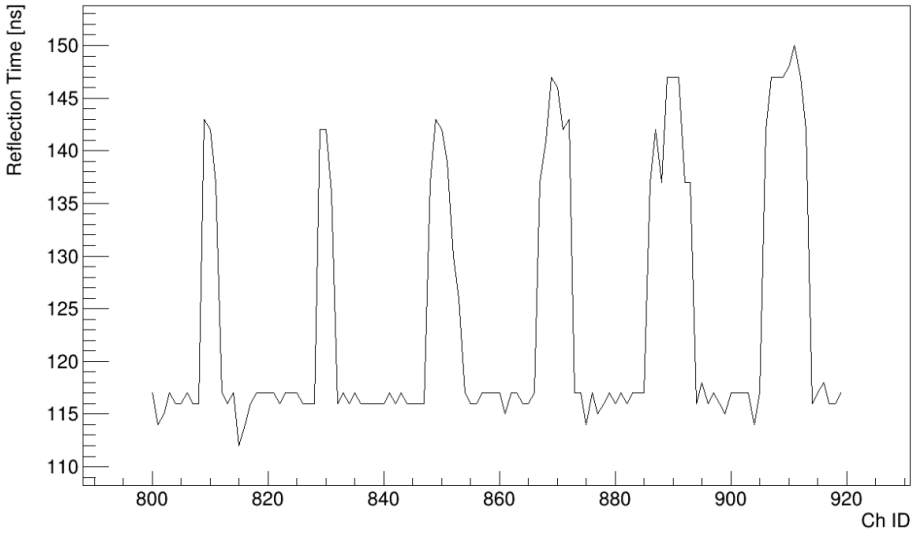

(a) Reflection Times calculated from SPHE Templates.

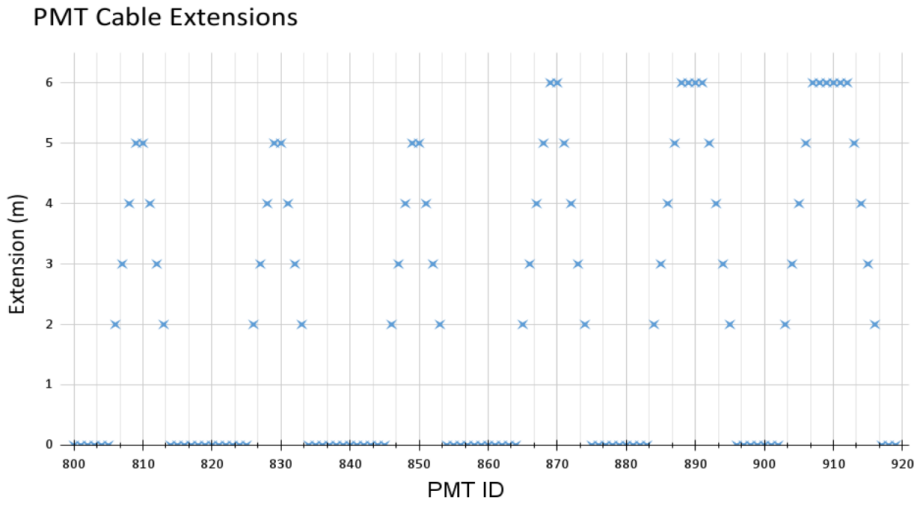

(b) PMT cable extensions.

Figure 4.7: Reflection Times calculated from SPHE Templates, along with cable extensions for all PMTs. Comparing these two distribution acts a cross-check that the approach taken is producing reasonable answers.

GdLS, 75 % of the deposited energy is still visible. The details of this study are contained in [82].

4.4 OD Neutron Trigger

LZ employed two physics trigger modes during the first science run. The first and most important of these triggers on events occurring in the TPC, where the primary

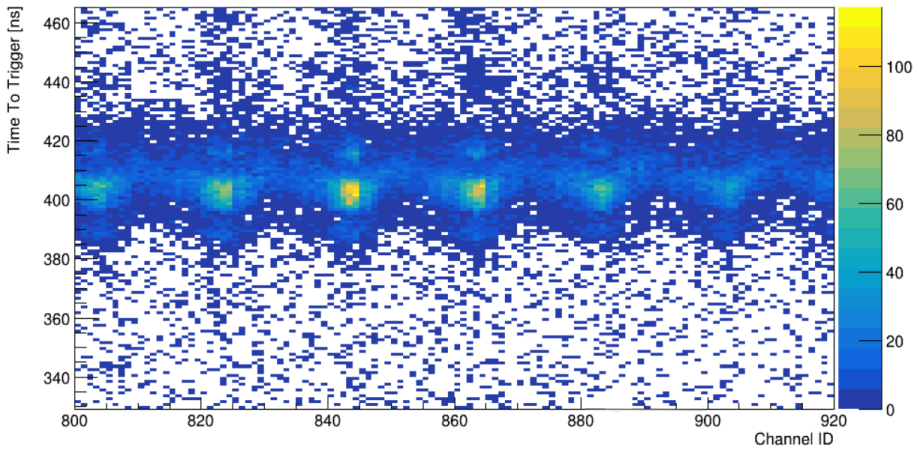

Figure 4.8: Histogramming the photon times determined from the template fitting procedure.

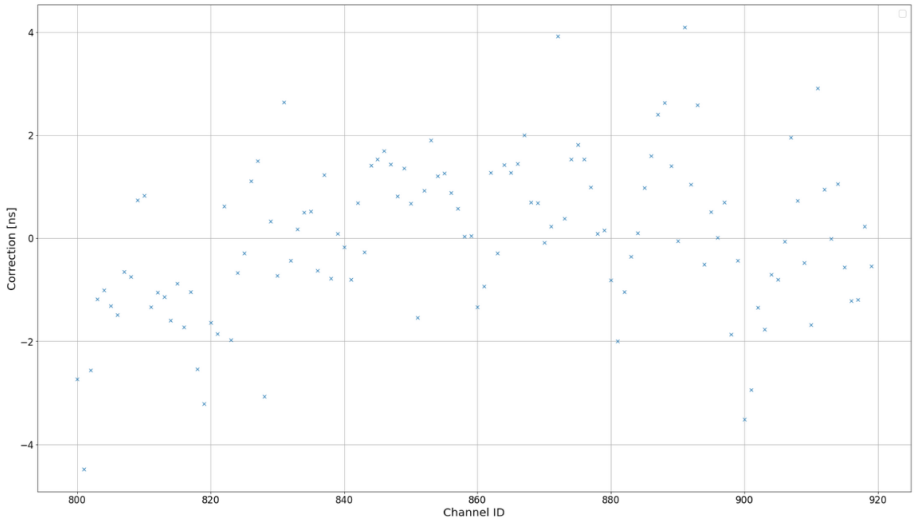

Figure 4.9: Final relative corrections for OD PMT system

search for the rare dark matter signal will occur. In this mode one reads out from both the TPC and the OD, using the latter to veto nuclear recoils in the former. The second mode triggers on OD events only, and only the OD signal is recorded. This trigger is designed to study more closely the ambient rate of the full spectrum of neutrons in the LZ detector. In order to do this one tunes the trigger for the 2.2 MeV hydrogen capture. This capture signal of a mono-energetic gamma is very clear, and being lower than the Gd capture, ensures that those too would be triggered on.

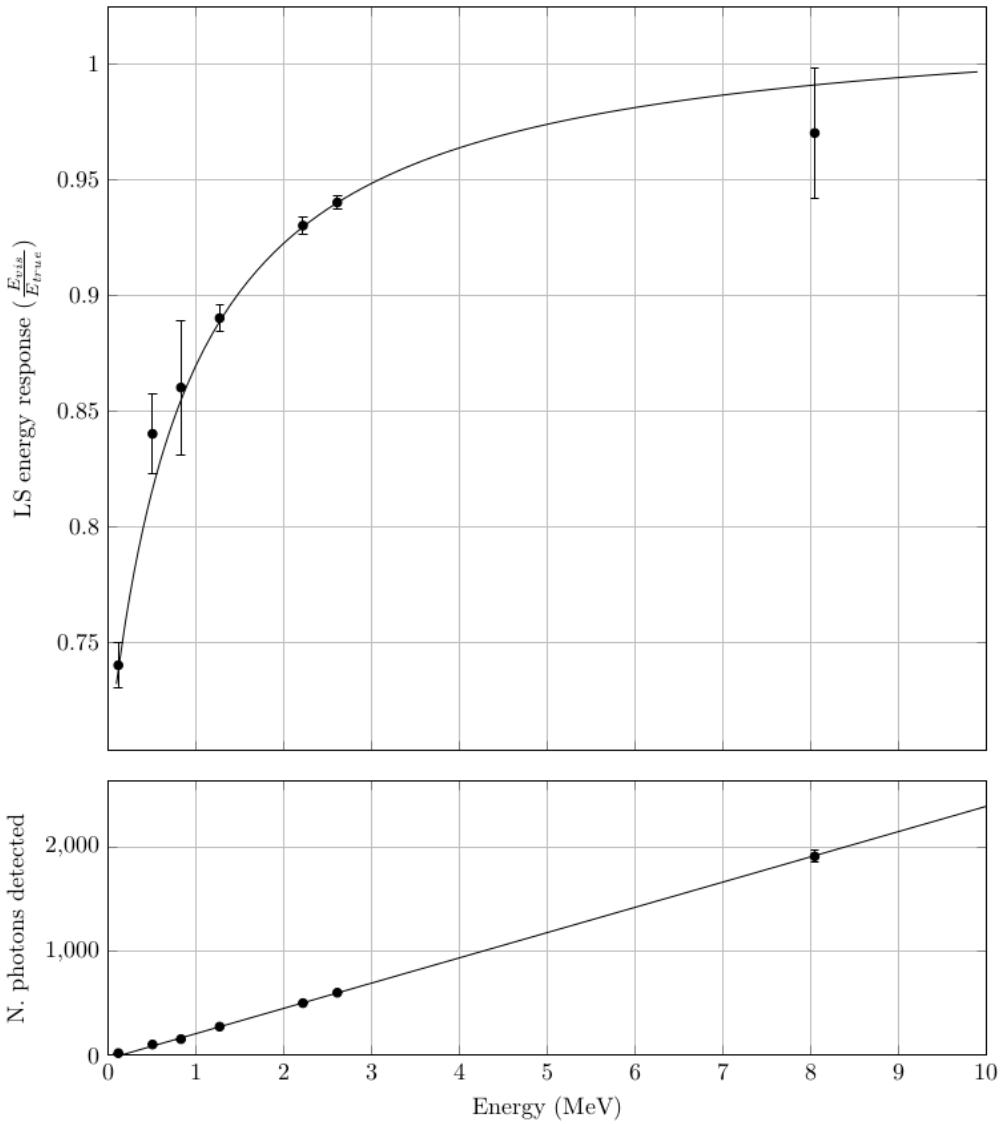

Figure 4.10: OD Energy Scale and the relation between the observed number of photons and the energy deposited. Figure from [69]

4.4.1 Trigger Structure

All PMT signals in LZ are split along two paths. One of these paths goes through a convolutional filter, and it is based upon this filtered signal that trigger decisions are made. The filter itself is formed of two side lobes and a central valley, as shown in Fig. 4.11a. As can be seen in Fig. 4.11b, the two side lobes act as effective baseline subtraction. Once a signal is filtered, provided that the filtered signal is above a user

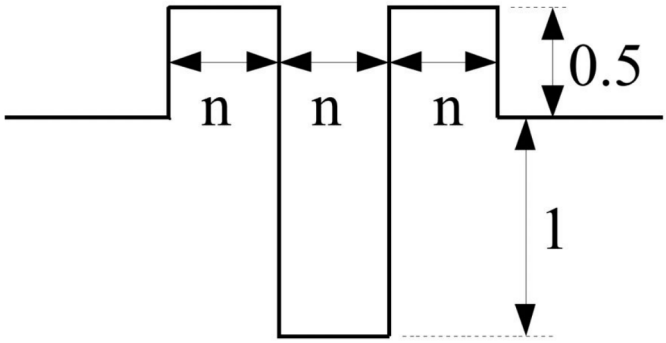

(a) Specification of LZ S1 filter which is convolved with waveforms.electing appropriate widths for the central and side lobes, results in zero crossing points in the output which correspond to rising and falling edges of pulses.

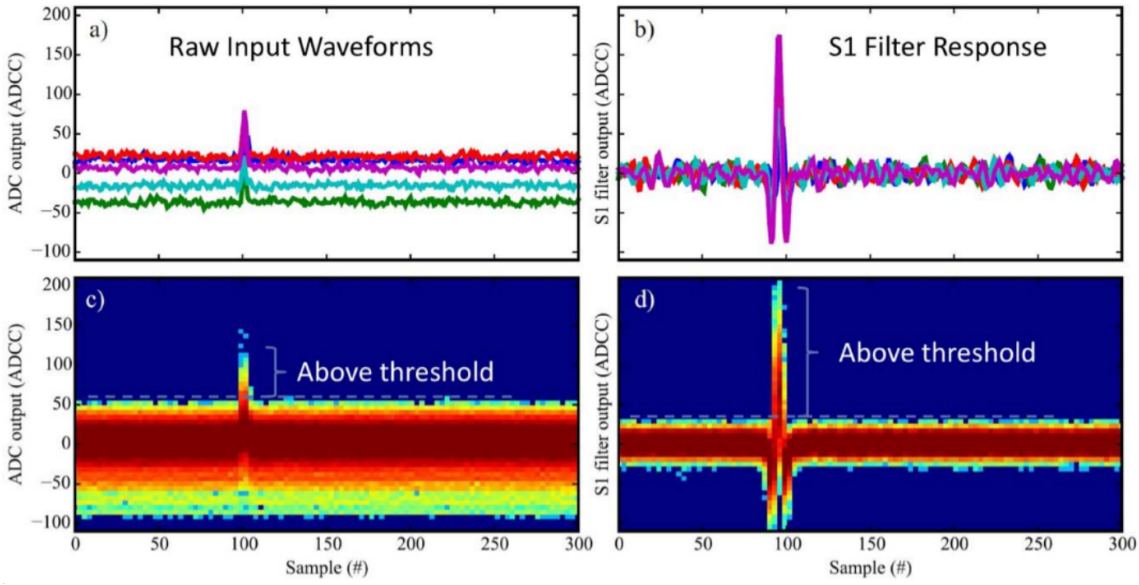

(b) Output of S1 Filter.

Figure 4.11

threshold, that signal is passed to the next stage of the trigger decision.

Once a collection PMT signals above threshold is obtained, one must determine if any section of these meet a given multiplicity and coincidence condition. Where the term multiplicity refers to the number of unique PMTs which observed a signal above threshold within a given time window.

Once the stream of data meets all of these conditions, it is recorded to disk.

4.4.2 Setting Filter Parameters

Since the S1 filter is applied to PMT signals on a channel by channel basis, the lobe widths and thresholds are initially based on single photon pulses. Since the filter response is proportional to the input in area, one may simply scale the threshold by the desired count of photons to accept.

In determining the one photon threshold, the filter is applied to a data set of SPE measurements, with a range of lobe sizes. The peak response for each pulse is obtained as a candidate threshold. These candidates are then used to populate a two dimensional histogram of threshold against lobe width, which we will denote $H(n,T)$, where n is the lobe width, and T is the candidate threshold. A conversion of $H(n,T)$ into efficiency, $E(n,T)$, as a function of n and T is achieved with the following calculation.

$$E(n,T) = \frac{\int_T^\infty H(n,T_p)\ dT_p}{\int_0^\infty H(n,T_q)\ dT_q} \tag{4.1}$$

To fully study the efficiencies involved here, one separates the data set into two components. The first is classed as the true photons, and is defined as all pulses with charge greater than $\frac{Q_{SPE}}{4}$. Where Q_{SPE} is the charge of the SPE peak. The remainder of the data is classed as noise, since data points in this region are deep inside the noise pedestal. Calculating efficiencies separately for "true photons", denoted $E_{SPE}(n,T)$; and for the noise rejection is defined below.

$$E_N(n,T) = 1 - E_F(n,T) \tag{4.2}$$

Where $E_F(n,T)$ is the false positive rate defined using Eqn. 4.1. They are then combined in Fig. 4.12. The optimum values of n and T for SPEs must be in the upper right corner of Fig. 4.12b. Hence, the lobe width corresponding to the curve furthest in this direction (upper right) is chosen. In this case, that corresponds to a width of 10. Once the lobe width is selected, the threshold is selected as the plateau

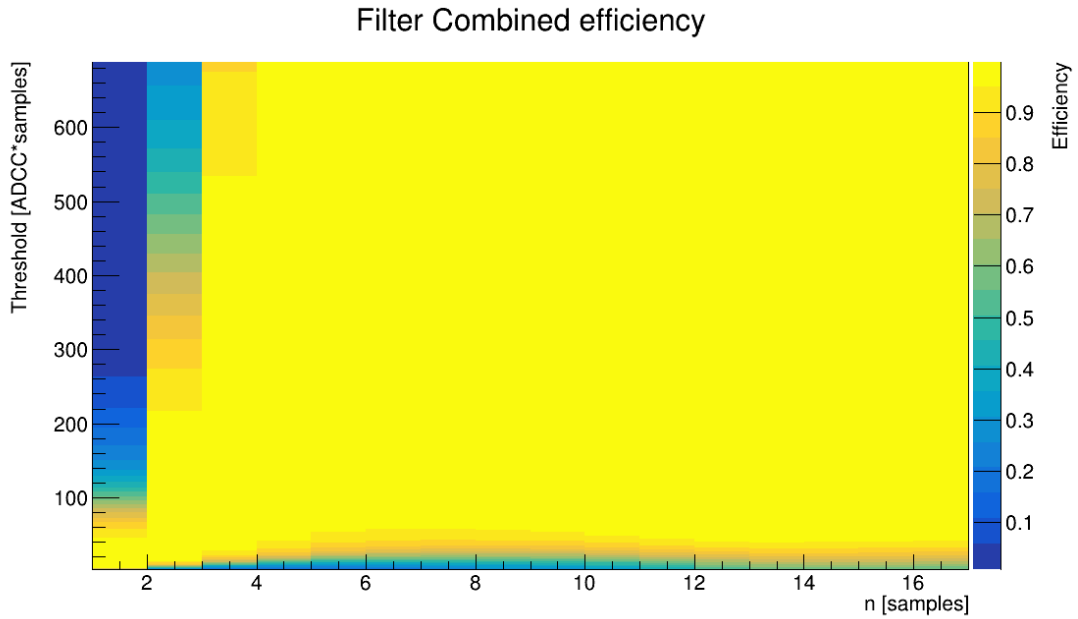

(a) Product of Efficiencies above and below $\frac{Q_{SPE}}{4}$. i.e. $E_{Prod}(n,T) = E_{SPE}(n,T) \cdot E_N(n,T)$

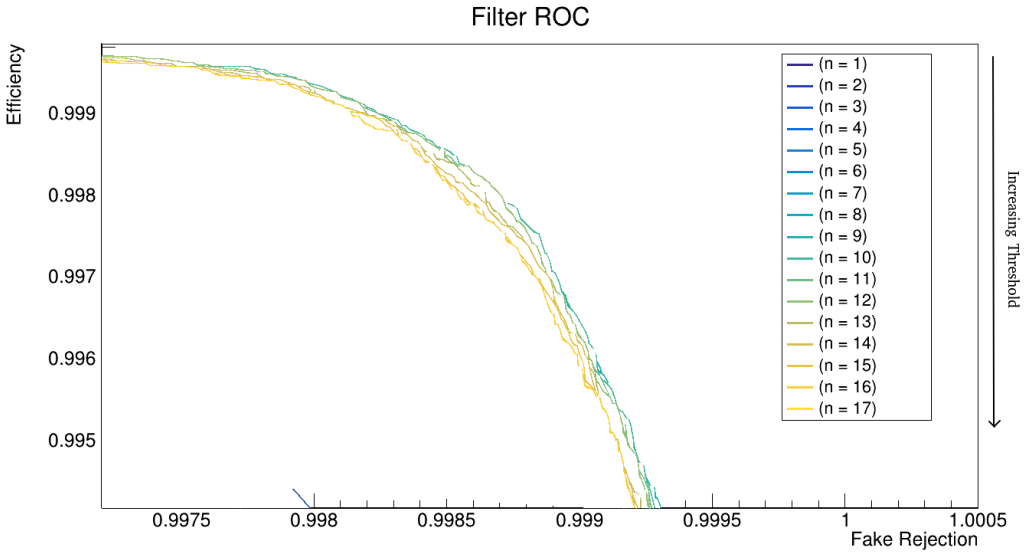

(b) ROC curve from filter efficiencies. Optimal parameters in the top right corner (maximising efficiency and rejection of false positives.

Figure 4.12

of the curve $E_{Prod}(10,T)$ (see Fig. 4.12a), giving a value of $T = 507\ ADCC \cdot\ ns$.

4.4.3 Multiplicity and Coincidence Window in Data

The multiplicity and coincidence window of the trigger are to be determined based on a comparison of pulses in random trigger data. Since the random trigger data represents an unbiased sampling of the pulse phase space. Using the energy scale shown in Fig. 4.10, the 2.2 MeV Hydrogen capture gamma is determined to be equivalent to 483 phd. Since this is such a large signal, the threshold set above is scaled up. Several configurations of coincidence window, multiplicity, and threshold scaling are tested.

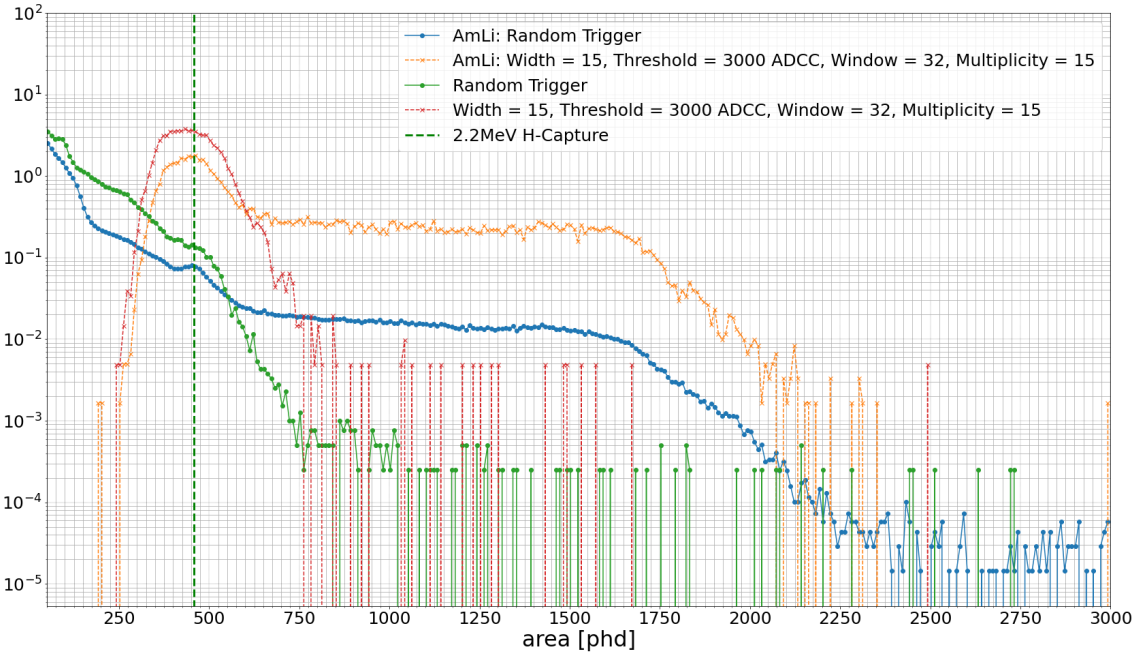

Figure 4.13: Spectrum of pulses triggered on for the selected configuration, compared with the spectrum from a random trigger. Runs are taken both with and without an AmLi source deployed. The dashed green line shows the location of the 2.2 MeV H-Capture.

The spectra of trigger pulses for the selected configuration both with and without use of an AmLi source are shown in Fig. 4.13. One observes excellent acceptance of the 2.2 MeV line and larger pulses, the boosted statistics of the OD Trigger in the large area region is testament to this. The AmLi data provides confirmation that the Hydrogen peak is captured and is above the trigger turn on. It is also promising

to note that the shapes of the random trigger and the OD trigger spectrum are consistent, having strikingly similar endpoints. The final parameters for the trigger are specified in Table. 4.1.

Lobe Width [ns]	Threshold [ADCCns]	Multiplicity	Coincidence Window [ns]
150	3000	15	320

Table 4.1: The final trigger configuration selected.

4.4.4 Efficiency

The efficiency of the final OD S1 trigger is determined using the OCS to generate pulses of varying size at, above and below the Hydrogen peak. These are produced using three fibres 11, 14, and 18, shown in Fig. 4.14.

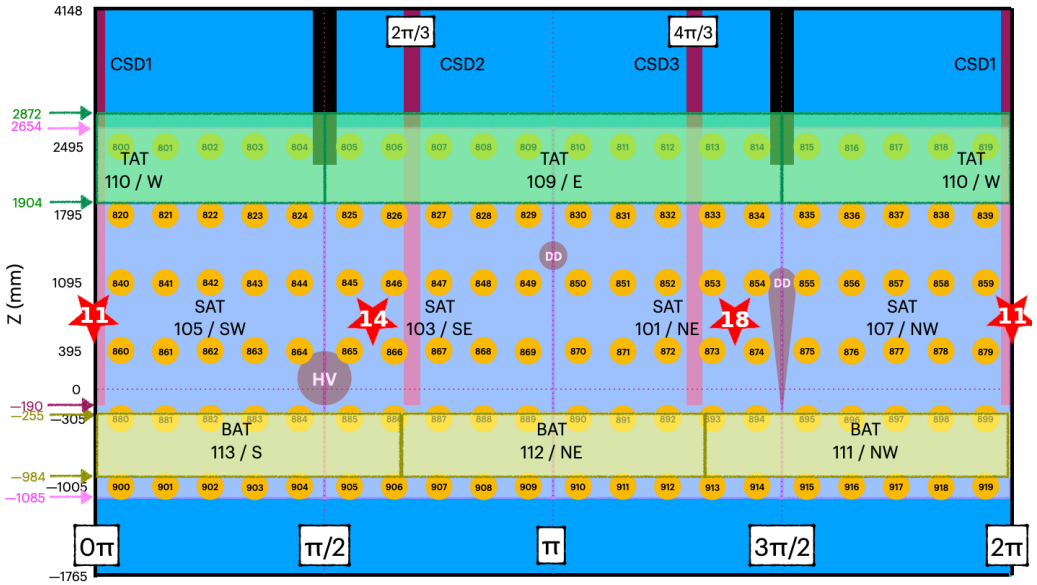

Figure 4.14: View of the OD unwrapped in θ with selected fibre locations shown in the red stars. In this view the OD Side Acrylic Tanks (SAT), TOp Acrylic Tanks (TAT), and Bottom Acrylic Tanks (BAT) are visible. The fibre locations were chosen to span the full angular range of the detector. In addition the locations of TPC HV, CSD, DD calibration conduits are highlighted.

The LZ DAQ triggers on the OCS injection pulse along with a flag denoting activation of the OD Trigger. As a result the efficiency is simply the ratio of the

pulses passing the neutron trigger logic to the total number of injected pulses. The OCS pulses are selected based on timing since the signal at the PMT has a consistent time delay from the OCS trigger pulse. This is due to travel time of photons in the fibres and of the electrical signal on the boards. The distribution of observed pulse

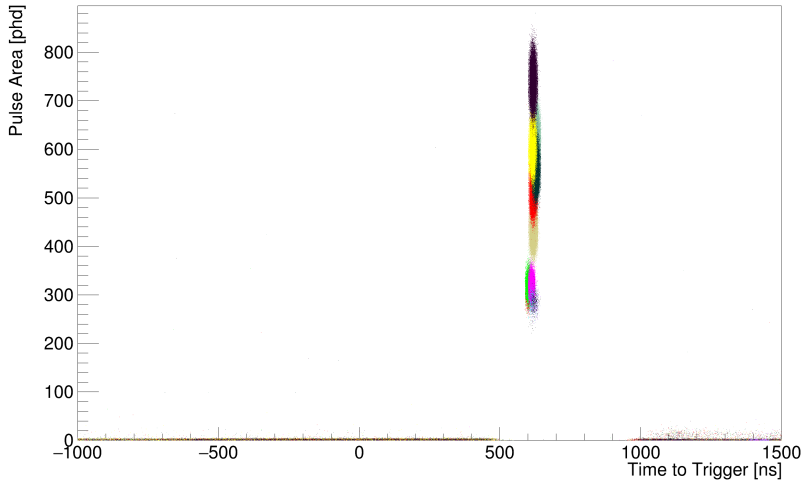

(a)

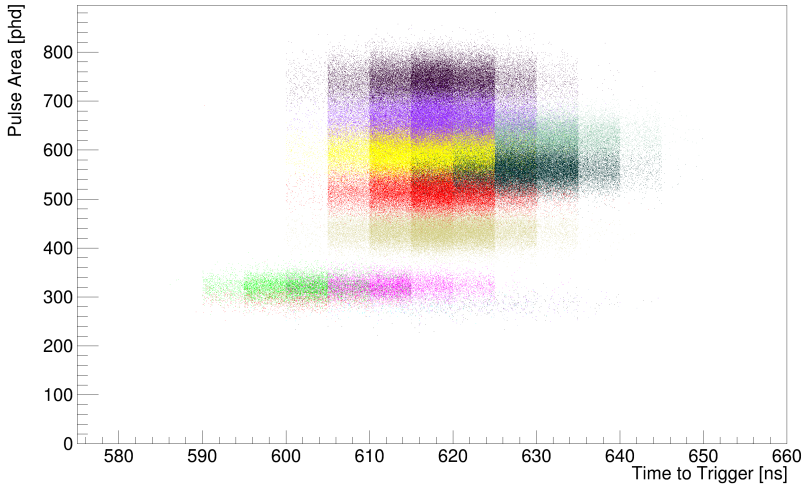

(b)

Figure 4.15: Time against pulse area for all OCS runs. 4.15a shows the full event window. 4.15b zooms into the clean region of OCS pulses where almost no low area noise pulses are observed. Each coloured population is a unique run with an OCS fibre. The most important feature here is the narrow time distribution of the OCS pulse relative to the trigger.

areas against time relative to the OCS trigger is shown in Fig. 4.15. It is observed that a cut on time provides a very clean sample of pulses with almost zero contamination

from low area noise pulses. For the remainder of this analysis one selects pulses within the time window 580 ns $<$ t $<$ 650 ns.

The average efficiency across the injections is determined by summing histograms of pulse area for each injection and calculating the ratio of the summed histogram for pulses passing both the OD neutron trigger logic and the time cut (numerator) to the summed histogram of all pulses passing the time cut. The resulting efficiency curve is shown in Fig. 4.16. The efficiency data is fit with the modified gaussian cumulative

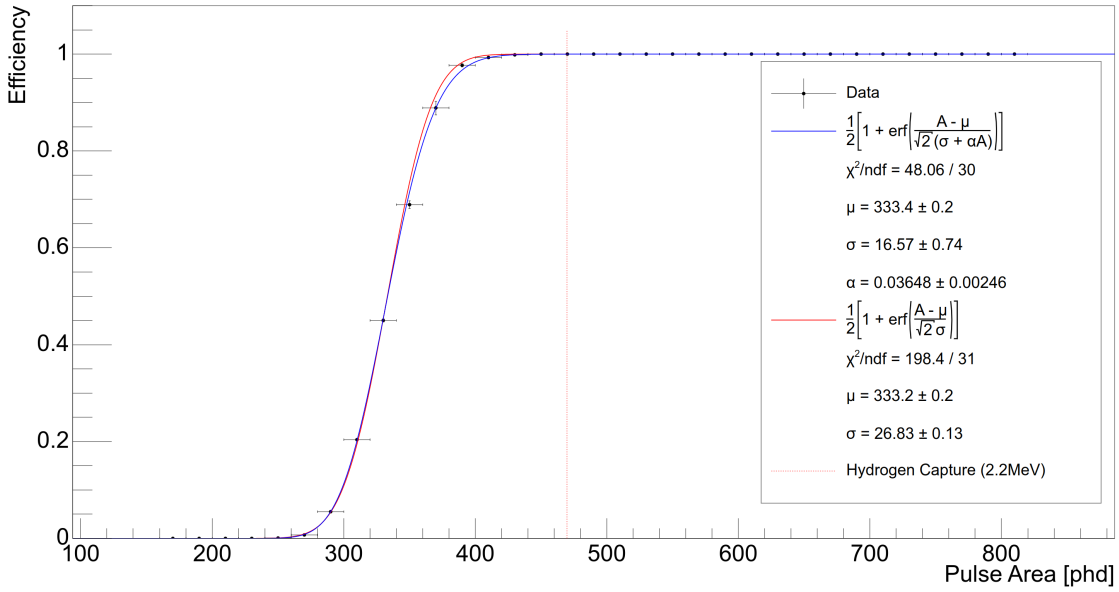

Figure 4.16: Efficiency of the OD Neutron Trigger as calculated using the OCS. Data is shown with Poisson errors as black dots. A gaussian distribution CDF curve is fit (solid red curve). A modified gaussian distribution CDF curve is fit (solid blue curve). Red dashed line shows location of Hydrogen capture 2.2 MeV peak.

distribution function (CDF) shown in Eq. 4.3; A is the pulse area, whilst μ, σ, and α are fit parameters.

$$Efficiency(A) = \frac{1}{2}\left[1 + erf\left(\frac{A - \mu}{\sqrt{2}(\sigma + \alpha A)}\right)\right] \tag{4.3}$$

The parameter, α, introduces an area dependent modification to the denominator allowing a far superior fit to the data compared to the standard gaussian distribution

CDF. From the data points and the fit, one observes excellent (100%) trigger efficiency for pulses at or above the hydrogen capture peak as expected.

4.5 Concluding remarks

Having used the approaches defined in Chapter III to calibrate the installed and running OD PMTs, all parameters are within requirements. These calibrations are monitored throughout the operation of LZ, acting as a health check of the detector.

An independent trigger of the OD was developed, with the aim of boosting statistics for higher energy processes such as the Gd capture and H capture. This is useful for monitoring the ambient neutron environment, and studies involving muons which also produce large pulses but are rarer events. An assessment of the trigger efficiency using injected pulses from the OCS found a (100%) trigger efficiency for pulses at or above the hydrogen capture peak.

CHAPTER V

A Few Gammas From Davis

As part of the first on-site expedition made by the author, before assembly and installation of the LZ detector, measurements were made to asses the γ-ray output of radioisotopes in the Davis Cavern rock. Maintaining a low background rate and understanding said background inside the OD from sources external to the detector, such as the γ-rays from natural radioactivity in the cavern, is essential for its role as a veto. This is due to considerations of the false veto rate and the amount of excluded data, both of which will increase with the rate in the OD. The content of this chapter is based on a publication written by this author and colleagues [83]. In writing this publication, this author took the leading role in the calibration and efficiency analysis, in addition to key roles in the overall simulations and analysis of the measurements.

Radiometric surveys of the Homestake mine show that most of the rock at the same depth as the Davis Cavern (4850 ft) is of the 'Homestake formation'. The content of ^{238}U, ^{40}K, and ^{232}Th found in samples of the Homestake formation is shown in Table 5.1[1]. Geological surveys have also identified veins of rhyolite in the rock. The rhyolite has much higher activity than the homestake formation, particularly in the ^{238}U and ^{232}Th chains which produce the most penetrating γ-rays. The expected distribution of rhyolite is shown in Fig. 5.1. Further to this, a layer of shotcrete

[1]Isotopes from these decay chains form the overwhelming majority of the cavern background radiation

~12.7 cm thick covers the walls and ceiling of the cavern, whilst the floor is covered by ~0.5 feet of low radioactivity concrete.

Sample	^{40}**K (Bq/kg)**	^{238}**U (Bq/kg)**	^{232}**Th (Bq/kg)**
Homestake	297.2	2.7	1.3
Rhyolite	1291.0	108.0	44.1
Shotcrete (average)	272.4	23.3	11.6
Concrete	380.8	26.7	13.0
Shotcrete (new sample)	216.7	21.4	11.4
Water tank gravel	35	26.4	1.7

Table 5.1: Measured activities from radio-assay of rock, shotcrete and gravel samples [84]. The rock and older shotcrete measurements are the average of several samples. The shotcrete and gravel samples were extracted from the Davis cavern during the time of the measurements.

The ^{238}U and ^{232}Th decay chains contain a series of α and β decays, but since they are embedded in the rock, γ-rays can be induced by reactions with light nuclei [85]. The signature γ-rays from these decay chains are:

- ^{238}U: 1.73 MeV, 2.119 MeV, and 2.204 MeV γ-rays from ^{214}Bi
- ^{232}Th: 2.614 MeV γ-rays from ^{208}Tl (highest energy signature from these chains)

In addition, ^{40}K emits a 1.461 MeV γ-ray with ~10% branching ratio.

Measurements of the γ-ray flux at 800 ft, 2000 ft, and 4550 ft depths at SURF, conducted with a NaI detector, indicate that the flux at different locations on the same level can vary by up to 30% [86]. Hence further measurement is necessary to determine the γ-ray flux in the Davis cavern and inform background estimates for LZ.

5.1 Setup

For this study a Harshaw NaI(Tl) detector was used, pictured in Fig. 5.2. This detector is equipped with a 5 inch diameter by 5 inch height NaI(Tl) crystal with a

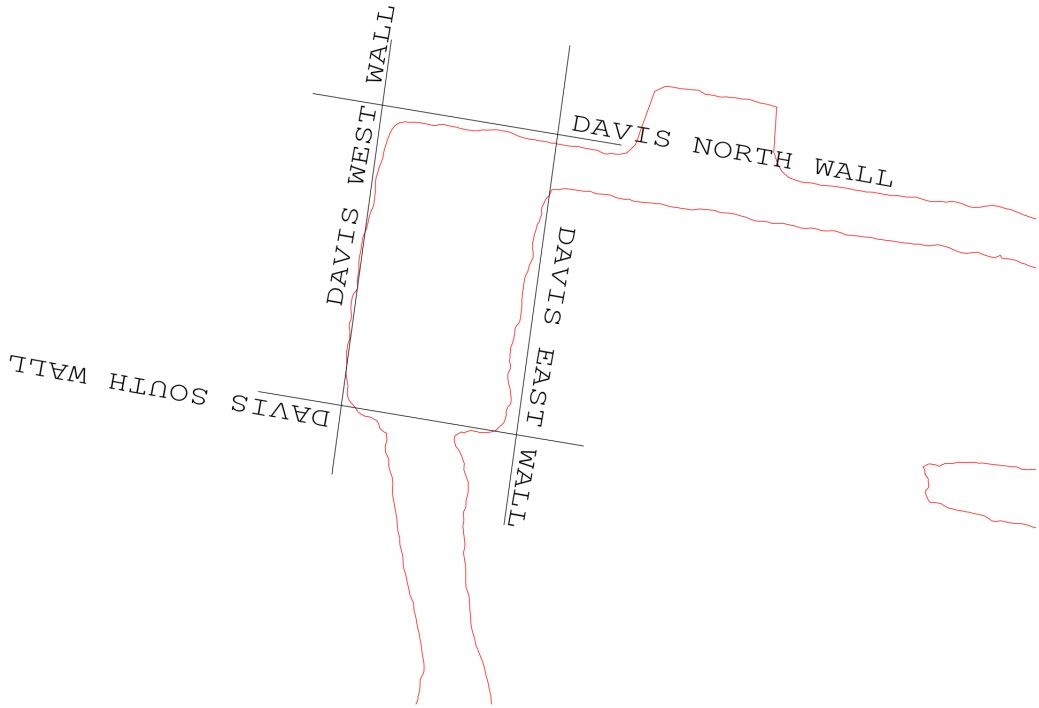

(a) Schematic of the Davis cavern and adjoining drifts, with the naming convention of the walls.

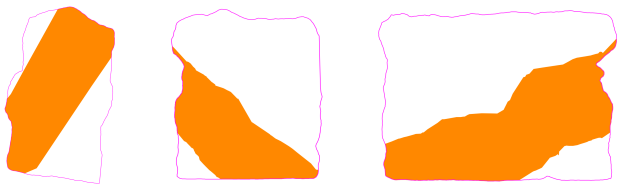

(b) Floor (c) North Wall (d) West Wall

Figure 5.1: Expected location of the rhyolite intrusions in Davis Cavern.

single 5 inch PMT, connected to a NOMAD 92X-P portable γ-spectroscopy unit.

Nine background measurements were conducted, three unshielded and six shielded (see Fig. 5.3). The unshielded measurements were taken at positions a), d), and e).

Shielding was achieved using lead bricks (2×4×8) inch which were used to construct an enclosure of 8 inch thickness around the detector with one side left unshielded (see an example in Fig. 5.4). Shielded measurements were taken at positions a), b), and c). Four shielded measurements at position a) were taken, with the detector unshielded from above, below, east, and west; the remaining shielded measurements were taken at positions b) and c), both unshielded from below. The three

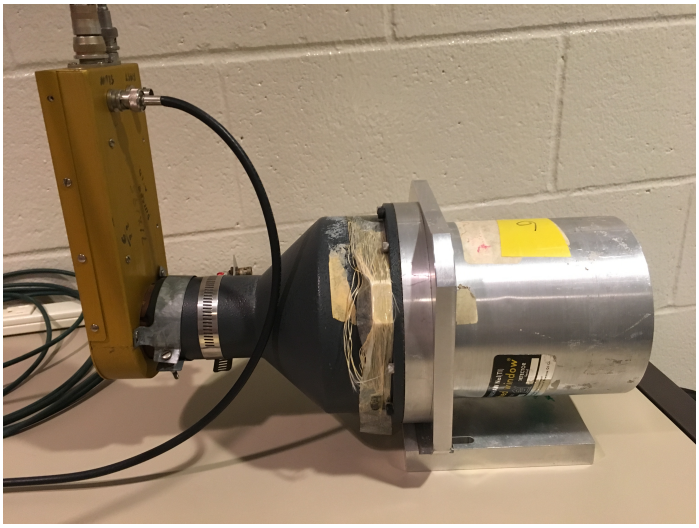

Figure 5.2: 5-inch NaI(Tl) detector, showing the preamp, PMT and NaI crystal.

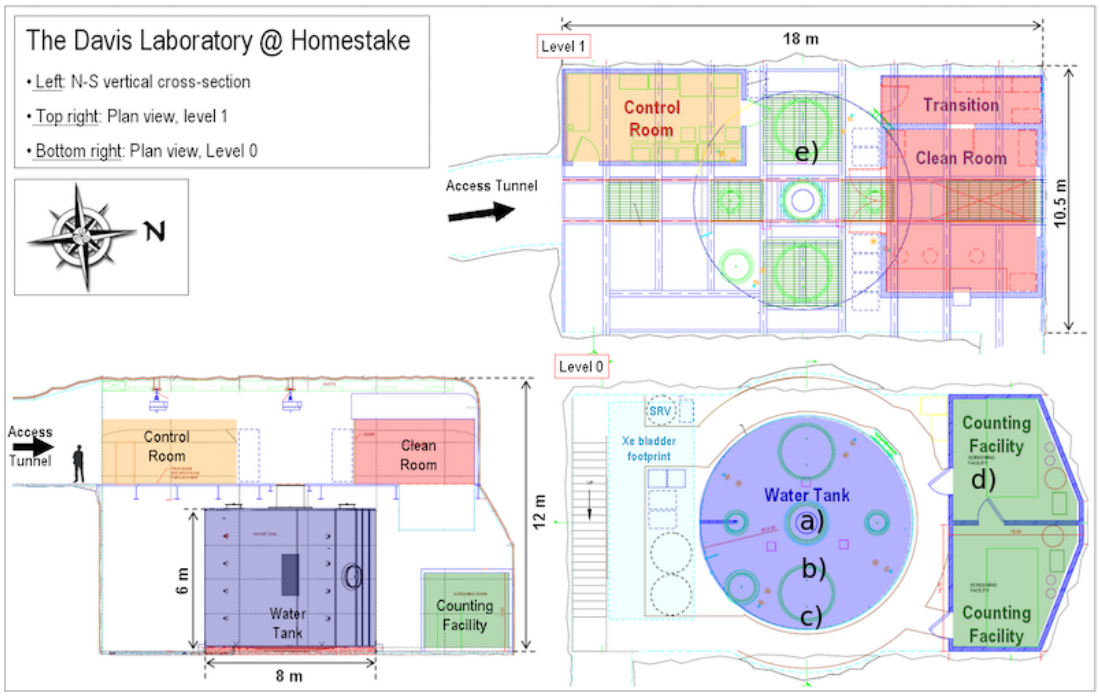

Figure 5.3: Layout of the Davis cavern with measurement positions denoted. Positions a), b), and c) are on the water tank floor. Position d) is in the east counting room, and position e) is in the upper Davis approximately 3.4 m above the water tank centre.

measurements unshielded from below, were taken to assess the attenuation provided by the steel pyramid under the water tank. Position c) is beyond the reach of the pyramid, position b) is attenuated by half of the pyramid (6 inches of steel), and

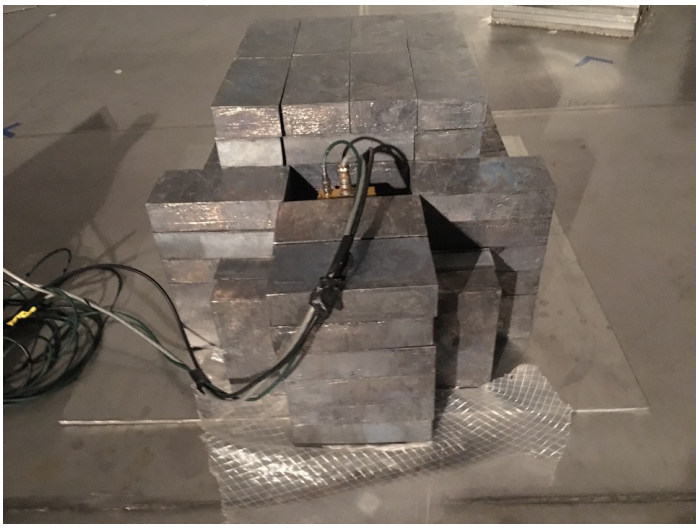

Figure 5.4: Shielding configuration for measurement looking down at position a).

position a) is attenuated by the full pyramid (12 inches of steel). The labels by which these measurements are hereafter referred to by are elucidated in Table 5.2.

Location	Label	Description
a	Pos0	Centre, unshielded
a	Pos1	Centre, looking up
a	Pos2	Centre, looking down
b	Pos3	Halfway to south edge, looking down
c	Pos4	South Edge, looking down
e	Pos5	Upper Davis, unshielded
d	Pos6	East Counting Room, unshielded
a	Pos7	Centre, looking east
a	Pos8	Centre, looking west

Table 5.2: Positions and descriptions of all measurements along with the label they will hereafter be referred by.

Before each measurement, a rough energy calibration was performed using a ^{60}Co source and the MAESTRO software to determine the 2.5 MeV coincidence peak [87], with the scale adjusted to ensure that the 2.614 MeV ^{208}Tl peak would be within the range of the spectrum. Further calibration spectra were collected with ^{137}Cs, and ^{228}Th sources. All of these calibration measurements were taken such that the efficiency and resolution scale of the detector could be assessed.

5.2 Detector Calibration and Efficiency

A ^{60}Co source calibration was performed before each measurement. The gain of the NOMAD unit was adjusted so that the sum peak at 2505 keV was visible, ensuring that the dynamic range was adequate to fully contain the 2614 keV peak from ^{208}Tl for the background measurements. ^{60}Co, ^{137}Cs, and ^{228}Th calibration sources were used in order to assess detector efficiency and resolution. Each calibration spectrum was fitted with Gaussians and exponential backgrounds in order to determine the location and resolution of the 1173 keV, 1332 keV, and 2505 keV peaks for ^{60}Co, the 662 keV peak for ^{137}Cs and the 2614 keV peak from ^{208}Tl (a product of the ^{228}Th decay chain). All calibrations were performed in the centre of the water tank on the floor; the unshielded measurement in that position was used to subtract the cavern background from the calibration spectra. These spectra are shown in Fig. 5.5.

Using the peaks in the ^{60}Co spectra a calibration curve relating the PMT channels to an energy is obtained and shown in Fig. 5.6, where good linearity is observed.

From these fits the integrated rate in each peak is calculated. This rate, however includes the efficiency of the detector, which must be extracted and corrected for when comparing the cavern flux measurements to simulation results. The absolute efficiency (ϵ_A) has contributions from the geometric efficiency, depending on the fraction of solid angle the detector is exposed to, the intrinsic efficiency which describes the conversion of incident γ-rays into counts in the spectra, and a light collection efficiency. The absolute efficiency is used to estimate the over prediction of detected rates from BACCARRAT simulations, and is given by:

$$\epsilon_A(E) = \frac{N(E)}{A \times P_\gamma(E)}, \tag{5.1}$$

where $N(E)$ is the integrated rate for a photopeak of energy E, A is the activity of the source, and $P_\gamma(E)$ is the probability of a single decay producing a γ-rays of

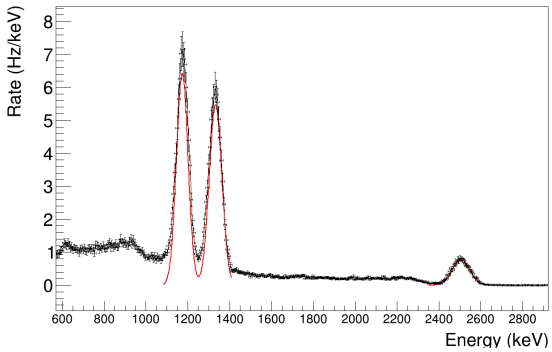

(a) Background subtracted ^{60}Co calibration spectrum.

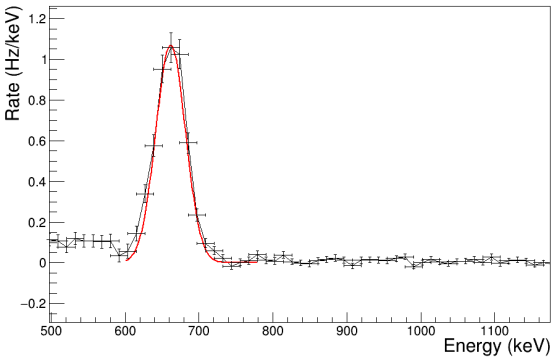

(b) Background subtracted ^{137}Cs calibration spectrum.

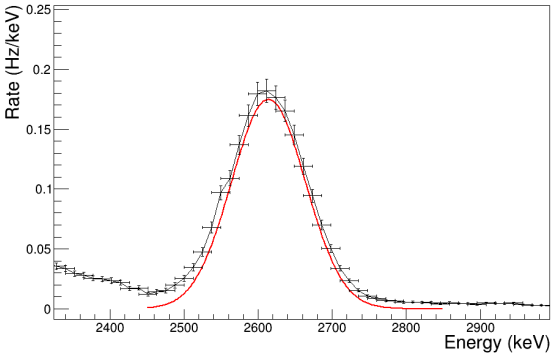

(c) Background subtracted ^{228}Th calibration spectrum.

Figure 5.5: Calibration spectra data (**black**) with a gaussian fit to the peaks (**red**).

energy E. The correction factor required is simply a ratio of the absolute efficiency in data to the absolute efficiency in simulation. The resulting efficiency correction factor is 0.90 ± 0.06.

A further parameter of interest is the resolution scale of the detector. The resolution (R) of each peak is calculated from the full width at half maximum (δE), and the energy (E) of that peak. From these calculations the resolution scale can be determined from a fit to a resolution model obtained from Ref. [88]:

$$R = \frac{\Delta E}{E} = \sqrt{\alpha^2 + \frac{\beta^2}{E} + \frac{\gamma^2}{E^2}}, \tag{5.2}$$

where α describes the light transmission from the scintillating crystal to the photo-

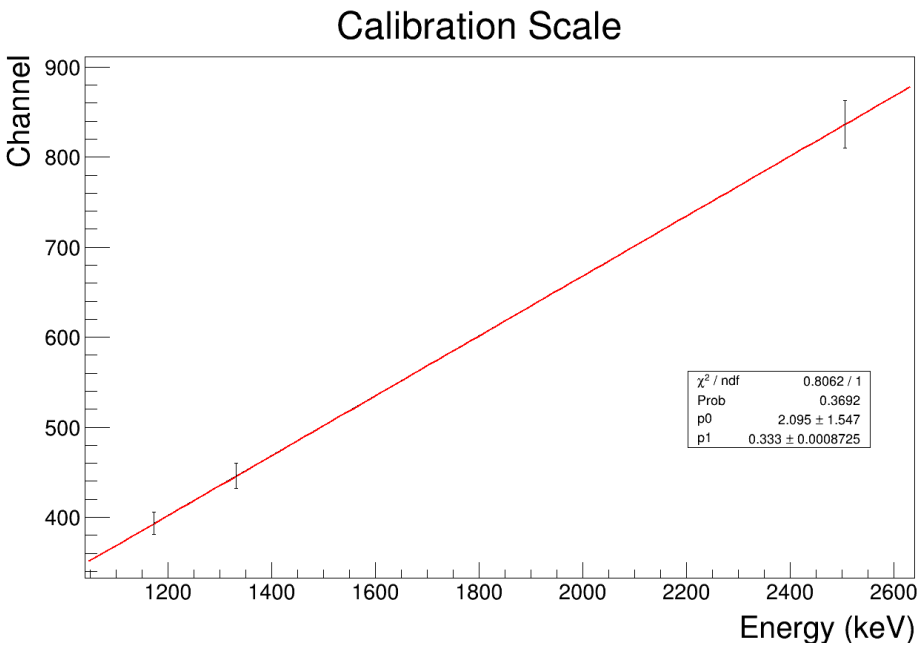

Figure 5.6: Energy calibration curve extracted from fits in Fig.5.5.

cathode, β is the statistical fluctuations in photon production, attenuation, conversion and amplification, and γ is the contributions of noise. This resolution model is shown

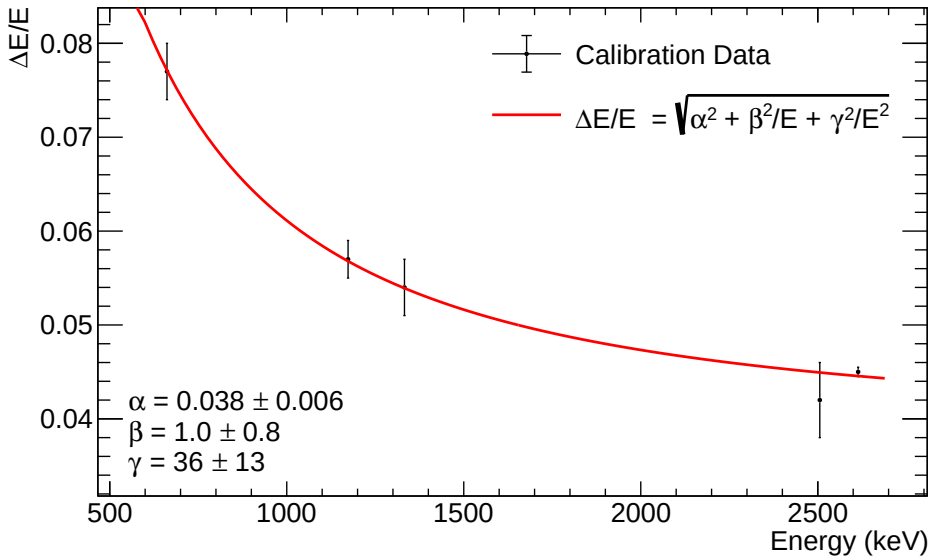

Figure 5.7: Resolutions fit to Eqn. 5.2.

in Fig. 5.7, and is used to apply a correction to true energy deposits in Monte Carlo simulations of the cavern γ-flux for direct comparison with the NaI data

5.3 Measured Rock Spectra

In Fig. 5.8, spectra for all nine measurements can be seen. Table 5.3 shows

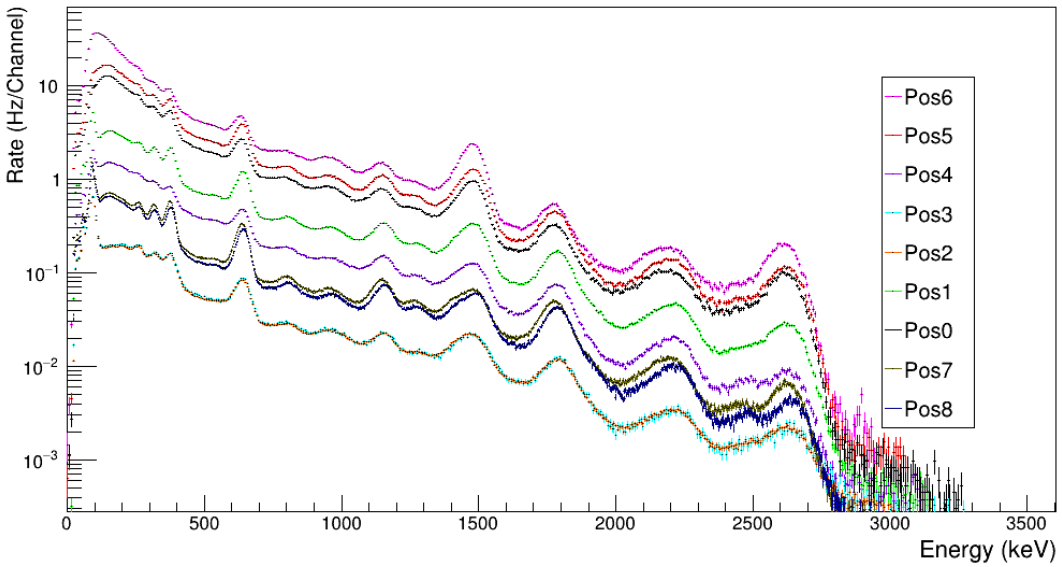

Figure 5.8: The energy spectra for all nine measurements in the energy range 0–3000 keV. The three signature peaks are visible at 1.76 MeV from ^{214}Bi, 1.46 MeV from ^{40}K and 2.61 MeV from ^{208}Tl. Several more peaks from ^{214}Bi are visible at 609 keV, 1.12 MeV, 2.12 and 2.20 MeV.

the rates extracted from these spectra. The differing live times were dictated by

Label	**Start Date**	**live time (hours)**	**Avg. Radon (Bq/m^3)**	**Rate (Hz) Total**	**Rate (Hz) $>$ 200 keV**
Pos0	24/10/17	4.0	422 ± 34	595.7 ± 0.2	386.0 ± 0.2
Pos1	18/10/17	20.2	372 ± 76	203.57 ± 0.05	139.0 ± 0.04
Pos2	19/10/17	117.0	500 ± 155	16.715 ± 0.006	10.427 ± 0.005
Pos3	17/10/17	17.9	336 ± 55	17.15 ± 0.02	10.70 ± 0.01
Pos4	16/10/17	18.2	358 ± 80	94.17 ± 0.04	64.40 ± 0.03
Pos5	26/10/17	3.6	868 ± 222	794.4 ± 0.2	512.0 ± 0.2
Pos6	26/10/17	2.1	929 ± 70	1355.0 ± 0.4	750.9 ± 0.3
Pos7	25/10/17	22.3	316 ± 46	106.33 ± 0.4	59.14 ± 0.03
Pos8	24/10/17	17.3	359 ± 37	95.11 ± 0.04	51.77 ± 0.03

Table 5.3: Measurement dates, live times, radon concentrations and integrated count rates. Here, 'looking down (up)' refers to the shielding configuration where only the underside (topside) of the detector is not shielded by lead. Uncertainties on rates are Poisson counting errors only.

time available underground at SURF, with shielded measurements given priority for

overnight data-taking to account for the lower rate. The overall measured rates were highest in the east counting room, followed by the upper level of the Davis cavern and the centre of the water tank. Differences in rate can be attributed to shielding, the proximity to the steel pyramid and differences in the structure and material of the floor.

For the west and east facing measurements, no significant asymmetry was observed in comparison to the differences in activity of the rhyolite versus the Homestake rock and shotcrete. The rhyolite intrusion is thought to be present on the west wall (see Fig. 5.1), but the rate from this direction was measured to be about 10% less than the east facing measurement in total rate. This suggests a lack of a significant flux of γ-rays from rhyolite surviving through the shotcrete layer, and the observed difference may be due to unevenness in shotcrete thickness since the shotcrete is approximately 10 times more radioactive than the Homestake formation in ^{238}U and ^{232}Th (see Table 5.1.

For the measurements facing downwards at the steel shielding pyramid, the total rate measured above 30 cm of steel in the centre was within 3% of the rate in the position at half of the tank radius, where the detector was just shielded by 15 cm of steel, as can be seen by the two lowest rate histograms overlapping in Fig. 5.8. The measurement at the edge of the tank, with no steel beneath, had a higher rate. As the gravel under the water tank is known to be relatively low in radioactivity, we assume that the rate measured in Pos2 and Pos3 - the lowest - correspond to the intrinsic background of the experimental setup, including the NaI detector, as NaI(Tl) crystals are known to have intrinsic ^{40}K, ^{238}U and ^{232}Th contamination [89] and PMTs are also known sources of radioactivity. Contributions from the lead shielding are expected to be subdominant to the detector.

Radon in the cavern air resulting from natural emanation must also be considered; decays from below ^{222}Rn make up a majority of the γ-rays in the ^{238}U chain. There is

no specific mitigation of underground radon levels at SURF, where the total average radon concentration in the Davis Campus is approximately 310 Bq/m^3, with a seasonal dependence resulting in a winter low of 150 Bq/m^3 [84]. However, during some days of data acquisition, unusually high radon levels were recorded, due to changes in airflow in the mine drift outside of the Davis Campus. The average recorded radon concentration (measured with an AlphaGuard detector) for each dataset is also shown in Table 5.3, but it should be noted that radon data was taken in an area outside the main entrance to the cavern known as the common corridor, so some uncertainties remain over the air circulation differences between this location and where the γ-ray data was taken, but the concentrations were significant enough that γ-rays from radon must be included in this analysis.

5.4 Simulations and Analysis Approach

This work utilizes the LZ simulation package BACCARAT [73], described in Chapter II. BACCARAT includes custom features such as detailed detector and cavern geometry, event generators for the specific backgrounds of interest to LZ (neutrons and γ-ray activity from detector materials, muon induced neutrons, and cavern rock γ-rays), and the NEST[75] (Noble Element Simulation Technique)package which handles the details of Xe micro-physics. An event biasing technique is applied to accelerate the simulation; this was developed for LZ background simulations of the cavern due to the low probability of a γ-ray surviving through the water shield, outer detector and the skin layer of liquid xenon. ^{238}U, ^{232}Th and ^{40}K decays are initiated within a 30 cm thick layer of material surrounding the cavern at the approximate location of the cavern walls. The event biasing technique involves saving γ-rays on a predefined surface, then propagating them onward with the same momentum in a second simulation with a multiplicative factor in order to increase γ-ray statistics. This can be done multiple times on surfaces of decreasing size around a target detector volume.

A custom simplified geometry featuring the cavern, pyramid, water tank and detector was created, with options to use each of the lead shielding configurations to expose the NaI detector from either above or below. The cavern and the surrounding rock are modelled as a cuboid with internal space of $20 \times 14 \times 12$ m; this is larger, by design, than the dimensions of the Davis cavern (Fig. 5.3) to conserve the simulated surface area with reality due to unevenness of the cavern walls. Radioactive sources were placed within a 30 cm thick 'shell' on the inside of this cavern rock.

A simulation study done for experiments at the Modane Underground Laboratory have shown that due to attenuation, a 30 cm concrete/shotcrete shell configuration is sufficient to produce more than 96% of the total γ-ray flux without needing to include emission from the underlying rock [90]. This approximation is expected to hold also for the Davis cavern; in places, both the wall and the concrete are 30 cm thick, and the ratio of shotcrete to rock activities is in most cases higher than at the Modane Underground Laboratory, making the rock contribution less prominent. The cavern rock is simulated using the chemical composition of a Homestake sample and is a mixture of oxides, primarily SiO_2, Al_2O_3, FeO and water [91]. Discrepancies between simulation and data for different measurement positions may indicate a deviation from this simplified model, such as a contribution from γ-rays from the more radioactive rhyolite beneath the shotcrete.

For analysis of the calibration and cavern spectra, the NaI geometry is modeled in BACCARAT, and placed inside the LZ water tank in the Davis cavern. However, this simulation doesn't include the resolution of the NaI, which comes from the intrinsic efficiencies involved in conversion of energy deposits by γ-rays into scintillation photons. Nor does it include the efficiency for detection of scintillation photons by the PMT. These parameters, as determined by the calibration data, are be used to find correction factors for the simulations of the cavern rock spectra at each position.

For input into future LZ simulations, the simulated activities of isotopes within

the shell in Bq/kg are required to reproduce the measured rate in the NaI data. Since the Compton background in the simulation is unlikely to be accurate due to the lack of many features of the real cavern and objects within it in the simulation, the analysis focuses on the γ-ray lines with energies of 1400 keV and above where the Compton background is less dominant. The simplest technique is to fit Gaussians for the four most prominent lines at 1461 keV (^{40}K, BR: 10.66%)), 1764 keV (^{214}Bi, BR: 15.30%) , 2204 keV (^{214}Bi, BR: 4.92%) and 2614 keV (^{208}Tl, BR: 99.75%). Choosing to focus on the photopeaks selects predominantly γ-rays that have been produced near the surface of the cavern walls, as they have travelled to the detector without any Compton scatters.

Finding an analytic function to model the non-gaussian background to these photopeaks is a rather difficult task. As such, a template probability distribution function (PDF) based on smeared simulations are used for the fitting procedure. The prominent γ-ray lines mentioned above (the signal to be fit) are removed from the simulated spectra before smearing is applied. Energy deposits by conversion of γ-rays inside in the NaI crystal were recorded and then smeared by a Gaussian function using parameters from the fit of Eqn. 5.2 to calibration data shown in Fig. 5.7. This was done separately for ^{40}K, ^{238}U and ^{232}Th. Fig. 5.9 shows an example of a simulated energy spectrum summed over ^{40}K, ^{238}U and ^{232}Th in true energy deposits before and after smearing. The signal PDFs for the fits are generated using Gaussian functions whose widths are also constrained using the resolution function from Fig. 5.7.

Additionally, due the high levels of radon present at the time of the measurements, the ^{222}Rn decay chain was simulated within the cavern air and inside the water tank and the rates normalised using the measured concentrations. In the fit, one allows the radon contribution to float within 20% of the measured concentration, attempting to generously account for the unknown variations in air circulation between the Alphaguard detector location and the NOMAD unit locations in this study.

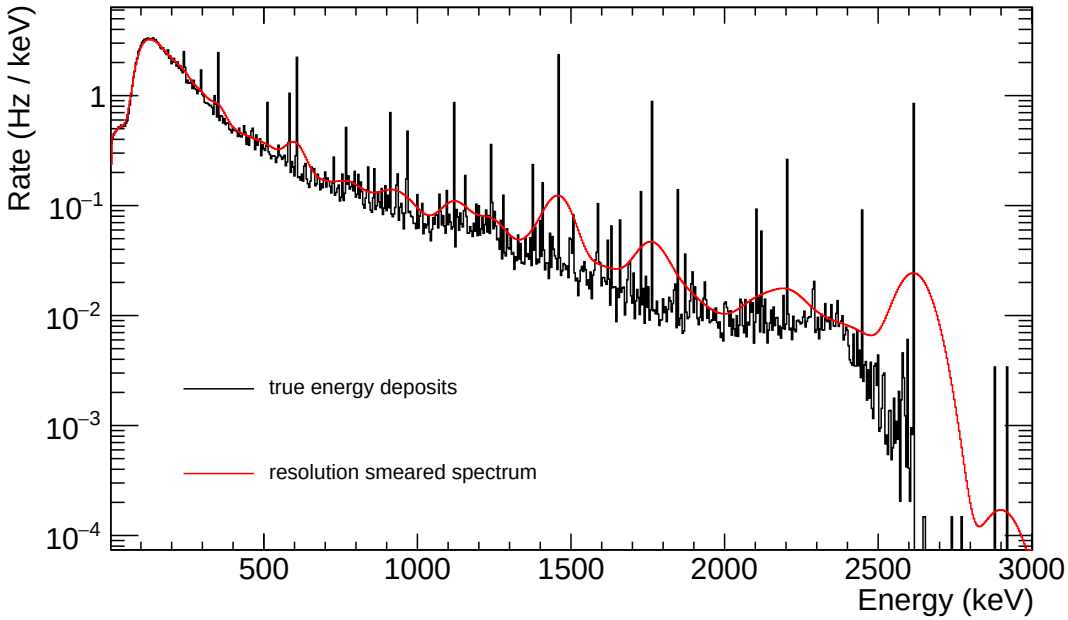

Figure 5.9: An example energy spectrum obtained in simulation for Pos0. The black histogram shows true energy deposits where photopeaks from various lines are visible, whilst the red line shows the result of smearing with the resolution obtained from Eqn. 5.2.

For each of the 1461, 1764 and 2614 keV peaks (denoted by the subscript i for isotope) in each measurement (denoted by the subscript m), a corresponding activity was determined using the comparison to the simulated rate in each peak:

$$A_{i,m} = \frac{R_{i,m} - R_i^I}{\varepsilon R_{i,m}^{sim}}, \tag{5.3}$$

where $R_{i,m}$ is the rate in each signal peak in data determined by the Gaussian fit, R_m^I is an internal rate calculated from the average of measurements Pos2 and Pos3 - these were shielded by both lead and the steel pyramid so are subtracted to account for the intrinsic background of the set up, ε is the aforementioned efficiency correction determined from calibration, and the rate in the simulated peak, $R_{i,m}^{sim}$ is calculated using:

$$R_{i,m}^{sim} = \frac{N_{i,m}}{N_{i,m}^{tot} B_m M}, \tag{5.4}$$

where $N_{i,m}$ is the raw number of counts in a given peak for isotope i and measurement position m, $N_{i,m}^{tot}$ is the total number of initial events simulated, B_m is the event biasing multiplicative factor for measurement m, and M is the mass of the simulated shell. This is equivalent to simulating 1 Bq/kg for each isotope and determining the necessary scale factors to match data.

Fitting of the calibration spectra is done with ROOT's TMinuit library [92]. The rock spectra are fit using the ROOFIT implementation of this library [93].

5.5 Rock Spectra Analysis Results

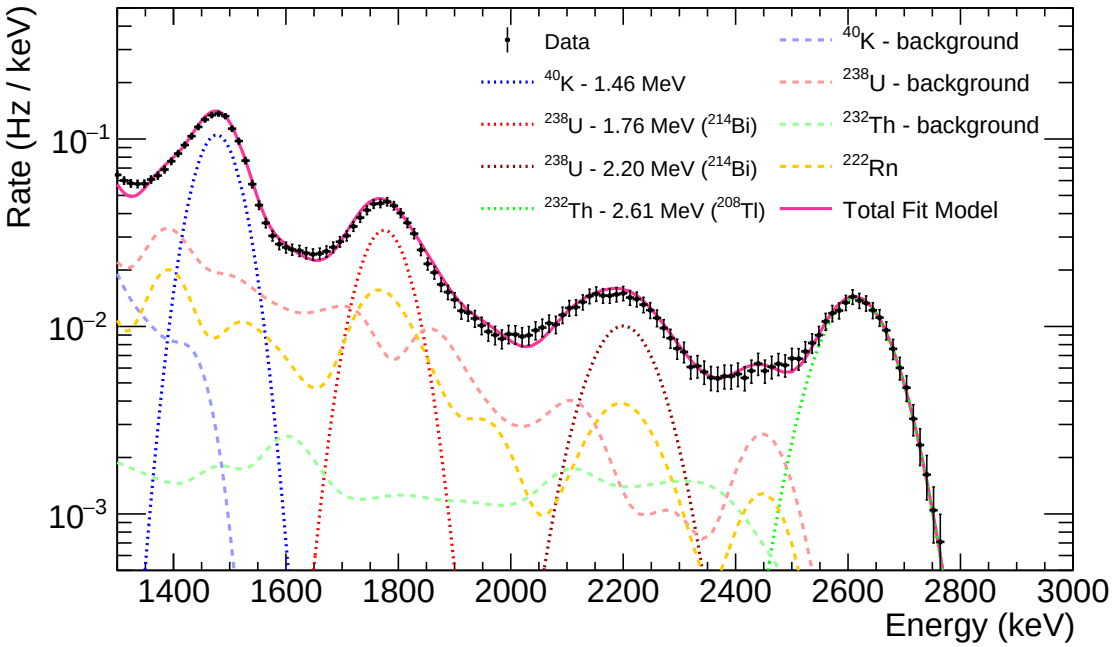

Figure 5.10: Fitted energy spectrum for position (a) showing the 1461 keV ^{40}K line, the 1764 keV and 2204 keV lines from ^{238}U and 2614 keV from ^{232}Th, background contributions from other, less dominant lines and Compton scattering, and in yellow, the airborne radon contribution.

Using the procedure described in the prior section, an example of the resulting fit to the unshielded data taken in the centre of the water tank is shown in Fig. 5.10. The resulting rates, $R_{i,m}$, activities, $A_{i,m}$ extracted from these fits are shown in Table 5.4. Large variations in both key quantities are observed between positions as a result of

several sources of uncertainty.

Label	^{40}K - 1461 keV		^{238}U - 1764 keV		^{232} Th - 2614 keV	
	Rate (Hz)	A_m (Bq/kg)	Rate (Hz)	A_m (Bq/kg)	Rate (Hz)	A_m (Bq/kg)
Pos0	10.33 ± 0.04	285 ± 1	2.55 ± 0.02	36.9 ± 0.4	2.12 ± 0.02	15.2 ± 0.1
Pos1	3.47 ± 0.01	214 ± 1	1.29 ± 0.01	48.4 ± 0.2	0.650 ± 0.004	9.5 ± 0.1
Pos2	0.300 ± 0.001	-	0.157 ± 0.001	-	0.0560 ± 0.0004	-
Pos3	0.167 ± 0.002	-	0.141 ± 0.002	-	0.0487 ± 0.0001	-
Pos4	1.01 ± 0.01	182 ± 2	0.875 ± 0.005	31.4 ± 0.2	0.214 ± 0.002	16.7 ± 0.1
Pos5	13.82 ± 0.07	135 ± 4	1.56 ± 0.02	10.4 ± 0.2	2.498 ± 0.004	8.8 ± 0.1
Pos6	28.8 ± 0.1	264 ± 1	2.98 ± 0.03	18 ± 0.2	4.31 ± 0.03	12.2 ± 0.2
Average	-	220 ± 60	-	29 ± 15	-	13 ± 3

Table 5.4: Fit results for the three signature lines for each isotope/decay chain. The best fit activities, A_m, are given for each measurement - except the two lowest rate positions, where the contribution from the cavern is minimal. The uncertainties are from fit results only; a larger systematic uncertainty can be expected from the simplified simulation model. The average values are show at the bottom with their standard deviations.

One major factor is the radon concentration in the cavern. Since most of the γ-rays produced in the uranium chain are emitted in the late chain decays (^{222}Rn daughters), there is a great deal of overlap between the spectra of these two sources. Whilst this was allowed to float within 20% of the measurements, lack of specific and detailed information on the airflow around the Davis Campus during these measurements and the unusual radon concentration fluctuations means this uncertainty could very well account for the large variation in ^{238}U activities.

Additionally, the simplified geometry implemented in the simulation lacks several features of the cavern. These include, the steel grating separating the upper and lower Davis, the walls of the counting room and the control room. These features may impact the peak to continuum ratios in the data.

Furthermore, the observed variation in activities may be an indication of non-uniformity in concentrations of each isotope within the cavern walls. Given the measured activities in Table 5.1 and the size of the rhyolite intrusions identified, the variations in activity observed in this work are not high enough to be attributed to rhyolite.

Treating each measurement as an independent observation of the same γ-ray flux within the cavern results in the average activities shown in the last row of Table 5.4. From these averages, one calculates this flux for energies exceeding 1 MeV to be 0.35 ± 0.08 $\gamma\text{cm}^{-2}\text{s}^{-1}$. This is consistent with the upper limit of 2.19 $\gamma\text{cm}^{-2}\text{s}^{-1}$ above 1 MeV in Ref. [94]. Normalising simulated rates in each peak with these average activities gives good agreement across all measurements and is sufficient to estimate background rates fo the LZ experiment. If necessary, measured radon levels at SURF can be used to scale this flux if further large excursions are observed during operation of the detector.

Another cross-check of the data quality is to compare the relative branching fraction between the 609 keV(BR: 45.5%) and the 1764 keV(BR:15.5%) lines from ^{214}Bi. The measured relative branching fraction in the data was 0.34 ± 0.01. This is an excellent match to the expected value of 0.336.

Shotcrete undergoing HPGe screening contained ^{40}K, ^{238}U, ^{232}Th levels of 272 Bq/kg, 23 Bq/kg and 12 Bq/kg respectively for averages of samples during construction, and the more recent sample contained 220 ± 30 Bq/kg, 21 ± 1 Bq/kg, 11.4 ± 0.4 Bq/kg (see Table 5.1), showing agreement within uncertainties with the results of this analysis. This suggests the dominant contribution to the γ-ray flux in the Davis cavern is the shotcrete layer, with no measurable excess or directionality due to rhyolite.

5.6 Concluding remarks

The γ-ray flux inside the Davis cavern at SURF was measured with the corresponding radioactive contamination levels found to be 220 ± 60 Bq/kg of ^{40}K, 29 ± 15 Bq/kg of ^{238}U, and 13 ± 3 Bq/kg of ^{232}Th; consistent with the shotcrete material used to coat the cavern walls. Radon in cavern air was found to produce a significant contribution to the measured rate, and there is no conclusive evidence for a significant flux from the high radioactivity rhyolite intrusion within the cavern nor asymmetric

flux in the cavern.

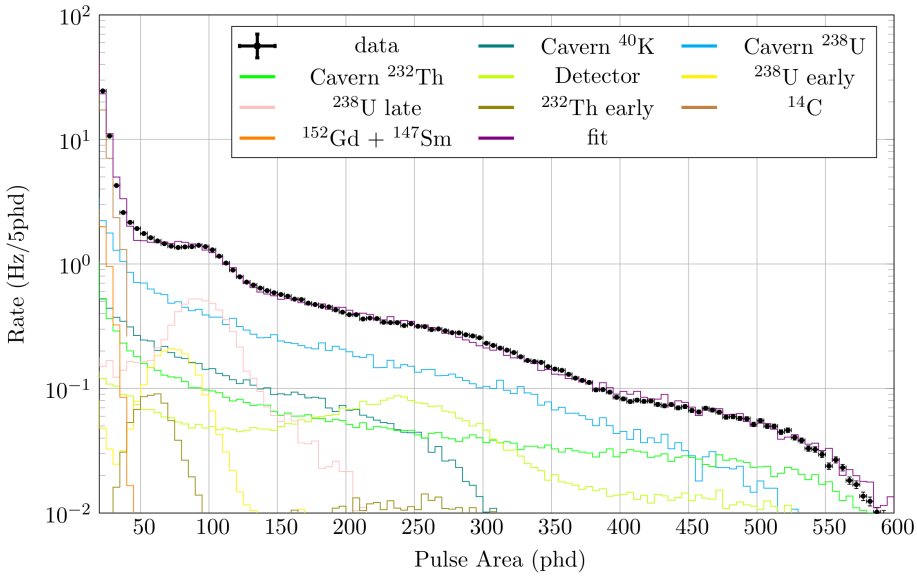

Figure 5.11: Contribution from each OD background source to the measured OD spectrum. Only components with a contribution greater than 1 Hz have been included. The dominant source of background are the cavern γ-rays studied in this chapter, particularly above 500 keV (102 phd), where it accounts for $\sim$50% of the total OD background rate. Figure adapted from from [69]

These results inform estimates of the background contribution from the Davis cavern for LZ as shown in Fig. 5.11. Here, a fit of the OD backgrounds was conducted, with the results showing the dominant source coming from the cavern γ-ray spectra measured in this chapter, contributing $\sim$50% of the total OD background rate above 500 keV.

CHAPTER VI

A Fist Full of Protons

As mentioned in Chapter II, the WIMP signal in LZ is a single nuclear recoil in the TPC without coincidence in the veto systems. A crucial background to this signal is neutrons. Being a neutral, non-relativistic (mostly) particle, the neutron is capable of replicating the WIMP signature. Thus it is crucial to understand the ambient neutron environment of the detector, the response of the detector to neutrons, and to minimize them where possible. Whilst neutrons can mimic the WIMP signal, they are far more strongly interacting, thus one expects them to interact multiple times in the TPC and/or Veto subdetectors. This provides a vital avenue to assess the impact and likelihood of singly interacting neutrons based on neutron calibration source measurements in the detector as a whole, and neutron signals captured by the OD trigger.

The major sources of fast neutron (1-20 MeV) flux in LZ are (α,n) reactions and spontaneous fission of ^{238}U (USF) in detector components and the ever-generous walls of the Davis Cavern. When a nucleus is bombarded by an alpha particle, a nuclear reaction can take place whereby the alpha particle is absorbed and results in the emission of a neutron, this is the (α,n) process. The remnant nuclues after neutron emission is typically in an excited state, and emits gammas as it decays to its ground state. Whilst a full neutron spectrum from the cavern walls has not

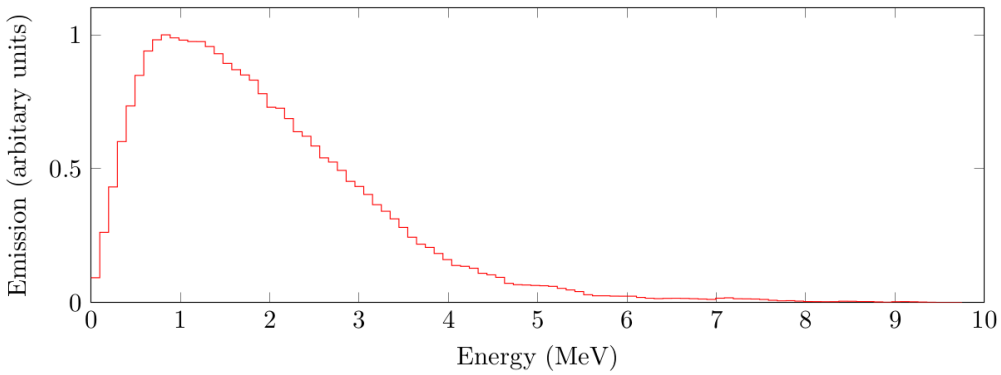

Figure 6.1: Expected merged spectrum of neutrons from the (α,n) and USF processes. Figure adapted from Ref. [97]

been generated, the overall flux of thermal neutrons has been measured with a ^{3}He detector at 1.7$\pm$0.1(stat)$\pm$0.1(sys) [95]. One of the most prolific actors with regards to (α,n) is ^{19}F in PTFE, which has a rather high cross-section for this interaction [96]. The resulting excited ^{22}Na remnant decays to its ground state producing a flurry of prompt gammas, before further decaying to ^{22}Ne with a half-life of 2.6 years. The combined expected neutron spectrum from (α,n) and USF is shown in Fig. 6.1

Observed captures in the OD and multiple scatters in the TPC serve to mitigate the impact of the neutron background. However, veto via capture in the OD requires that these neutrons first thermalise; given the danger posed by this background, it is prudent to seek a method to measure and identify those neutrons which fail to fully thermalise and capture. In what follows the proton recoil interactions in the OD are discussed as potential direct measure of the fast neutron environment in LZ.

6.1 Proton Recoils

Fast neutrons can scatter elastically on protons which produce an ionization signal in the GdLS dependent on the recoil energy. Since the proton and neutron have very similar masses, the relation between recoil energy (E_p) and incident neutron energy

(E_n) simplifies to:

$$E_p \;=\; E_n cos^2(\theta). \tag{6.1}$$

Taking an average over θ one arrives at a mean recoil energy of $E_n/2$. The key question is: For what recoil energies, hence neutron energies, is the ionization signal above the OD threshold of 100 keV?

At this point it is prudent to refer to the discussion of light yield and quenching in Chapter II. Due to the high electro-negativity of Hydrogen (protons), there is a significant amount of chemical/ionization quenching. From the measurements in [55], the light yield in the GdLS from recoiling protons is determined to be a factor ∼3-5 lower than for electrons/gammas of the same energy. Thus a much larger ionization signal is required to cross the detector threshold. To reach above the 100 keV threshold for electrons/gammas, a proton would need to deposit ∼500 keV. Whilst a high bar, this is certainly reachable given that LZ expects to observe neutrons of ∼1 MeV and above.

Though the highly ionizing nature of protons (compared to electrons/gammas) leads to reduced light yield, it also leads to a higher population of triplet states which have a slower decay time than the singlet states. Hence the decay time of scintillation light produced is measurably longer. This property can be used to attempt to distinguish them from the gamma background produced by the cavern walls and radioactive impurities in the detector.

6.1.1 Approach to tagging

The procedure one takes in an effort to identify, or 'tag' proton recoils, one must first define a signal and background population. The signal population is taken from neutron calibration data. With a neutron source, one knows that the data collected must include the recoils being searched for. In order to clean this dataset and maximize its purity, events must be selected based on a correlated feature that is more

easily identifiable. The neutron capture on Gd is one such feature. By selecting events which contain pulses of 3 MeV or larger (captures) and looking at pulses occurring before the capture pulse, one reduces the dataset to events which contain a neutron which has thermalised in the GdLS. Since neutrons thermalise by scattering, the selected population must contain proton recoils. The purity of this population is evaluated based on simulations of the calibration source. The background dataset used here will be taken from gamma calibration sources, in addition to the capture pulse itself, since this too is a gamma signal. Once these datasets have been selected, one attempts to build a discriminating variable using the pulse level reconstructed quantities (see Section 2.6). After which point a simple likelihood estimator is used to asses its effectiveness. This estimator takes the form:

$$\mathcal{L}(S|x) = \frac{S(x)}{S(x) + B(x)}, \tag{6.2}$$

where x is the discriminating variable in question, $S(x)$ is the signal distribution of x, and $B(x)$ is the background distribution of x.

6.2 Simulations

One uses simulations to inform selections on neutron calibration data to maximise purity of the signal sample one collects. The DD neutron source is chosen as a starting point since it produces a mono-energetic beam of 2.5 MeV neutrons. At this energy one expects a good quantity of proton recoils above the ∼500 keV to study. Recording the number of photons produced by gammas and proton recoils incident on PMTs results in Fig. 6.2. From this it can be seen that 500 keV proton recoil deposits correspond to pulses of ∼30 phd and equivalent gammas of 150 keV. Now, to determine the expected purity of the signal sample, one looks at events containing a capture gamma pulse. Energy selections are applied to the capture gamma pulse

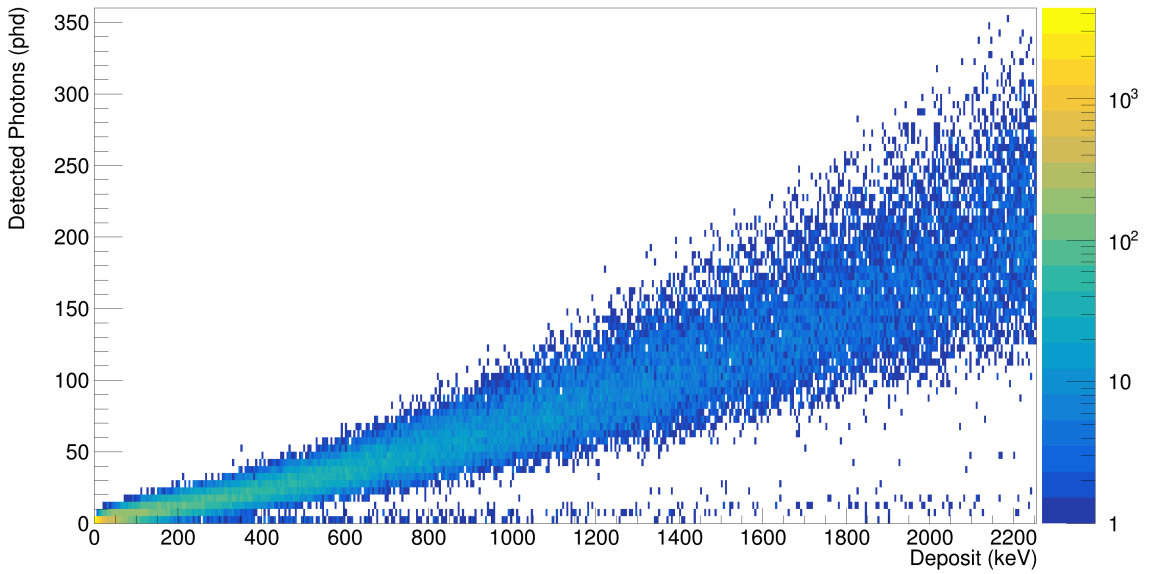

(a) Deposits by recoiling protons.

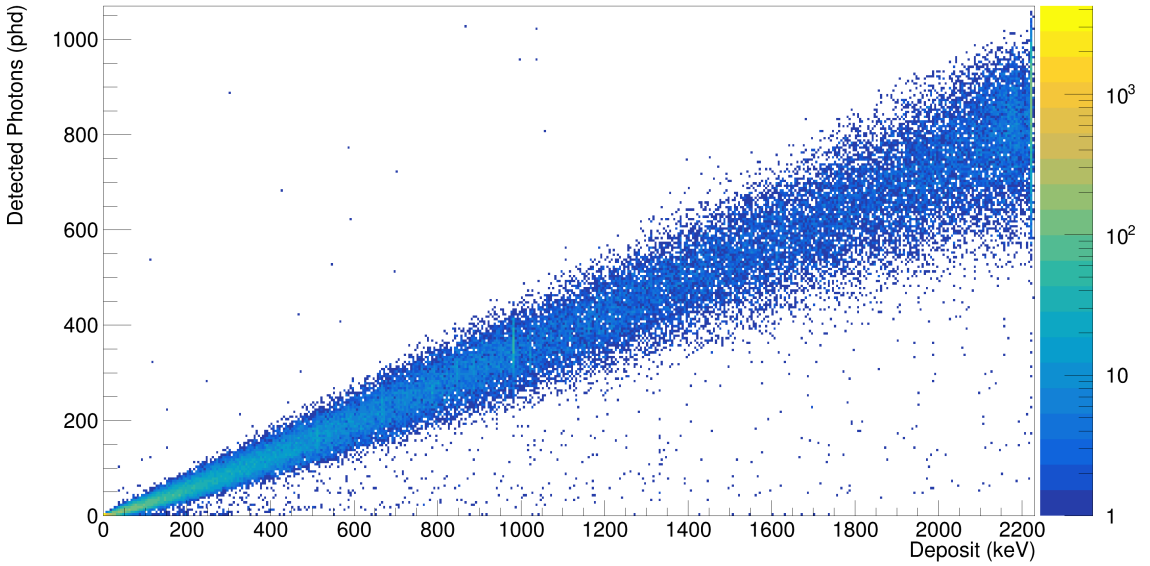

(b) Deposits by gammas.

Figure 6.2: Photons observed by PMTs as a function of energy deposited by recoiling protons (6.2a) and gammas (6.2b).

(spectrum shown in Fig. 6.3). Observed in this figure are the long shoulder from the multiple Gd capture gamma spectrum ending at ∼8 MeV, in addition to the peak from the 2.2 MeV hydrogen capture gamma.

Requiring at least a 2 MeV deposit from a capture means one captures all events involving both Hydrogen and Gd capture. However if one also considers background

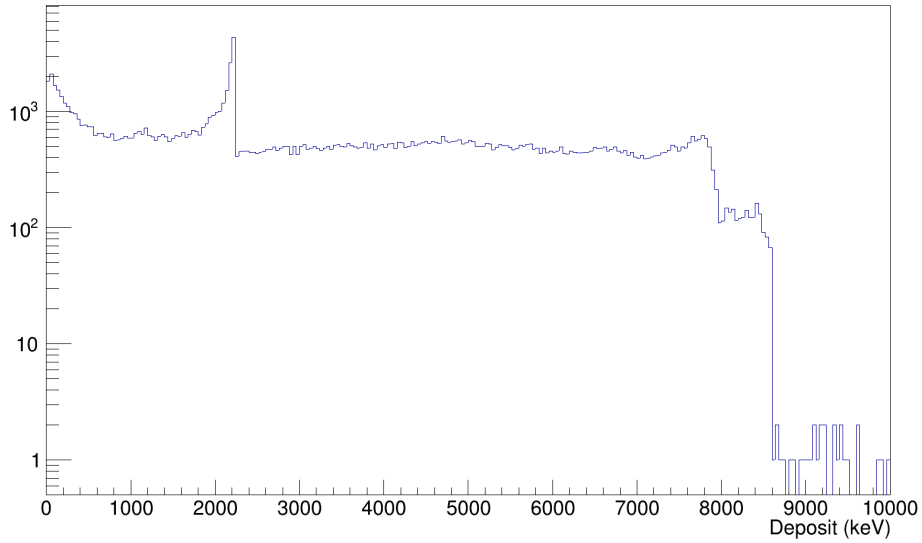

Figure 6.3: Spectrum of capture gamma deposits resulting from the DD simulation. The 2.2 MeV hydrogen capture peak is clearly visible, as are the endpoints for Gd capture appearing around 8 MeV. There are two endpoints visible which correspond to the slightly different total capture gamma energies from the different Gd isotopes [98, 99, 100, 101].

gammas, the purity of this selection suffers. Since, when utilizing the OD S1 trigger specified in Section 4.4, either the triggering pulse is the capture pulse or it is a large gamma not produced by a capture and the capture pulse occurs later in the event. The event during data collection has a pre-trigger window of 1.5 ms; given the OD background rate of 85 Hz above 200 keV (see Fig. 5.11 and [69]), there is a $\sim$13% likelihood of accidental gammas occurring in this window in the best case where the triggering pulse is a capture. This contamination worsens when one considers the 4.5 Hz of OD background above 2 MeV which could be falsely attributed to captures. The 3 MeV selection removes the vast majority of the false capture pulses since the OD background rate above this region is less than 10 mHz, leaving one with a 33 % efficiency for selecting events containing a proton recoil.

This however, does not remove the accidental background gamma pulses which may be selected as recoil candidates. Being more selective of the timing window relative to the capture pulse, within which these candidates are selected is be more

effective at this. The distribution of time from proton recoil to capture signal is shown in Fig. 6.4. From here it is observed that 98.8% of recoils coincident with a capture occur within a window of 300 μs before the capture signal. This is consistent with the capture time distribution expected when the foam spacers between the OCV and the acrylic tanks is considered (see [69]). Given this window and the 85 Hz of background rate above 200 keV, one calculates a ~2% likelihood of accidental gammas contaminating the signal selection. As such this selection is used in addition to the

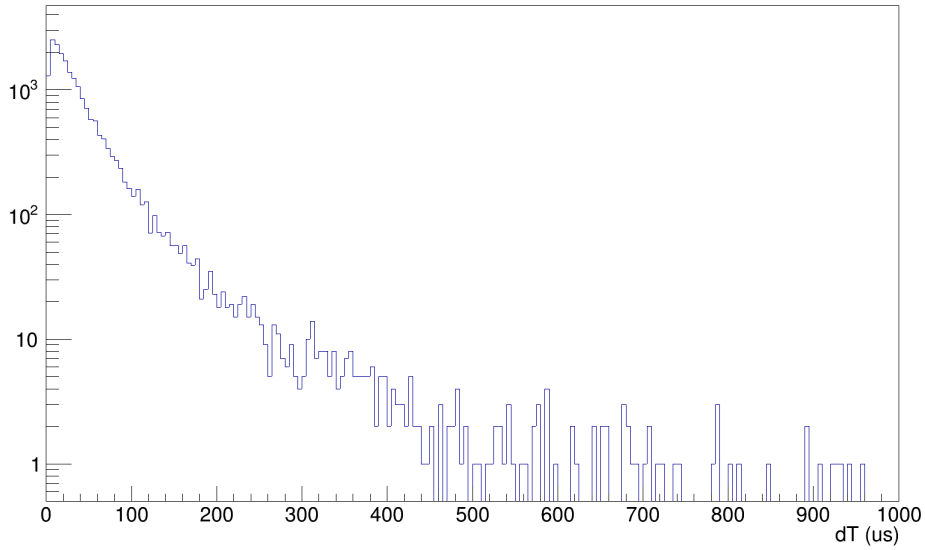

Figure 6.4: Time delay between capture and proton recoil from simulation. Can be observed that 95% of the recoils occur within the 300 μs preceding capture.

3 MeV capture pulse selection and the 500 keV recoil selection. This selection criteria brings the selection efficiency to 32 %. A summary of the fraction of proton recoil events selected given various selections on the observed capture signal are shown in Tab. 6.1.

6.3 Calibration Data

In the DD calibration dataset, one defines a series of selections to select for the recoil candidates to use for the signal sample. Informed by the simulations described

Selection criteria	Selection Efficiency (%)
No selection	17
Capture Pulse > 0	26
Capture Pulse $\geqslant 2$ MeV	31
Capture Pulse $\geqslant 3$ MeV	33
(Capture Pulse $\geqslant 3$ MeV) & 300 μs Window	32

Table 6.1: Percentage of events with proton recoil depositing over 500 keV in the GdLS given the stated selection on the capture pulse. Chosen selection criteria in **bold**.

above, these selections include a 3 MeV selection on the largest pulse (700 phd), a requirement of at least 20 phd from the candidate proton recoils which must occur within 300 μs before the Gd capture pulse.

The background dataset used for this study is made up of gamma sources covering an energy range from 122 keV to 2.6 MeV. These sources are: ^{57}Co, ^{54}Na, ^{228}Th, and ^{22}Na. On this dataset, pulses are selected for based on pulse area (Energy). The pulse area and energy spectra of the sources used are shown in Fig. 6.5. The signature peaks

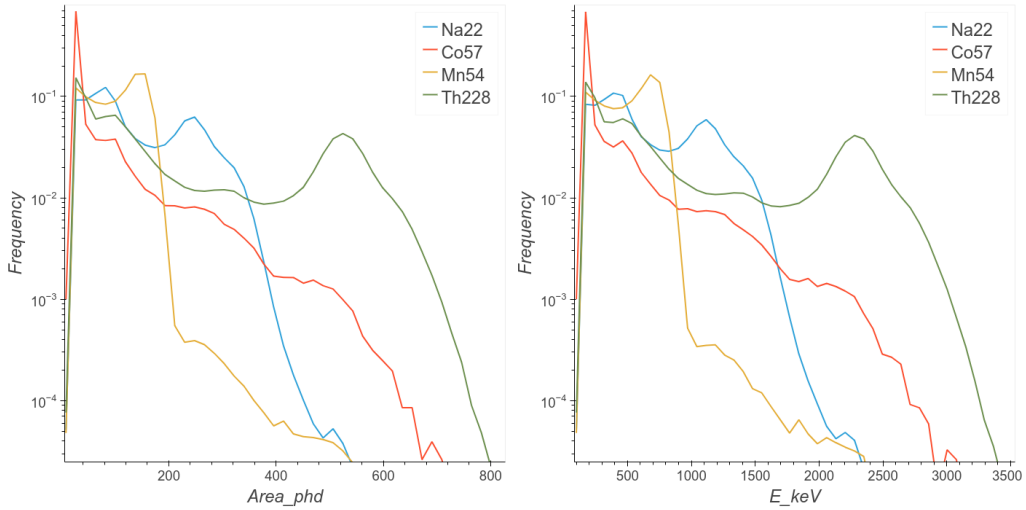

Figure 6.5: Pulse area (left) and energy spectra of sources used in this study. All spectra normalized by their integral to show spectral shape. The conversion from pulse area is achieved using the calibration scale generated from data using these same sources [82].

of these sources (see Table 2.3) are clearly visible in the spectra shown. The singular exception is the 122 keV ^{57}Co gamma, which appears as a peak in the low energy

region, though its peakedness is an artefact of having energy so close to detector threshold that it is sculpted. This is due to the source's closeness to the expected 100 keV detection threshold of the OD. This source was chosen by LZ precisely for this reason, and is included in this study due to the large quenching effect already discussed which has the potential to reduce lighter proton recoils to towards this energy. Table 6.2 details the area (Energy) selection applied.

Source	Area (Energy) Selection
^{57}Co	20 phd (111 keV) < Area (Energy) < 25 phd (138 keV)
^{22}Na	95 phd (467 keV) < Area (Energy) < 115 phd (557 keV)
^{54}Na	162 phd (764 keV) < Area (Energy) < 188 phd (878 keV)
^{228}Th	563 phd (2.45 MeV) < Area (Energy) < 638 phd (2.76 MeV)

Table 6.2: Energy selections applied to select gamma peaks associated with the decay of each calibration sources. See Table 2.3 which details the gamma lines from each of the sources. Selections are based on width of the peaks as determined by the energy scale study in [82].

6.3.1 The Parameters

After applying these selections, one begins plotting the various pulse parameters produced in the standard LZAP (see Section 2.6). Of particular interest are those which probe the timing profile of the pulses. In addition to the standard LZAP RQs, the author also calculates several composite variables. The distribution of these variables are displayed in Fig. 6.6. The standard RQs are:

- rms: The root mean square width of the pulse in nanoseconds defined as $\sqrt{\frac{\sum_j \ V_j(j-\mu)^2}{\sum_j \ V_j}}$; where the sum is over samples of the pulse, V_j is the amplitude at sample j, and μ is the weighted mean over j with V_j as weights

- prompt50: The fraction of the pulse area in the first 50 ns of the pulse

- prompt100: The fraction of the pulse area in the first 100 ns of the pulse

The composite variables are:

- AreaAmp_ns: Ratio of pulse area to pulse peak amplitude
- WidthRise_ns: Rise time of the pulse in nanoseconds (Start to peak)
- WidthFall_ns: Fall time of the pulse in nanoseconds (Peak to end)
- WidthEarly49_ns (WidthLate49_ns): Length in nanoseconds of the first (last) 49% of the pulse area
- Width98_ns: Length in nanoseconds of the central 98% of the pulse area
- Kurt: The excess kurtosis of the pulse
- Early/Late: Defined as $\frac{WidthEarly49\_ns}{WidthLate49\_ns}$
- Rise/Fall: Rise time over fall time ($\frac{WidthRise\_ns}{WidthFall\_ns}$)
- prompt50/prompt100: Defined as $\frac{prompt50}{prompt100}$
- promptdiff/prompt100: Defined as $\frac{prompt100-prompt50}{prompt100}$

These variables all relate to the time profile of the pulse and are expected to yield some information. The AreaAmp_ns in particular has been utilized before to attempt pulse shape discrimination with some success in [66]. The excess kurtosis is a fairly well known parameter derived from the fourth statistical moment. It is calculated using the waveform samples of the pulse in question as the distribution:

$$Kurt = \frac{1}{n}\frac{\sum_j (V_j - \mu)^4}{\sigma^4} \tag{6.3}$$

Where n is the number of samples to sum over, V_j is the amplitude of the pulse at sample j, μ is the mean V_j, and σ is the standard deviation of V_j. its use as a measure of the "tail fatness" of a distribution [102] was particularly attractive to the author given the efforts described in Ref. [103] where the fraction of the pulse falling in the tail was utilized.

6.3.2 The Results

Having chosen a set of variables to probe with and having applied the selections in Table 6.2, the various background datasets are combined, as are the two signal source datasets. The resulting combination is shown in Fig. 6.7. The resulting distributions show a rather dismaying amount of overlap between signal and background. This suggests poor discriminating power, but one continues, temporarily undeterred, to generate the likelihood distributions for these parameters according to Eq. 6.2. As expected from the overlap in the merged distributions of Fig. 6.8, no single parameter shows the discriminating power hoped for. However, some do show slight promise peaking at likelihoods of $\sim$0.8. It is possible that an appropriate combination of those parameters could lead to some discrimination, although that is an exceedingly difficult task to conduct by hand.

It is also of note that these distributions were normalized by their integral before computing the likelihood, not normalized to the rate of the expected contributors to the background gamma distribution and neutron distribution. Normalizing by the source rates would not be the appropriate approach since the sources provide an environment where neutron and gamma rates respectively are on close to equal footing. In order to accurately judge the performance of these parameters in the less friendly environment of source free experiment running, one must normalize using the expected rates of gamma and neutron sources in that environment. The dominant contributors to this for the OD would be the cavern gammas detailed in Chapter V, and the cavern neutron and (α,n) sources described at the beginning of this chapter. Hence this is likely the best performance these parameters can provide.

It is now prudent to discuss some effects which may be obscuring the timing information sought after.

6.3.3 Smearing of the time profile

In the pursuit of a tag using the timing profile of scintillation light several challenges must be overcome. The first is the signal size. As discussed above, the quenching of proton signals in liquid scintillator raises the minimum energy at which one expects to observe these signals. As a result of this higher threshold this study is limited to fast neutrons entering the detector. However, there are still a significant quantity of proton signals to observe.

The second key issue is whether the time profile information is preserved from the emission of the scintillation light to the pulses observed by the PMTs. The time signature of the emitted photons is necessarily smeared due to the geometry of the detector. Photons are emitted in an isotropic fashion, thus there is natural variation in the path lengths to the various PMTs. One considers the worst case variation; where the emission occurs at the closest position to the top row of PMTs[1](~80 cm radial distance and ~0 cm vertical distance); the observing PMTs are at the top and bottom most positions (~350 cm vertical separation), and maximally separated in azimuthal angle (π). The resulting variation for photons taking a direct path to the PMTs is ~280 cm, leading to ~7 ns time variation in the worst case. In the best case; the scintillation light is produced at the same radial position as the worst case and azimuthally bisects adjacent observing PMTs on the horizontal plane resulting in no path length difference due to geometry. Given the difference between the fast and slow components of scintillation decay time is 13 ns [56], this source of smearing does not prevent tagging even in the worst case.

An additional source of signal smearing is reflections on the Tyvek. As mentioned in Section 2.3.4, the OCV and the wall of PMTs is lined with Tyvek in order to improve light collection efficiency. The reflections on the Tyvek introduce a time delay to the signal dependent on the number of reflections. This source of smearing

[1]One could just as easily choose the bottom row, as this calculation would be symmetric.

is particularly dangerous since the discriminating power comes from the difference in decay time of the scintillation signal. This means accurately reconstructing the tails of the scintillation time profile is a crucial path to success. Given the factor of two improvement in light collection due to the Tyvek reflectors, one should expect at least half the photons forming the pulse to have reflected one or more times. In the best case scenario where scintillation light is produced close to the OCV and the reflected photon takes the most direct path to the PMT only $\mathcal{O}(1$ ns) of delay is introduced. However, given the diffuse reflectivity of Tyvek and the relatively low spatial density of PMTs in the OD, further reflections are likely in addition to the geometric time delay for those photons reflected directly into a more distant PMT. Fig. 6.9 shows the results of a relatively simple cross-check in simulation, comparing the spread of the distribution of photon arrival times with and without reflection. From this it is clear that with reflections indeed have a large smearing effect. One approach attempting to mitigating this, is to use only the prompt component of the pulse. Alas, since the valued discriminatory information appears in the tail of the distribution, thus it would be lost in the process. It is promising though, that even with the smearing effect of reflections, separation becomes more visible at higher energies. This occurs at recoil energies in excess of 2 MeV, which are generally outside the reach of the (α,n) and spontaneous fission process being targeted by this study. However, such high recoils would not be beyond the reach of cosmic ray muon-induced neutrons, which produce fast (1-20 MeV) and ultra-fast (>20 MeV) neutrons [104].

6.4 Concluding remarks

It can be seen that, despite quenching effects, proton recoils produce a signal that is certainly observable in the OD. In addition they are observed to occur within the veto window, hence are excluded in the WIMP search. However, the Tyvek reflector proves to be a double-edged sword. Whilst it succeeds in its task of improving light

collection efficiency, allowing the detection of scintillation signals as low as 100 keV, the reflections introduce a smearing in the time profile of the signal. This prevents direct tagging using pulse shape discrimination in the regime studied using any one of the variables identified. Although, given the non-zero difference between signal (proton recoils) and background (gammas) in the distributions of the variables explored, a combination of these variables could yield a sufficiently robust discriminator. As such a combination is difficult to picture, this would be an appropriate problem to tackle using machine learning to pick up on features that may be missed by a human analyzer. It is also possible that avenues still exist to explore the energetically dizzying heights of muon-induced neutrons. However, exploration of these avenues is left as an exercise for the sufficiently motivated reader.

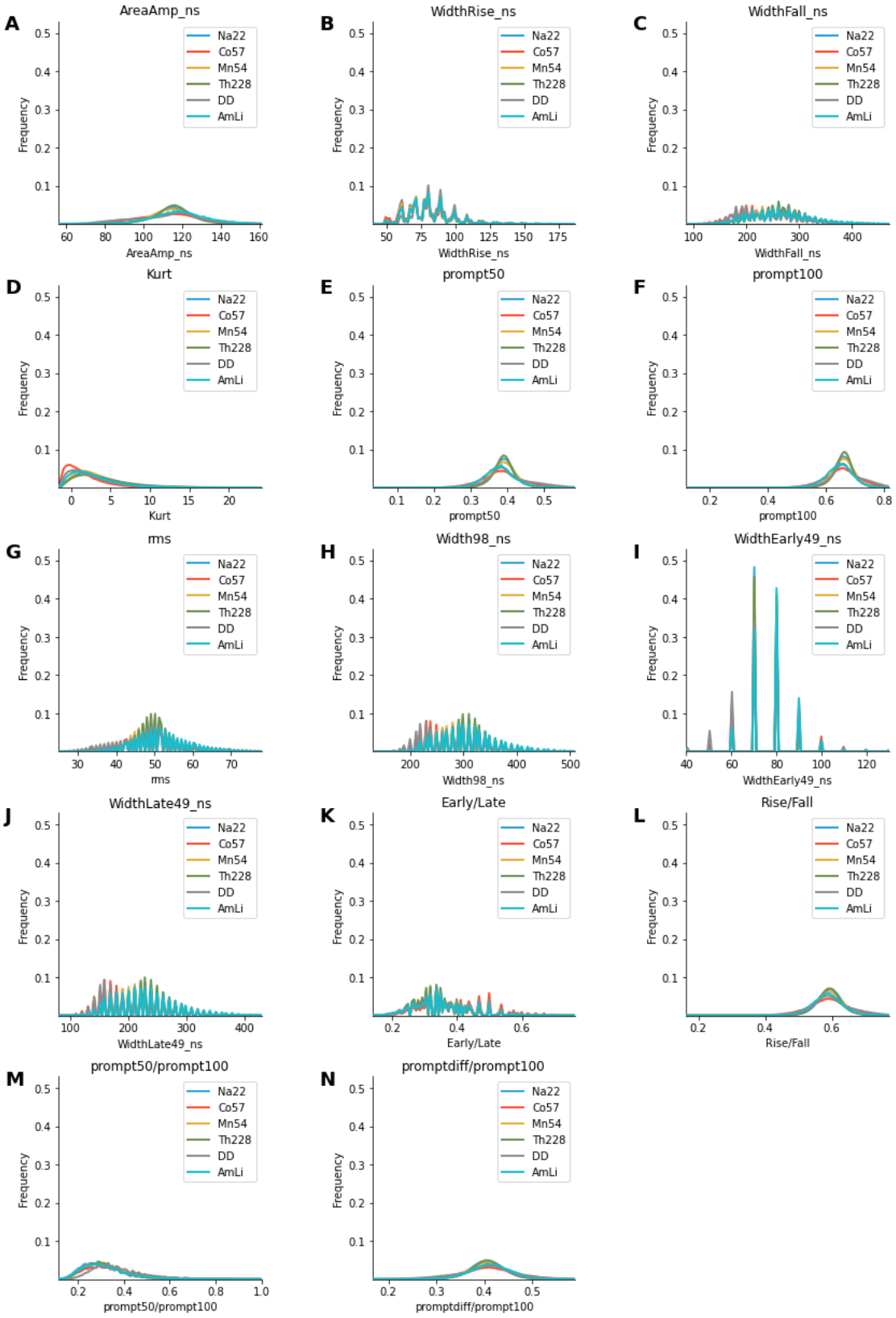

Figure 6.6: Overlay of RQ distributions for all sources individually.

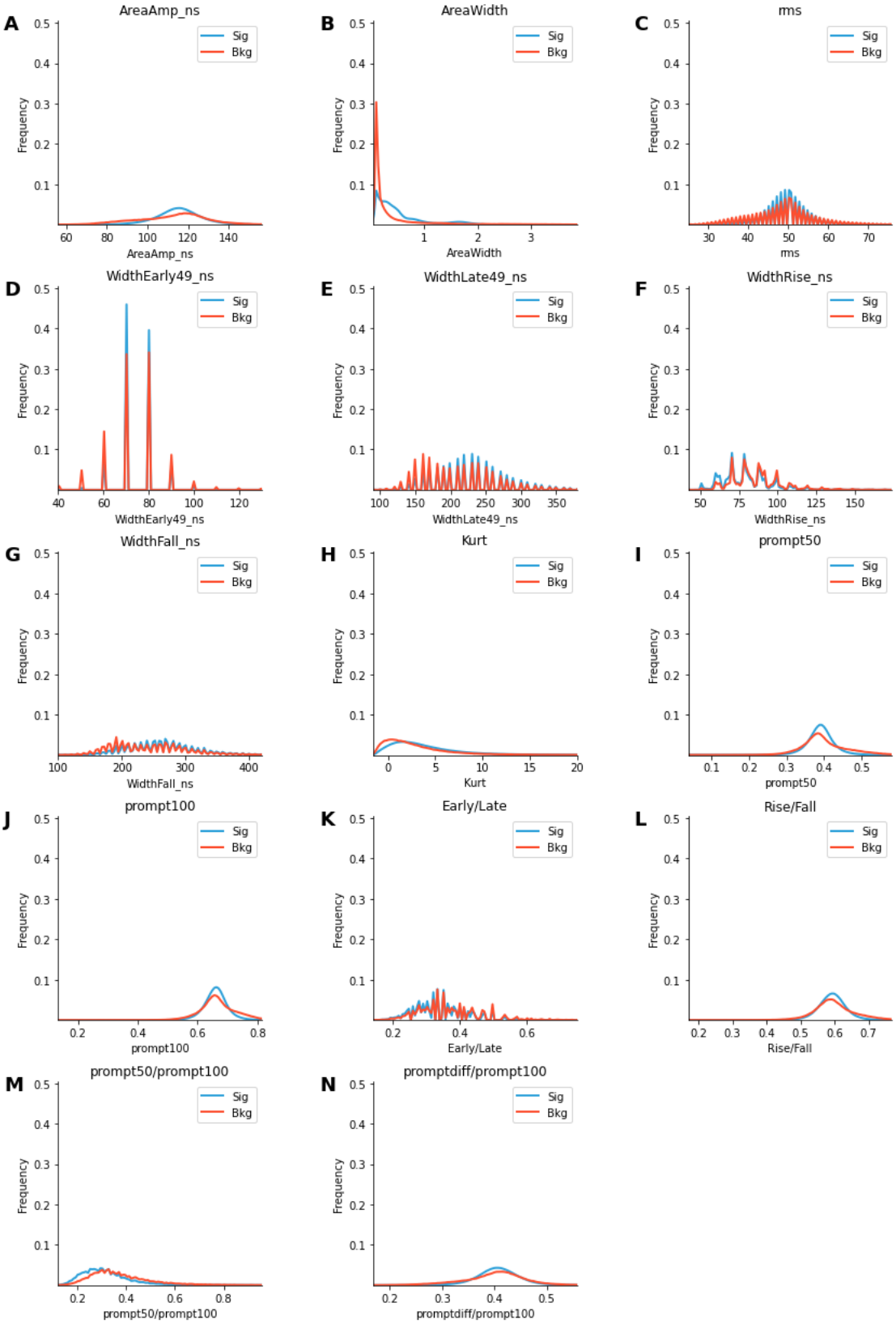

Figure 6.7: RQ distributions for merged signal and background source datasets.

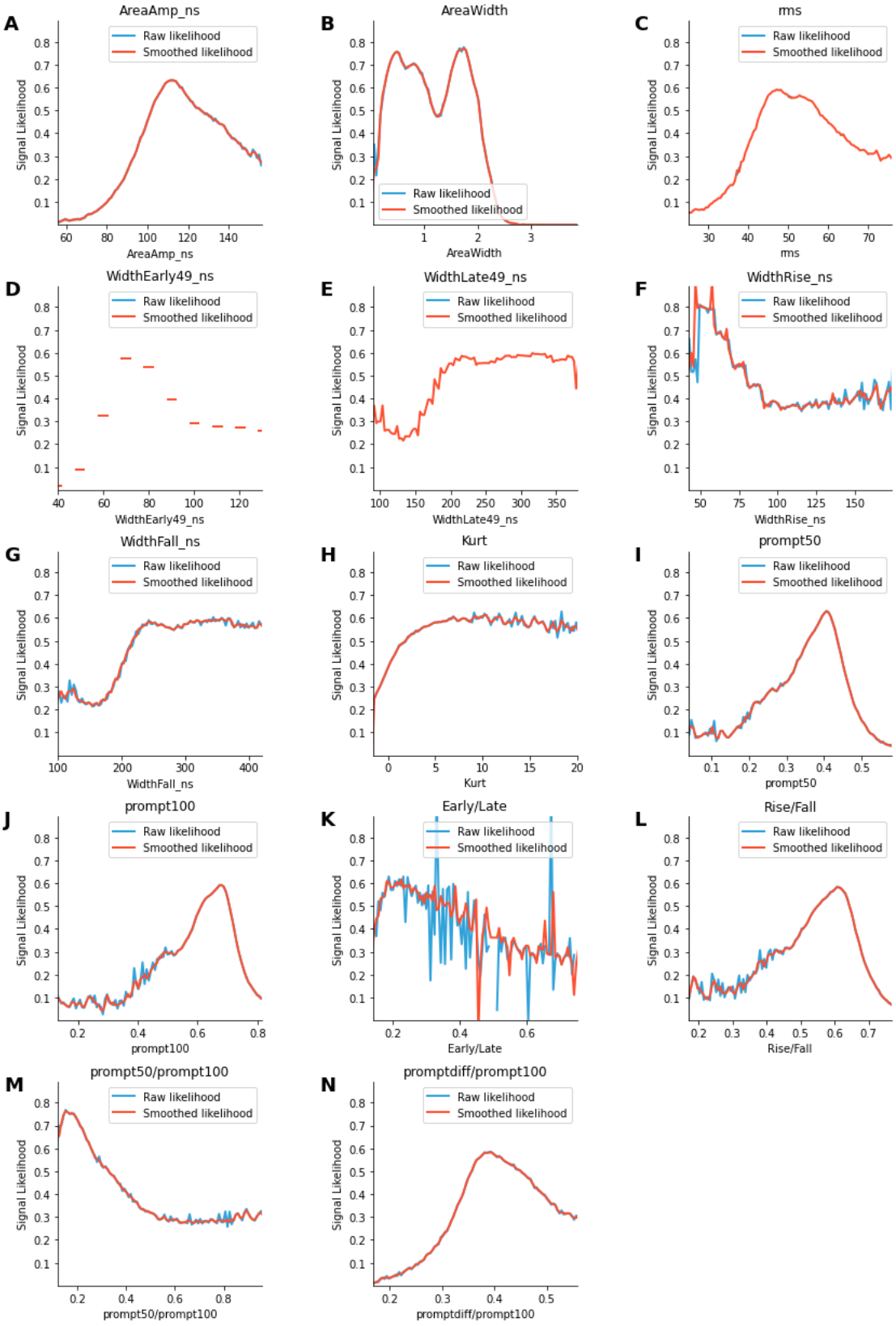

Figure 6.8: Likelihood distributions for parameters in Fig. 6.7

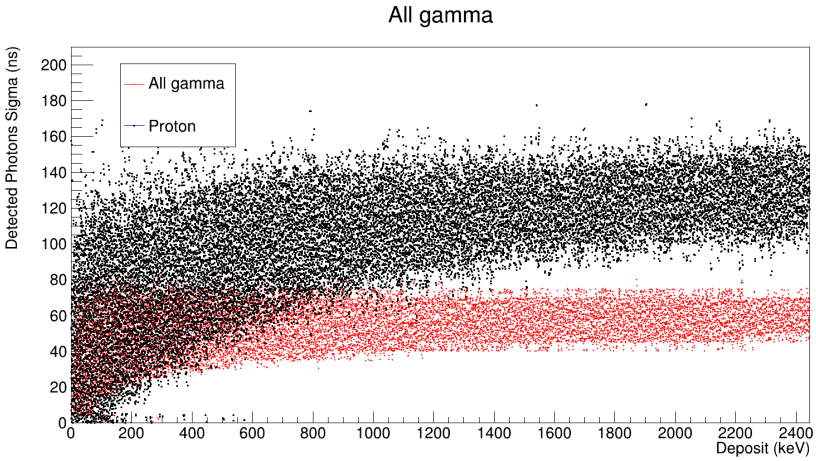

(a) Without reflection

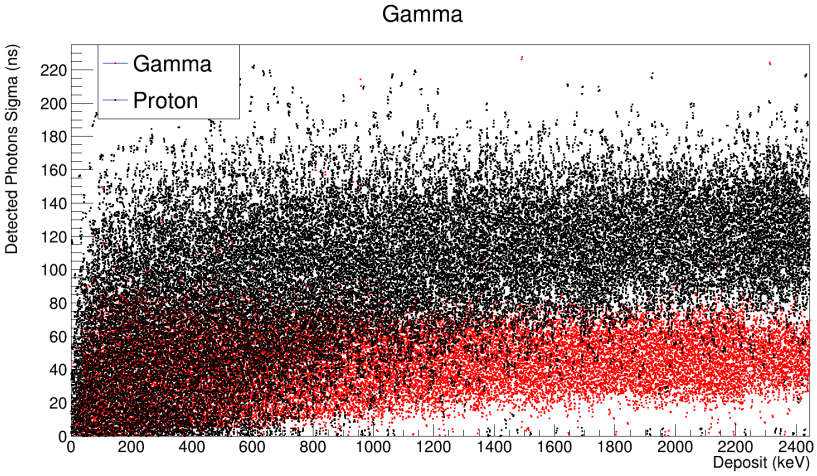

(b) With reflections

Figure 6.9: Comparing standard deviation of PMT hit times of photons from proton recoil and gamma energy deposits as a function of energy, with and without reflection.

CHAPTER VII

Results of the LZ First Science Run

In what follows the first science run (SR1) results of the LZ experiment are summarized. The SR1 results contain the highest sensitivity to spin-independent WIMP-nucleon scattering for masses above 9 GeV/c^2 to date [105].

This result is based on data collected from 23 December 2021 to 11 May 2022. Livetime for the WIMP search is defined as the time during which the DAQ is live and can record an event, and during which a WIMP interaction (if it were to occur) could be reconstructed. After removing periods for calibration, detector maintenance, 3% DAQ deadtime, and a 7% loss from periods of anomalous trigger rate, 89 days of search data. Due to elevated rates of activity experienced in dual-phase xenon TPCs after large S2 pulses [106, 107, 108, 109] and muons, a hold-off is implemented to remove these effects. These additional exclusions leave a final WIMP search livetime of 60 $\pm$ 1 days.

During this period, the liquid xenon maintained a stable (within 0.2%) temperature of 174.1 K and pressure of 1.791 bar(a). A drift field of 193 V/cm, and a gas extraction field of 7.3 kV/cm was established and maintained. The electron lifetime was observed at 5000 - 8000 μs throughout the run, far exceeding the maximum dift time in the TPC of 951 μs. The entire xenon quantity of 10 tonnes was continuously purified at a rate of 3.3 tonnes/day through a hot getter system [110].

The DAQ system, described briefly in section 3.5, records events for the WIMP search using the S2 filter trigger architecture. This trigger reaches and maintains, maximum efficiency for S2 pulses with 6 or more extracted electrons and had a typical rate of 5 Hz. The event window recorded when a trigger occurs is defined by a pre-trigger window of 2 ms and a post-trigger window of 2.5 ms.

7.1 Calibration

The calibration sources in Table 2.3 were used to determine the detector response model. ER calibrations using ^{131m}Xe, ^{83m}Kr, and tritiated methane (CH_3T) provide the energy calibration for the TPC. The resulting photon gain g_1 measured was 0.114±0.002 phd/photon. The resulting electron gain was 47.1±1.1 phd/electron [105]. These sources were also used to correct for the position dependent variation of S1 and S2 signals. The variation of the S1 signal is primarily due to geometric dependence of the S1 light collection efficiency and variation of PMT quantum efficiency. Variation in the S2 signal has the same origins as the S1 variation in addition to; electrostatic deflections of the gate and anode electrodes (radial variation), and electron absorption by trace impurities (vertical variation). The S1 correction normalizes the observed signal to the geometric center of the TPC, with the normalized value denoted $S1_c$. The S2 signal is normalized to a signal at the top of the detector (shortest drift time) in the radial centre, with the corrected value denoted $S2_c$. The AmLi source, and 2.45 MeV neutrons produced by the DD generator, are used to calibrate the NR response of the detector. From these ER and NR calibrations the corresponding bands ER and NR bands shown in Fig. 7.1 were produced.

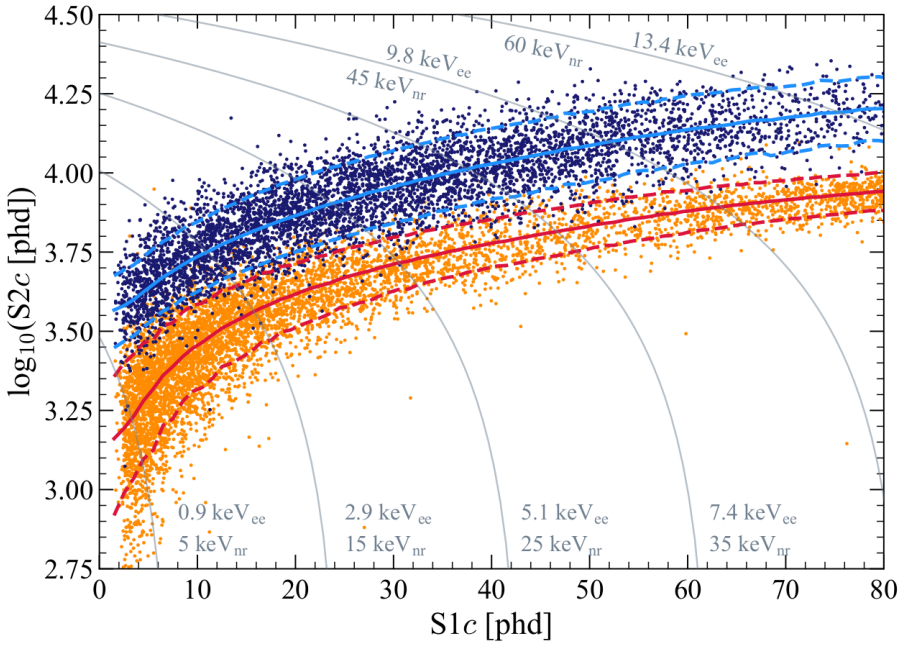

Figure 7.1: Calibration events in log 10 S2c-S1c for the tritium source (dark blue points, 5343 events) and the DD neutron source (orange points, 6324 events). Solid blue (red) lines indicate the median of the ER (NR) simulated distributions, and the dotted lines indicate the 10 % and 90 % quantiles. Thin grey lines show contours of constant electron-equivalent energy (keV$_{ee}$) and nuclear recoil energy (keV$_{nr}$). Figure from [105]

7.2 Event Selection

A variety of signal selection cuts were applied to the WIMP search data. The first and foremost of these is a selection for single scatter events only, since the low expected cross-section of WIMPs precludes multiple scatters in the detector. Secondly, a cut on pulse area was applied to restrict the analysis to regions of the parameter space for which signal and background are well modelled. For this reason, corrected S1 pulses were required to have areas larger than 3 phd and less than 80 phd. Corrected S2 pulses were required to have areas in excess of 600 phd and less than 100,000 phd.

Trace radioactive contaminants in detector components introduce additional background. This additional background is concentrated in the outer edges of the TPC where there is a higher density of detector components. In addition, events near the

cathode and anomalous above anode events pose the issues of un-physical drift times and below NR band single scatters. Due to the self-shielding property of liquid xenon briefly discussed in Chapter II, these backgrounds have a limited impact on the centre of the TPC. As a result, a fiducial volume cut was implemented to focus further analysis on well reconstructed events towards the centre of the detector. Drift time cuts requiring an excess of 86 μs and drift times below 936.5 μs define the lower and upper bounds of the fiducial volume. The radial fiducial volume cut is defined as 4 cm from the TPC wall in reconstructed position, based on dispersed ^{83m}Kr calibration data. A more aggressive radial cut was applied at the top and bottom of of the detector (drift time $<$ 200 μs and drift time $>$ 800 μs). This was due to elevated background rates in these regions.

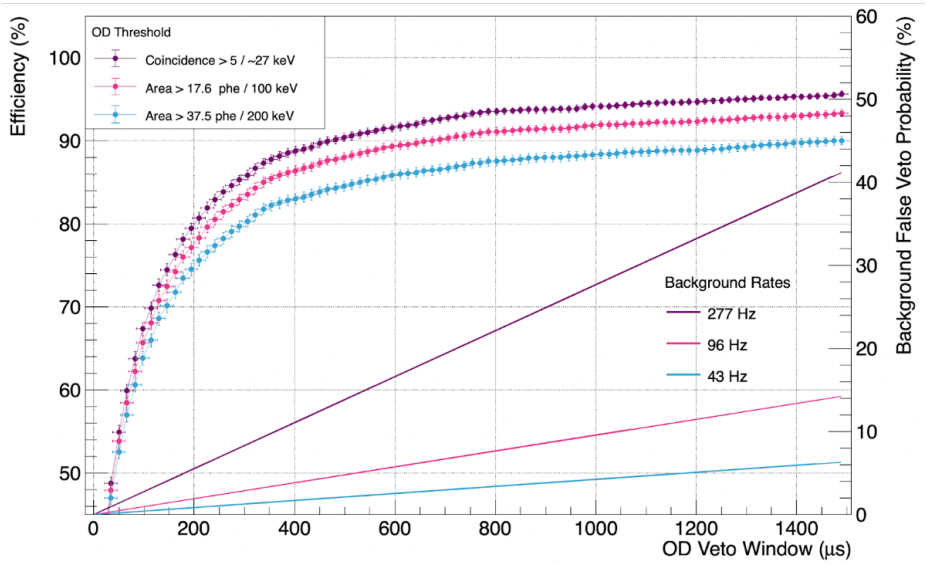

Figure 7.2: Neutron veto efficiency by the OD using data from the AmLi neutron calibration source. False veto probability defined using background rate in the OD which is dominated by the cavern γ-ray spectrum studied in Chapter V.

Finally, the skin and OD veto are applied. This veto represents the culmination of efforts by this author and their colleagues which have significant impact on the results of the first science run. A prompt and delayed veto are utilized, with the delayed veto having a larger pulse area requirement, to reduce the occurrence of

accidental veto. The prompt veto is defined by pulses of minimum area 17.6 phd (100 keV) within 0.3 μs of the TPC S1 pulse. The delayed veto is defined by pulses above 37.5 phd (200 keV) within 1200 μs after the TPC S1 signal. These settings were selected to maximize the neutron tagging efficiency shown in Fig. 7.2, whilst minimizing the false veto probability. This study was conducted using the AmLi neutron source data, and calculated the fraction of TPC single scatters in the NR band which also saw a coincident signal above the veto threshold in the OD. The selected veto window is longer than intended, reducing the the tagging efficiency. This is attributed to additional time spent by neutrons scattering in water saturated foam spacers between the OCV and acrylic tanks. This effect was not originally considered, but is discussed in detail in Ref. [69], with further studies to understand the effect ongoing. The resulting veto efficiency was 89 $\pm$ 3 %. The false veto probability was determined using background data to be 5 %. The impact of the

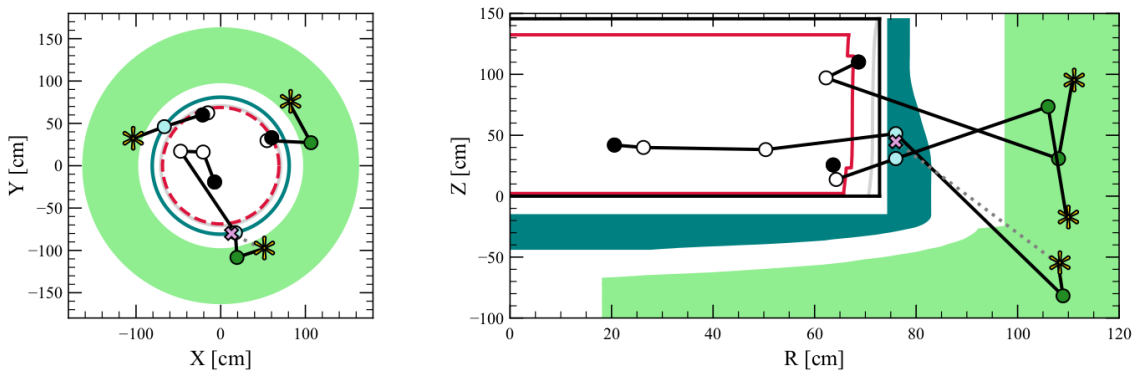

Figure 7.3: Locations of MS neutron events identified in the SR1 dataset, correlated across all three detectors. Chains of reconstructed scatters demonstrating inter-detector coincidences in tagging neutron events. Working outwards: the red outline indicates the SR1 FV; the gray curve highlights the TPC wall boundary in reconstructed space; the black box indicates the physical edges of the active xenon volume; the teal profile denotes the liquid xenon Skin; the outermost green region represents the OD acrylic tanks containing the GdLS. Black circles denote the locations of the scatters with shortest drift time in the given neutron MS chain, with empty circles showing the positions of other interactions in the TPC. Scatters in the Skin and OD are shaded in blue and green respectively. Neutron captures in the OD are marked as a $*$, and resulting gamma-ray splashes observed in the Skin are labelled with a pink cross. Figure from Ref. [111].

veto is displayed in Fig. 7.3, where the results of a side-band analysis of neutron events show a chain of neutron scatters in the TPC then the veto detectors. Here the neutron can be observed scattering in the TPC then capturing in the OD. This was generated for the LZ backgrounds paper by the author and their collaborators. The greatest benefit of the veto system to LZ is an increase in the fiducial volume of the TPC. With the ability to veto background events which produce coincident signals in the skin and OD, one can push the boundaries of the fiducial volume beyond the approximately 10 cm from the wall afforded by LXe self-shielding alone, without introducing an unreasonably large increase in background rates. This results in a much larger active target mass of 5.5 tonnes compared to the 3.2 tonnes without, corresponding to a 40% increase in exposure. The increase in exposure afforded by

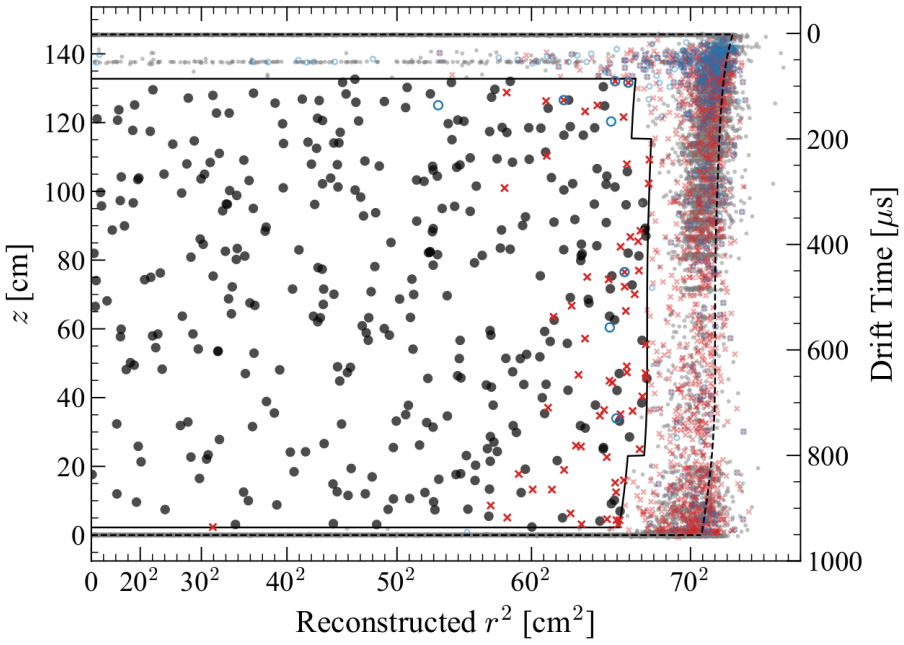

Figure 7.4: Data in reconstructed r^2 and z after all analysis cuts. Black (grey) points show the data inside (outside) the FV. Red crosses and blue circles show events vetoed by a prompt LXe skin or OD signal, respectively. The solid line shows the FV definition, and the dashed line shows the extent of the active TPC. Field non-uniformities cause the reconstructed r position of the active volume boundary to vary as a function of z. Events with drift time of approximately 50 µs are from recoils in the gas which produce S1 and S2 pulses with a fixed time separation. Figure from [105]

the use of an active veto constitutes the most crucial impact of this authors efforts (described in Chapters III, IV, and V) on the results of the first science run of LZ.

The distribution of events passing all selection criteria is shown in Fig. 7.4. Where the events removed by the veto near the walls are clearly visible. The high density of these vetoed events near the boundary of the fiducial region is the clearest indication of the increased exposure afforded to LZ, since the optimum way to mitigate these without the veto system would be to remove that portion of the target mass entirely.

7.3 Backgrounds

The overall TPC background model for the LZ WIMP search is shown in Fig. 7.5. There were 9 major components of which ^{214}Pb dominates. This component, along with ^{212}Pb are Rn daughters, specifically the ^{222}Rn and ^{220}Rn chains specifically, producing ERs. These are mitigated by the inline radon reduction system described in Ref. [110]. Additionally, the ^{85}Kr component is the next most significant, although it's contribution is regulated by mass spectrometer measurements of Xenon samples. These sources together form the full beta background, with contributions from detector components. ^{37}Ar and ^{127}Xe are a departure from the projected sensitivity and have been included to account for cosmogenic activation. These contributions are constrained using a side-band analysis and an accounting of the time spent above ground, during xenon transportation [111].

The total mass of Xenon constrains the contribution from the remaining Xenon isotopes. The final ER contribution comes from neutrinos which do not differ compared to the projected sensitivity analysis [112]. Detector components provided the largest contribution to NR events, which are constrained by the OD veto and assays of components. NR contribution from neutrinos is mitigated by the minimum S2 cut of 600 phd.

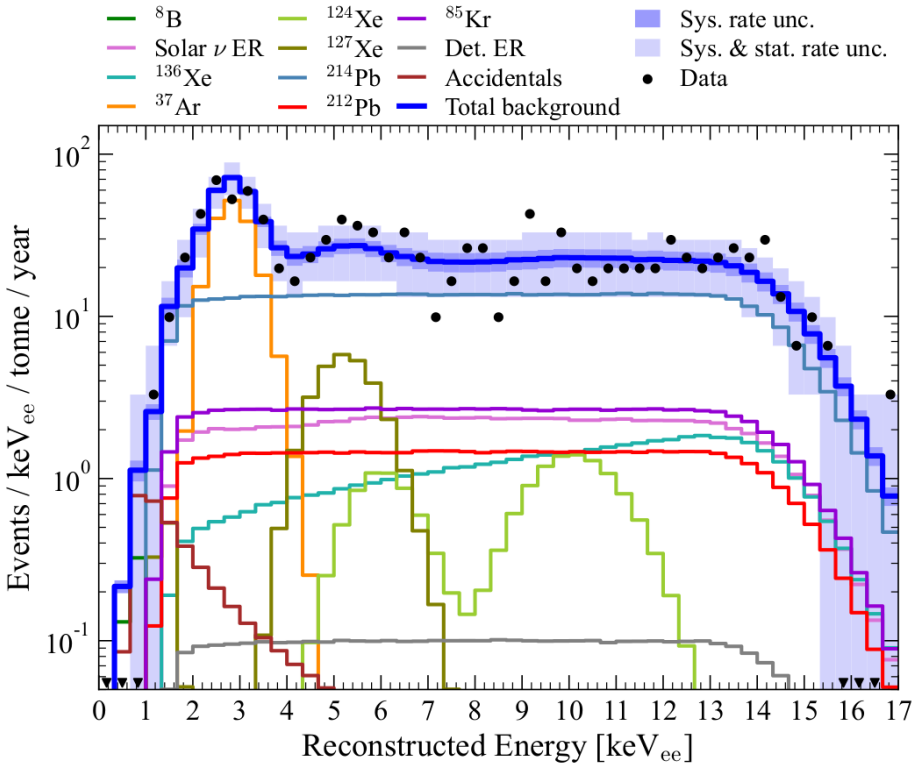

Figure 7.5: Background model before fitting to the SR1 data (except for the 37 Ar component, for which the post-fit normalization is used). The total model is shown in dark blue, and SR1 data after all WS cuts have been applied are denoted by the black points. This represents a background event rate of $(6.3 \pm 0.5) \times 10^{-5}$ events/keV$_{ee}$/kg/day. Figure from [111]

7.4 Results

A profile likelihood ratio (PLR) approach is used to determine the likelihood of a WIMP signal in data, given the background model shown in Fig. 7.5. This PLR analysis is performed in the $\log_{10}(\mathrm{S2}_c)$ vs $\mathrm{S1}_c$ 2D parameter space, in which a battery of frequentist tests provide limits on the WIMP-nucleon cross-section as a function of WIMP mass, by quantifying the level of discrepancy between data and the background-only model. A set of community recommended standards for statistical analysis of results are implemented in this approach [37]. This first science run did not include blinding, though it is planned for SR2. The placement of events passing cuts in $\mathrm{S1}_c$ vs log(S2) space is shown in Fig. 7.6. From this treatment, no WIMPs

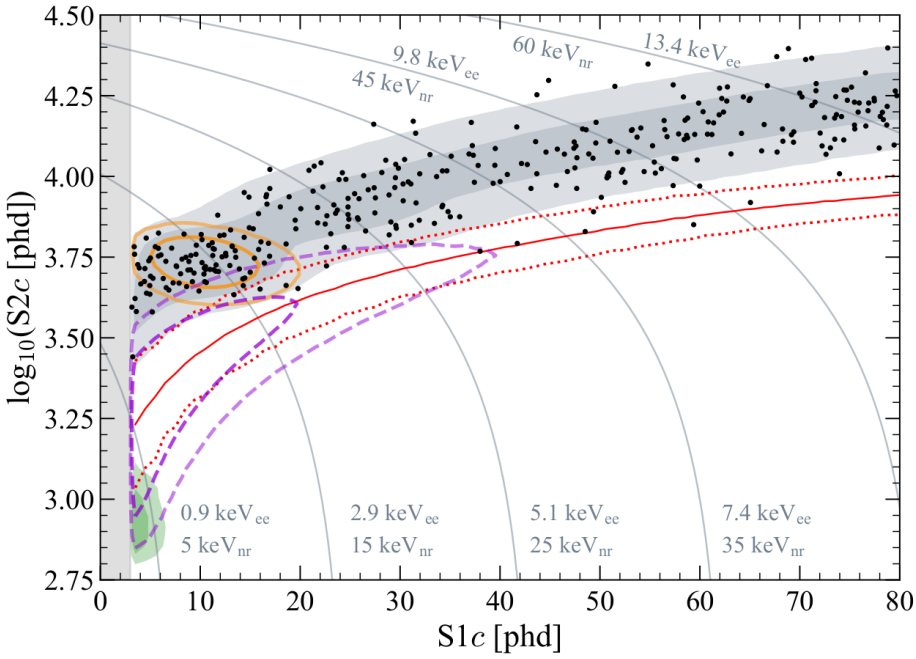

Figure 7.6: WIMP-search data (black points) after all cuts in log 10 S2c-S1c space. Contours enclose 1σ and 2σ of the following models: the best-fit background model (shaded grey regions), the 37 Ar component (orange ellipses), a 30 GeV/c 2 WIMP (purple dashed lines), and 8 B solar neutrinos (shaded green regions). The red solid line indicates the NR median, and the red dotted lines indicate the 10 % and 90 % quantiles. Thin grey lines indicate contours of constant energy. Figure from [105]

were identified, with the PLR yielding a best fit consistent with background only. Not having found WIMPs, the sensitivity reached is shown in Fig. 7.7. For WIMP masses from 9 GeV/c^2 to 10^4 GeV/c^2, this sensitivty outperforms all previous measurements. The downward fluctuation at 30 GeV is consistent with the background model which also shows a downward fluctuation at this energy. This energy corresponds to the best sensitivity in this study, and thus the most precise to date at 6.5×10^{-48}cm^2.

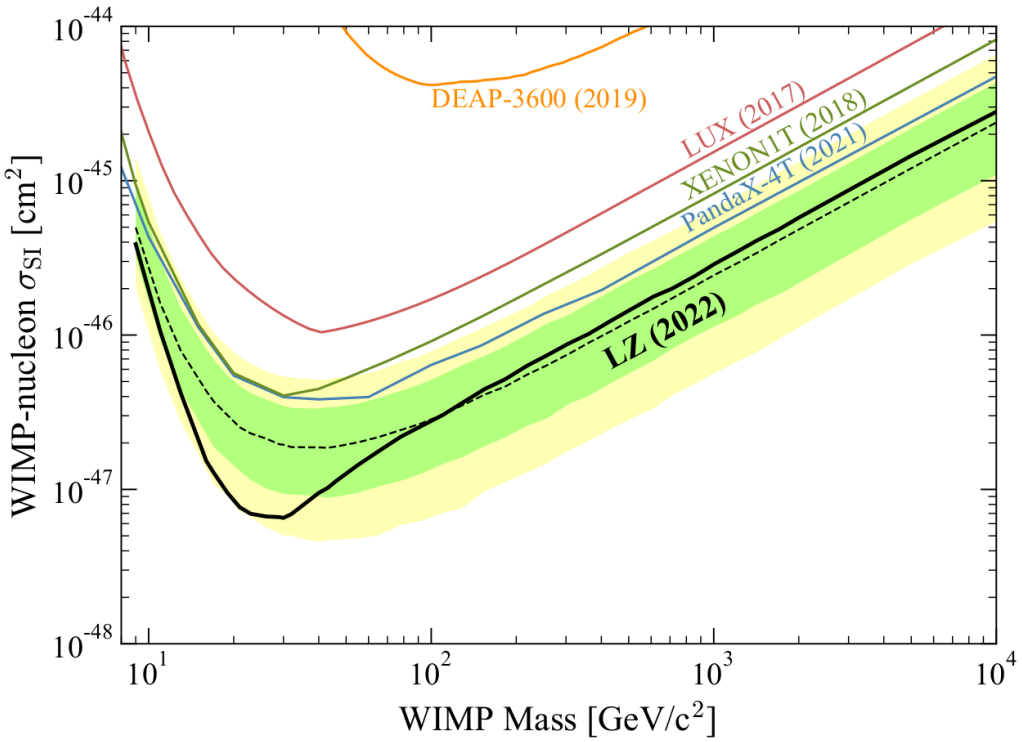

Figure 7.7: The 90 % confidence limit (black line) for the spin-independent WIMP cross section vs. WIMP mass. The green and yellow bands are the 1σ and 2σ sensitivity bands. The dotted line shows the median of the sensitivity projection. Also shown are the PandaX-4T [113], XENON1T [114], LUX [115], and DEAP-3600 [116] limits.[105]

CHAPTER VIII

Conclusion

Whilst the nature of dark matter remains veiled, LZ has constructed the most sensitive direct detection experiment to date producing world leading limits on spin-independent and spin-dependent WIMP-nucleon cross-sections. This was achieved using the world's largest (at the time of writing) dual-phase xenon time projection chamber containing 7 tonnes of active mass, two veto detectors, and the hard work of the entire LZ collaboration.

In Chapter III, the procedure for calibrating the OD PMTs was tested and successfully implemented in the commissioning of the outer detector. Allowing LZ to proceed with confidence in its veto capabilities. Additionally a series of tests were conducted to investigate the anomalous and excessive dark rate observed in PMTs deployed in water. Though no clear answer has been identified, it has been observed that this excessive rate is the result of external photons and is not related to any malfunction of the PMTs.

Having used the approaches defined in Chapter III, a recalibration of the installed and running OD PMTs in Chapter IV finds all parameters are within requirements. This sets an in-situ baseline are monitored throughout the operation of LZ, acting as a health check of the detector. An independent trigger of the OD was developed, with the aim of boosting statistics for higher energy processes such as the Gd capture

and H capture. This is useful for monitoring the ambient neutron environment, and studies involving muons which also produce large pulses but are rarer events. An assessment of the trigger efficiency using injected pulses from the OCS found a 100% trigger efficiency for pulses at or above the hydrogen capture peak.

The measurement of the gamma flux from the walls of the cavern housing LZ was detailed in Chapter V. The corresponding radioactive contamination levels were found to be 220±60 Bq/kg of ^{40}K, 29±15 Bq/kg of ^{238}U, and 13±3 Bq/kg of ^{232}Th; consistent with the shotcrete material used to coat the cavern walls. Radon in cavern air was found to produce a significant contribution to the measured rate, and there is no conclusive evidence for a significant flux from the high radioactivity rhyolite intrusion within the cavern nor asymmetric flux in the cavern. These results informed estimates of the background contribution from the Davis cavern for LZ, with a fit of the OD backgrounds showing the measured cavern spectra as the dominant source of background in the OD, contributing ∼50% of the total OD background rate above 500 keV.

A pulse shape discrimination was attempted in order to identify proton recoils such that one may veto neutrons which do not fully thermalise and the fast neutron spectrum may be probed. Using simulation output to inform selection criteria, a likelihood estimator using gamma calibration sources as background and DD neutron calibrations as the signal population was constructed for a variety of potential discriminator variables in Chapter VI. However, this study did not yield a suitably powerful discriminator due to the reflector system in the OD smearing the timing profile of scintillation light, a property which the discriminator sought after would be based. Despite this, the study did find that proton recoils from fast neutrons are within the observational reach of the OD, a prospect not expected in the initial design of the OD. In addition, due to the timing separation between recoils and captures, and the 1200 μs delayed veto window of LZ, it was found that though one is not

presently able to identify them as such, fast neutrons which do not fully thermalise and capture but cause recoils are also caught by the veto. Though a discriminator would still be beneficial as it would reduce the false veto rate due to gammas. Furthermore, even though no single one of the explored parameters proved a sufficiently powerful discriminator, the fact that the likelihood profiles generated were not flat indicates that a combination of these parameters may provide the desired discriminator. Determining how exactly to combine them is not trivial, and would be well served by a machine learning approach.

The first 60 live-day WIMP search which LZ used to report its world-leading result is merely a taste of what is to come. With a planned second science run of 1000 live-days due to begin imminently, LZ will improve its exposure by a factor of $\sim$17, pushing deeper into unexplored phase-space. The possibility of WIMP discovery with LZ remains.

BIBLIOGRAPHY

BIBLIOGRAPHY

[1] F. Zwicky. "Republication of: The redshift of extragalactic nebulae". In: *Gen. Relat. Gravit.* 41.1 (2009), pp. 207–224. ISSN: 0001-7701. DOI: 10.1007/s10714-008-0707-4.

[2] Ewa L Łokas and Gary A Mamon. "Dark matter distribution in the Coma cluster from galaxy kinematics: breaking the mass–anisotropy degeneracy". In: *Monthly Notices of the Royal Astronomical Society* 343.2 (2003), pp. 401–412.

[3] Vera C Rubin, W Kent Ford Jr, and Norbert Thonnard. "Rotational properties of 21 SC galaxies with a large range of luminosities and radii, from NGC 4605/R= 4kpc/to UGC 2885/R= 122 kpc". In: *The Astrophysical Journal* 238 (1980), pp. 471–487.

[4] KG Begeman, AH Broeils, and RH Sanders. "Extended rotation curves of spiral galaxies: Dark haloes and modified dynamics". In: *Monthly Notices of the Royal Astronomical Society* 249.3 (1991), pp. 523–537.

[5] WJG De Blok et al. "Mass density profiles of low surface brightness galaxies". In: *The Astrophysical Journal* 552.1 (2001), p. L23.

[6] Gianfranco Bertone, Dan Hooper, and Joseph Silk. "Particle dark matter: Evidence, candidates and constraints". In: *Physics reports* 405.5-6 (2005), pp. 279–390.

[7] R Kayser, S Refsdal, and R Stabell. "Astrophysical applications of gravitational micro-lensing". In: *Astronomy and Astrophysics* 166 (1986), pp. 36–52.

[8] LJ King et al. "A complete infrared Einstein ring in the gravitational lens system B1938+ 666". In: *Monthly Notices of the Royal Astronomical Society* 295.2 (1998), pp. L41–L44.

[9] Gianfranco Bertone and Dan Hooper. "History of dark matter". In: *Reviews of Modern Physics* 90.4 (2018), p. 045002.

[10] Douglas Clowe et al. "A direct empirical proof of the existence of dark matter". In: *The Astrophysical Journal* 648.2 (2006), p. L109.

[11] Arno A. Penzias and Robert G. Wilson. "A Measurement of excess antenna temperature at 4080-Mc/s". In: *The Astrophysical Journal* 142 (1965), pp. 419–421.

[12] R. A. Sunyaev. "The Thermal History of the Universe and the Spectrum of Relic Radiation". In: *Confrontation of Cosmological Theories with Observational Data*. Ed. by M. S. Longair. Dordrecht: Springer Netherlands, 1974, pp. 167–173. ISBN: 978-94-010-2220-0. DOI: 10.1007/978-94-010-2220-0_14. URL: https://doi.org/10.1007/978-94-010-2220-0_14.

[13] George F Smoot et al. "Structure in the COBE differential microwave radiometer first-year maps". In: *The Astrophysical Journal* 396 (1992), pp. L1–L5.

[14] Planck Collaboration. "Astronomy & Astrophysics (A&A)". In: *A&A* 594 (2016), A13.

[15] Nabila Aghanim et al. "Planck 2018 results-V. CMB power spectra and likelihoods". In: *Astronomy & Astrophysics* 641 (2020), A5.

[16] Planck Collaboration et al. "Planck 2018 results. VI. Cosmological parameters". In: (2020).

[17] Simon DM White, Carlos S Frenk, and Marc Davis. "Clustering in a neutrino-dominated universe". In: *The Astrophysical Journal* 274 (1983), pp. L1–L5.

[18] Scott Dodelson and Lawrence M Widrow. "Sterile neutrinos as dark matter". In: *Physical Review Letters* 72.1 (1994), p. 17.

[19] AA Aguilar-Arevalo et al. "MiniBooNE and MicroBooNE Joint Fit to a 3+ 1 Sterile Neutrino Scenario". In: *arXiv preprint arXiv:2201.01724* (2022).

[20] Alexey Boyarsky et al. "Sterile neutrino dark matter". In: *Progress in Particle and Nuclear Physics* 104 (2019), pp. 1–45.

[21] Igor Krasnov. "DUNE prospects in the search for sterile neutrinos". In: *Physical Review D* 100.7 (2019), p. 075023.

[22] Anson Hook. "TASI lectures on the strong CP problem and axions". In: *arXiv preprint arXiv:1812.02669* (2018).

[23] Roberto D Peccei and Helen R Quinn. "CP conservation in the presence of pseudoparticles". In: *Physical Review Letters* 38.25 (1977), p. 1440.

[24] Leanne D Duffy and Karl Van Bibber. "Axions as dark matter particles". In: *New Journal of Physics* 11.10 (2009), p. 105008.

[25] Nick Du et al. "Search for invisible axion dark matter with the axion dark matter experiment". In: *Physical review letters* 120.15 (2018), p. 151301.

[26] Derek F Jackson Kimball et al. "Overview of the cosmic axion spin precession experiment (CASPEr)". In: *Microwave Cavities and Detectors for Axion Research*. Springer, 2020, pp. 105–121.

[27] Stephen P Martin. "A supersymmetry primer". In: *Perspectives on supersymmetry II*. World Scientific, 2010, pp. 1–153.

[28] Martin Schmaltz and David Tucker-Smith. "Little higgs theories". In: *Annu. Rev. Nucl. Part. Sci.* 55 (2005), pp. 229–270.

[29] Dan Hooper and Stefano Profumo. "Dark matter and collider phenomenology of universal extra dimensions". In: *Physics Reports* 453.2-4 (2007), pp. 29–115.

[30] Gerard Jungman, Marc Kamionkowski, and Kim Griest. "Supersymmetric dark matter". In: *Physics Reports* 267.5-6 (1996), pp. 195–373.

[31] Robert J Scherrer and Michael S Turner. "On the relic, cosmic abundance of stable, weakly interacting massive particles". In: *Physical Review D* 33.6 (1986), p. 1585.

[32] Stefano Giagu. "WIMP dark matter searches with the ATLAS detector at the LHC". In: *Frontiers in Physics* 7 (2019), p. 75.

[33] David G Cerdeno and Anne M Green. "Direct detection of WIMPs". In: *arXiv preprint arXiv:1002.1912* (2010).

[34] Anne M Green. "Astrophysical uncertainties on the local dark matter distribution and direct detection experiments". In: *Journal of Physics G: Nuclear and Particle Physics* 44.8 (2017), p. 084001.

[35] N Wyn Evans, Ciaran AJ O'Hare, and Christopher McCabe. "Refinement of the standard halo model for dark matter searches in light of the Gaia Sausage". In: *Physical Review D* 99.2 (2019), p. 023012.

[36] Andrzej K Drukier, Katherine Freese, and David N Spergel. "Detecting cold dark-matter candidates". In: *Physical Review D* 33.12 (1986), p. 3495.

[37] D Baxter et al. "Recommended conventions for reporting results from direct dark matter searches". In: *The European Physical Journal C* 81.10 (2021), pp. 1–19.

[38] JD Lewin and PF Smith. "Review of mathematics, numerical factors, and corrections for dark matter experiments based on elastic nuclear recoil". In: *Astroparticle Physics* 6.1 (1996), pp. 87–112.

[39] Martin C Smith et al. "The RAVE survey: constraining the local galactic escape speed". In: *Monthly Notices of the Royal Astronomical Society* 379.2 (2007), pp. 755–772.

[40] Christopher McCabe. "The Earth's velocity for direct detection experiments". In: *Journal of Cosmology and Astroparticle Physics* 2014.02 (2014), p. 027.

[41] Ralph Schönrich, James Binney, and Walter Dehnen. "Local kinematics and the local standard of rest". In: *Monthly Notices of the Royal Astronomical Society* 403.4 (2010), pp. 1829–1833.

[42] R Abuter et al. "Improved GRAVITY astrometric accuracy from modeling optical aberrations". In: *Astronomy & Astrophysics* 647 (2021), A59.

[43] Mark W Goodman and Edward Witten. "Detectability of certain dark-matter candidates". In: *Physical Review D* 31.12 (1985), p. 3059.

[44] Vernon Barger, Wai-Yee Keung, and Gabe Shaughnessy. "Spin dependence of dark matter scattering". In: *Physical Review D* 78.5 (2008), p. 056007.

[45] P Klos et al. “Large-scale nuclear structure calculations for spin-dependent WIMP scattering with chiral effective field theory currents”. In: *Physical Review D* 88.8 (2013), p. 083516.

[46] J Engel. “Nuclear form factors for the scattering of weakly interacting massive particles”. In: *Physics Letters B* 264.1-2 (1991), pp. 114–119.

[47] B. J. Mount et al. “LUX-ZEPLIN (LZ) Technical Design Report”. In: (Mar. 2017). arXiv: `1703.09144 [physics.ins-det]`.

[48] DS Akerib et al. “The lux-zeplin (lz) experiment”. In: *Nuclear Instruments and Methods in Physics Research Section A: Accelerators, Spectrometers, Detectors and Associated Equipment* 953 (2020), p. 163047.

[49] D.S Akerib et al. “Identification of Radiopure Titanium for the LZ Dark Matter Experiment and Future Rare Event Searches”. In: *Astropart. Phys.* 96 (2016), pp. 1–10.

[50] AC Kahler et al. “ENDF/B-VII. 1 neutron cross section data testing with critical assembly benchmarks and reactor experiments”. In: *Nuclear Data Sheets* 112.12 (2011), pp. 2997–3036.

[51] Carl Eric Dahl. “The physics of background discrimination in liquid xenon, and first results from Xenon10 in the hunt for WIMP dark matter”. PhD thesis. Princeton University, 2009.

[52] LW Goetzke et al. “Measurement of light and charge yield of low-energy electronic recoils in liquid xenon”. In: *Physical Review D* 96.10 (2017), p. 103007.

[53] Jens Lindhard et al. “Integral equations governing radiation effects”. In: *Mat. Fys. Medd. Dan. Vid. Selsk* 33.10 (1963), pp. 1–42.

[54] Gregory Rischbieter. “Signal Yields and Detector Modeling in Xenon Time Projection Chambers, and Results of an Effective Field Theory Dark Matter Search Using LUX Data”. PhD thesis. University at Albany, State University of New York, 2022.

[55] Belina Von Krosigk. “Measurement of proton and alpha-particle quenching in LAB based scintillators and determination of spectral sensitivities to supernova neutrinos in the SNO+ detector”. PhD thesis. Technische Universitat Dresden, 2015.

[56] Wei-Li Zhong et al. “Measurement of decay time of liquid scintillator”. In: *Nuclear Instruments and Methods in Physics Research Section A: Accelerators, Spectrometers, Detectors and Associated Equipment* 587.2-3 (2008), pp. 300–303.

[57] Qiang Du et al. “Response of gadolinium doped liquid scintillator to charged particles: measurement based on intrinsic U/Th contamination”. In: *Journal of Instrumentation* 13.04 (2018), P04001.

[58] "1.A - The Interactions of Charged Particles with Matter". In: *Nuclear Spectroscopy*. Ed. by FAY AJZENBERG-SELOVE. Vol. 9. Pure and Applied Physics. Elsevier, 1960, pp. 3–30. DOI: https://doi.org/10.1016/B978-1-4832-3063-4.50009-6. URL: https://www.sciencedirect.com/science/article/pii/B9781483230634500096.

[59] Hans Bethe. "Bremsformel für elektronen relativistischer geschwindigkeit". In: *Zeitschrift für Physik* 76.5 (1932), pp. 293–299.

[60] John Betteley Birks. "Scintillations from organic crystals: specific fluorescence and relative response to different radiations". In: *Proceedings of the Physical Society. Section A* 64.10 (1951), p. 874.

[61] CN Chou. "The nature of the saturation effect of fluorescent scintillators". In: *Physical Review* 87.5 (1952), p. 904.

[62] B. von Krosigk et al. "Measurement of the proton light response of various LAB based scintillators and its implication for supernova neutrino detection via neutrino–proton scattering". In: *The European Physical Journal C* 73.4 (Apr. 2013). DOI: 10.1140/epjc/s10052-013-2390-1. URL: https://doi.org/10.1140.

[63] Kaito Hagiwara et al. *Gamma Ray Spectrum from Thermal Neutron Capture on Gadolinium-157*. 2018. DOI: 10.48550/ARXIV.1809.02664. URL: https://arxiv.org/abs/1809.02664.

[64] S F Mughabghab. *Thermal neutron capture cross sections resonance integrals and g-factors*. Tech. rep. Wien: Int. Nucl. Data Comm., 2003. URL: https://cds.cern.ch/record/747981.

[65] RC Greenwood and WW Black. "The binding energy of the deuteron determined from measurement of the hydrogen neutron capture gamma-ray energy". In: *Physics Letters* 21.6 (1966), pp. 702–704.

[66] S.J. Haselschwardt et al. "A liquid scintillation detector for radioassay of gadolinium-loaded liquid scintillator for the LZ Outer Detector". In: *Nuclear Instruments and Methods in Physics Research Section A: Accelerators, Spectrometers, Detectors and Associated Equipment* 937 (Sept. 2019), pp. 148–163. DOI: 10.1016/j.nima.2019.05.055. URL: https://doi.org/10.1016/j.nima.2019.05.055.

[67] Hamamatsu. *LARGE PHOTOCATHODE AREA PHOTOMULTIPLIER TUBES*. URL: https://www.hamamatsu.com/content/dam/hamamatsu-photonics/sites/documents/99_SALES_LIBRARY/etd/LARGE_AREA_PMT_TPMH1376E.pdf.

[68] W. Turner et al. "Optical calibration system for the LUX-ZEPLIN (LZ) outer detector". In: *Nuclear Instruments and Methods in Physics Research Section A: Accelerators, Spectrometers, Detectors and Associated Equipment* 1010 (Sept. 2021), p. 165551. ISSN: 0168-9002. DOI: 10.1016/j.nima.2021.165551. URL: http://dx.doi.org/10.1016/j.nima.2021.165551.

[69] Sam Eriksen. "Commissioning of the Outer Detector of the LUX-ZEPLIN experiment and a study of the experiment's sensitivity to signatures arising from effective field theory operators". PhD thesis. University of Bristol, 2022.

[70] Alvaro Chavarria. "A study on the reflectivity of Tyvek". In: *APS Southeastern Section Meeting Abstracts*. Vol. 73. 2006, GC–007.

[71] William Taylor. "Neutron Calibrations and Activation Signals in Low-Background Liquid Xenon Dark Matter Detectors". PhD thesis. Brown University, 2022.

[72] Eryk Druszkiewicz. *The Data Acquisition System for LZ*. 2015. DOI: 10.48550/ARXIV.1511.08385. URL: https://arxiv.org/abs/1511.08385.

[73] D.S Akerib et al. "Simulations of events for the LUX-ZEPLIN (LZ) dark matter experiment". In: *Astroparticle Physics* 125 (Feb. 2021), p. 102480. DOI: 10.1016/j.astropartphys.2020.102480. URL: https://doi.org/10.1016/j.astropartphys.2020.102480.

[74] S. et al Agostinelli. "GEANT4—a simulation toolkit". In: *Nuclear instruments and methods in physics research section A: Accelerators, Spectrometers, Detectors and Associated Equipment* 506.3 (2003), pp. 250–303.

[75] M Szydagis et al. "NEST: Noble Element Simulation Technique". In: *Astrophysics Source Code Library* (2013).

[76] Melih Solmaz. "Search for annual and diurnal modulations in the LUX experiment and assembling a tagged neutron source for the LZ Outer Detector". PhD thesis. UC, Santa Barbara (main), 2020.

[77] F Bečvář. "Simulation of γ cascades in complex nuclei with emphasis on assessment of uncertainties of cascade-related quantities". In: *Nuclear Instruments and Methods in Physics Research Section A: Accelerators, Spectrometers, Detectors and Associated Equipment* 417.2-3 (1998), pp. 434–449.

[78] G. Barrand et al. "GAUDI - A software architecture and framework for building HEP data processing applications". In: *Comput. Phys. Commun.* 140 (2001), pp. 45–55. DOI: 10.1016/S0010-4655(01)00254-5.

[79] KK Hamamatsu Photonics. *PHOTOMULTIPLIER TUBES Basics and Applications, 4-th edition*. 2017.

[80] FP An et al. "The muon system of the Daya Bay Reactor antineutrino experiment". In: *Nuclear Instruments and Methods in Physics Research Section A: Accelerators, Spectrometers, Detectors and Associated Equipment* 773 (2015), pp. 8–20.

[81] Raymond C Smith and Karen S Baker. "Optical properties of the clearest natural waters (200–800 nm)". In: *Applied optics* 20.2 (1981), pp. 177–184.

[82] Ewan Fraser. "Calibration of the Outer Detector, Offline Data Quality Monitoring and Study of Laboratory and Neutron Backgrounds for Dark Matter searches in LZ". PhD thesis. University of Liverpool, 2022.

[83] S. Shaw et al. “Measurement of the gamma ray background in the Davis cavern at the Sanford Underground Research Facility”. In: *Astroparticle Physics* 116 (Mar. 2020), p. 102391. DOI: 10.1016/j.astropartphys.2019.102391. URL: https://doi.org/10.1016/j.astropartphys.2019.102391.

[84] J Heise. “The Sanford Underground Research Facility at Homestake”. In: *Journal of Physics: Conference Series* 606 (May 2015), p. 012015. DOI: 10.1088/1742-6596/606/1/012015. URL: https://doi.org/10.1088/1742-6596/606/1/012015.

[85] MC Perillo et al Isaac. *High Energy Gamma-Rays Measurements in the SNO Cavity*. Tech. rep. SNO-STR-97.

[86] D.-M. Mei and A. Hime. “Muon-induced background study for underground laboratories”. In: *Phys. Rev.* D73 (2006), p. 053004. DOI: 10.1103/PhysRevD.73.053004. arXiv: astro-ph/0512125 [astro-ph].

[87] ORTEC. *MAESTRO Multichannel Analyzer Emulation*. https://www.ortec-online.com/products/application-software/maestro-mca. URL: https://www.ortec-online.com/products/application-software/maestro-mca.

[88] M. Moszyński. “Inorganic scintillation detectors in γ-ray spectrometry”. In: *Nuclear Instruments and Methods in Physics Research Section A: Accelerators, Spectrometers, Detectors and Associated Equipment* 505.1 (2003). Proceedings of the tenth Symposium on Radiation Measurements and Applications, pp. 101–110. ISSN: 0168-9002. DOI: https://doi.org/10.1016/S0168-9002(03)01030-1. URL: http://www.sciencedirect.com/science/article/pii/S0168900203010301.

[89] Adhikari et al. “Understanding internal backgrounds in NaI(Tl) crystals toward a 200 kg array for the KIMS-NaI experiment”. In: *Eur. Phys. J.* C76.4 (2016), p. 185.

[90] V. Tomasello, M. Robinson, and V. A. Kudryavtsev. “Radioactive background in a cryogenic dark matter experiment”. In: *Astropart. Phys.* 34 (2010), pp. 70–79. DOI: 10.1016/j.astropartphys.2010.05.005.

[91] D-M. Mei et al. “Early Results on Radioactive Background Characterization for Sanford Laboratory and DUSEL Experiments”. In: *Astropart. Phys.* 34 (2010), pp. 33–39. DOI: 10.1016/j.astropartphys.2010.04.003. arXiv: 0912.0211 [nucl-ex].

[92] Ilka Antcheva et al. “ROOT—A C++ framework for petabyte data storage, statistical analysis and visualization”. In: *Computer Physics Communications* 182.6 (2011), pp. 1384–1385.

[93] Wouter Verkerke and David Kirkby. “The RooFit toolkit for data modeling”. In: *Statistical Problems in Particle Physics, Astrophysics and Cosmology*. World Scientific, 2006, pp. 186–189.

[94] K. J. Thomas. *An Estimate of the Gamma Flux in the East Counting Room of the Davis Cavern*. Tech. rep. Lawrence Berkeley National Laboratory (LBNL), 1 Cyclotron Road, Berkeley, CA 94720-8099, USA, 2014.

[95] Andreas Best et al. "Low energy neutron background in deep underground laboratories". In: *Nuclear Instruments and Methods in Physics Research Section A: Accelerators, Spectrometers, Detectors and Associated Equipment* 812 (2016), pp. 1–6.

[96] N. P. Heydenburg and G. M. Temmer. "Gamma Rays from Li^7, F^{19}, Ne^{22}, and Na^{22} Produced by Alpha-Particle Bombardment of Lithium and Fluorine". In: *Phys. Rev.* 94 (5 June 1954), pp. 1252–1257. DOI: 10.1103/PhysRev.94.1252. URL: https://link.aps.org/doi/10.1103/PhysRev.94.1252.

[97] VA Kudryavtsev, P Zakhary, and B Easeman. "Neutron production in (α, n) reactions". In: *Nuclear Instruments and Methods in Physics Research Section A: Accelerators, Spectrometers, Detectors and Associated Equipment* 972 (2020), p. 164095.

[98] N Nica. "Nuclear data sheets for A= 155". In: *Nuclear Data Sheets* 160 (2019), pp. 1–404.

[99] RG Helmer. "Nuclear data sheets for A= 157". In: *Nuclear Data Sheets* 78.2 (1996), pp. 219–394.

[100] CW Reich. "Nuclear data sheets for A= 154". In: *Nuclear Data Sheets* 110.10 (2009), pp. 2257–2532.

[101] CW Reich. "Nuclear data sheets for A= 156". In: *Nuclear Data Sheets* 113.11 (2012), pp. 2537–2840.

[102] Kevin P Balanda and HL MacGillivray. "Kurtosis: a critical review". In: *The American Statistician* 42.2 (1988), pp. 111–119.

[103] Y Jeong et al. "Pulse-shape Discrimination of Fast Neutron Background using Convolutional Neural Network for NEOS II". In: *Journal of the Korean Physical Society* 77.12 (2020), pp. 1118–1124.

[104] Cristiano Galbiati and John F. Beacom. "Measuring the cosmic ray muon-induced fast neutron spectrum by (n, p) isotope production reactions in underground detectors". In: *Phys. Rev. C* 72 (2 Aug. 2005), p. 025807. DOI: 10.1103/PhysRevC.72.025807. URL: https://link.aps.org/doi/10.1103/PhysRevC.72.025807.

[105] J Aalbers et al. "First dark matter search results from the LUX-ZEPLIN (LZ) experiment". In: *arXiv preprint arXiv:2207.03764* (2022).

[106] XENON Collaboration et al. "Dark matter search results from a one ton-year exposure of xenon1t". In: *Physical review letters* 121.11 (2018), p. 111302.

[107] DS Akerib et al. "Results from a search for dark matter in the complete LUX exposure". In: *Physical review letters* 118.2 (2017), p. 021303.

[108] Peter Sorensen. "Electron train backgrounds in liquid xenon dark matter search detectors are indeed due to thermalization and trapping". In: *arXiv preprint arXiv:1702.04805* (2017).

[109] DS Akerib et al. "Investigation of background electron emission in the LUX detector". In: *Physical Review D* 102.9 (2020), p. 092004.

[110] Maris Arthurs. "Radon Reduction and the First Science Results of the LZ Experiment". PhD thesis. University of Michigan, 2022.

[111] J Aalbers et al. "Background Determination for the LUX-ZEPLIN (LZ) Dark Matter Experiment". In: *arXiv preprint arXiv:2211.17120* (2022).

[112] DS Akerib et al. "Projected WIMP Sensitivity of the LUX-ZEPLIN (LZ) Dark Matter Experiment. arXiv 2018". In: *arXiv preprint arXiv:1802.06039* ().

[113] Yue Meng et al. "Dark matter search results from the PandaX-4T commissioning run". In: *Physical Review Letters* 127.26 (2021), p. 261802.

[114] XENON Collaboration et al. "Dark matter search results from a one ton-year exposure of xenon1t". In: *Physical review letters* 121.11 (2018), p. 111302.

[115] DS Akerib et al. "Results from a search for dark matter in the complete LUX exposure". In: *Physical review letters* 118.2 (2017), p. 021303.

[116] P-A Amaudruz et al. "First results from the DEAP-3600 dark matter search with argon at SNOLAB". In: *Physical review letters* 121.7 (2018), p. 071801.